Investigation of Hypersonic Transitional Shock Wave Boundary-Layer Interactions

L.N. Lodder

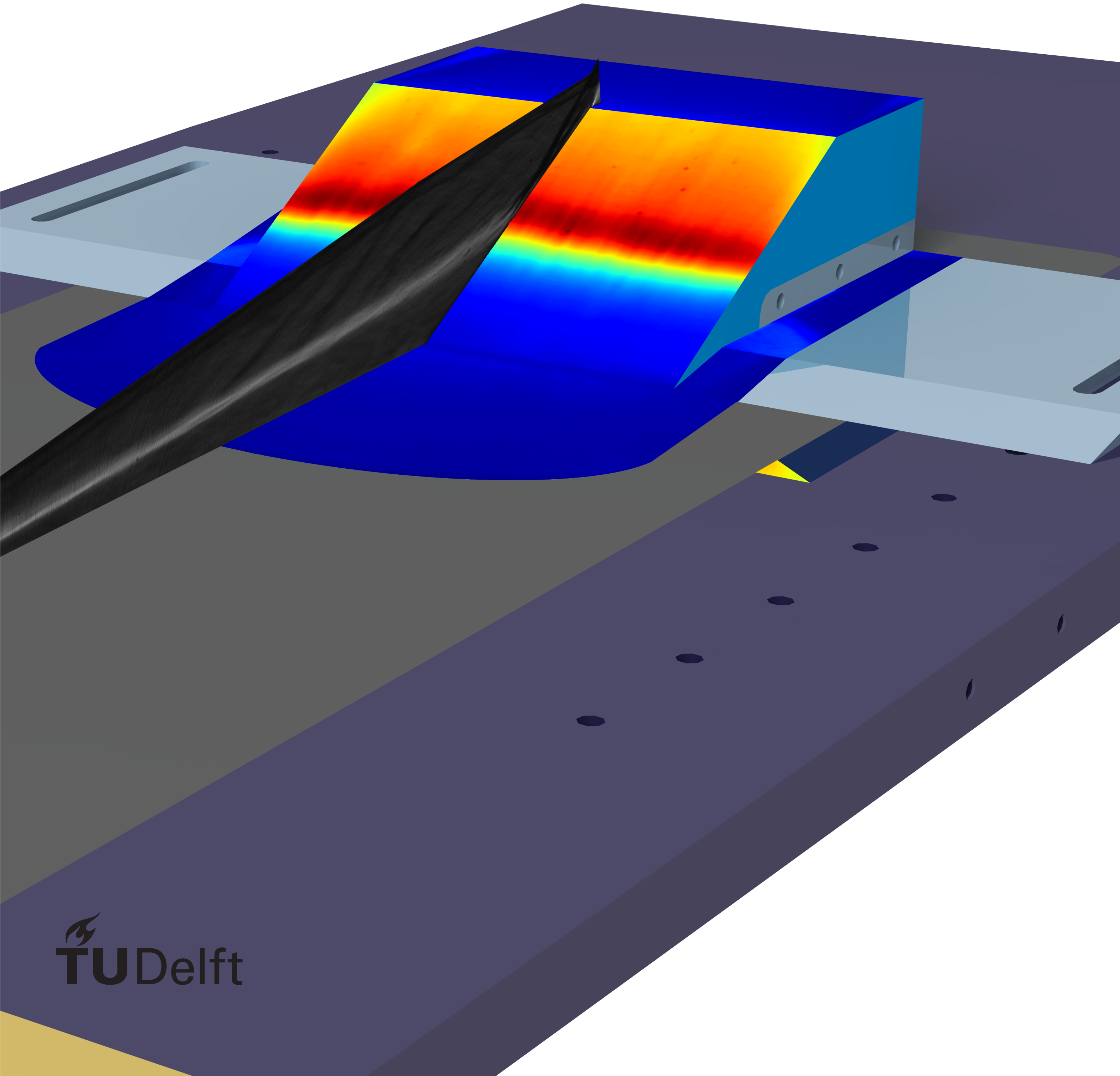

Investigation of Hypersonic Transitional Shock Wave Boundary-Layer Interactions

by

L.N. Lodder

to obtain the degree of Master of Science
at the Delft University of Technology,
to be defended publicly on Thursday July 16, 2020 at 09:30 AM.

Student number:	4296990
Supervisors:	Dr. ir. F.F.J. (Ferry) Schrijer,
	Dr. ir. B.W. (Bas) van Oudheusden

An electronic version of this thesis is available at `http://repository.tudelft.nl/`.

TU Delft

Preface

This document is the end result of my master thesis with the title: Investigation of Hypersonic Transitional Shock Wave Boundary-Layer Interactions. It also entails the end of my time as an Aerospace Engineering student at the Delft University of Technology.

First of all, I would like to thank Ferry Schrijer for his help in getting the HTFD up and running and for his supervision and advice during the master thesis. Also I want to thank Bas van Oudheusden for his additional insights. Furthermore, thank you Peter Duyndam for the support when I needed help with adapting the HTFD or other technical stuff and thank you Frits Donker Duyvis for helping me with the Schlieren set-up.

Above all, I would like to thank my parents and girlfriend for their love and support during my study. Finally, my friends, thank you for the highly valued coffee breaks, help and the memorable time you gave me during my study. You have made my master Aerodynamics a walk in the park.

Thank you,

L.N. Lodder
Delft, July 2020

Summary

Hypersonic flows over lifting vehicles are characterized by the high amount of thermal loading present on the structure. Especially around control surfaces, that guarantee maneuverability of the vehicle, very high thermal loads are found. Besides the thermal loads, hypersonic lifting vehicles encounter a large range of Reynolds numbers during the descending and ascending phase. The combination of the two effects creates a shock wave boundary-layer interaction that is very challenging to predict.

In the past, a lot of research is done on this in the form of flows over compression ramps. However, still not every aspect is clearly understood. In this report an investigation is performed on strong shock wave boundary-layer interactions in compression ramp flows. In front of the compression ramp a very long flat plate is placed which results in a thick boundary-layer at the interaction location. This will enlarge the effects present in the shock wave boundary-layer and aids the visualization of the interaction.

Measurements are performed using Schlieren, Quantative InfraRed Thermography (QIRT) and Background Orientated Schlieren (BOS) in the HTFD wind tunnel in Delft. The working principle of the HTFD is based on the Ludwig tube principle. The experiments are performed at a Mach number of 7 and at a range of ramp leading Reynolds numbers of $1.67 \cdot 10^6 - 5.30 \cdot 10^6$. The model consists of a flat plate on which five different compression ramps can be placed. The ramps have angles of 10°, 15°, 20°, 25° and 30° and are designed such that they do not block the wind tunnel too much.

The Schlieren measurements show clearly the typical flow topology found in compression ramp flows. A separation shock wave is present that closely resembles the theoretical inviscid shock wave angle. In front of the ramp, a separation bubble is present with on top a strong shear layer. At the reattachment location a strong reattachment shock wave is present. Furthermore, clear compression waves are found between the shear layer and the separation shock. The waves can be traced back to instability waves in the shear layer which points at a transitional shear layer.

From the Schlieren images, quantitative data is obtained in the form of the shear layer length, the shear layer angle and the fluctuations during the run. The shear layer length shows a clear dependency on both the ramp angle and the Reynolds number. Both variables cause an increase in the shear layer length when they are increased. The shear layer angle gets lower with an increasing Reynolds number and gets higher with an increasing ramp angle.

The fluctuations are based on the computation of a Standard Deviation (STD) field in time. This STD field gives additional information on instabilities waves in the shear layer. It is found that at high ramp angles and high Reynolds numbers the shear layer is getting turbulent near the ramp. Outside the turbulent part, the instability waves clearly grow inside the shear layer. Also, the shape of the waves change in the shear layer from asymmetrical to a more symmetrical profile.

To get QIRT data, first a successful calibration of the camera was performed using a black body. Besides that, calibration plates were made such that the data can be mapped into physical coordinates. The data showed that a large overshoot in heat flux is present at the reattachment location for high ramp angles. For the lowest ramp angle this overshoot is not present. The effect of the Reynolds number on the peak heat fluxes is less clear. Only for the highest Reynolds numbers a decrease is found in peak heat fluxes. A potential reason for this is that the shear layer becomes turbulent instead of transitional. However, this should be investigated further.

Furthermore, spanwise streaks are observed in the reattachment region. Besides the compression waves found in the Schlieren data, this is evidence that there are transitional structures present in the shear layer. A cross sectional view showed that two types of waves are present, big large waves with on top smaller waves. It was not possible to find the magnitude change of these waves on the Stanton number due to aliasing. However, the non-dimension wavelength is found. It turns out that both type of waves decrease for increasing Reynolds numbers. It should be noted that the spreading in the data is large. So to confirm this, additional research is required.

At last, BOS measurements are done to look at the density changes in the shear layer. Unfortunately, the measurement set-up was not accurate enough to find any density changes. Instead an investigation is done to find the deficiency in the set-up. It showed that probably the lack of light in the test section was the cause. This resulted in that there are not sufficient intensity differences in the images for a proper cross correlation.

Contents

List of Symbols

Greek Symbols

β	Shock wave angle	$\circ$
γ	Ratio of specific heats	$(-)$
δ	Boundary layer thickness	m
δ^*	Boundary layer displacement thickness	m
ϵ	Emissivity	$(-)$
Λ	Non-dimensional wavelength	$(-)$
λ	Wavelength	(m)
μ	Mach angle, dynamic viscosity	$\circ$, $kg/(m \cdot s)$
ν	Kinematic viscosity	$Pa \cdot s$
ρ	Density	kg/m^3
σ	Growth rate	$(-)$
φ	Deflection angle	$\circ$
φ_{SL}	Shear layer angle	$\circ$

Arabic Symbols

a	Speed of sound	m/s
C	Speed of light	m/s
c	Thermal capacity	$J/(kg \cdot K)$
c_f	Local skin-friction coefficient	$(-)$
c_h	Stanton number based on $(T_t - T_w)$	$(-)$
c_p	Specific heat at constant pressure	$J/(K \cdot kg)$
d	Diameter	m
E_{b_λ}	Spectral exitance for a black body	$W/(m^2 \cdot m)$
h	Enthalpy	J/kg
I	Intensity of a signal	$(-)$
K	Gladstone-Dale constant	$m^3/(kg \cdot m)$
k	Thermal conductivity	$W/(m \cdot K)$
L	Length of the storage tube	m
M	Mach number	$(-)$
n	Refractive index	$(-)$

p	Pressure	Pa, (N/m^2)
Pr	Prandtl number	$(-)$
q_s	Heat flux	W/m^2
R	Specific gas constant	$J/(kg \cdot K)$
Re	Reynolds number	$(-)$
St	Stanton number based on $(h_{aw} - h_w)$	$(-)$
T	Temperature	K
t	Time	s
u	Velocity	m/s
x	Streamwise coordinate	mm
y	Spanwise coordinate	mm
z	Height coordinate	mm

Superscripts & **accents**

$*$	Reference temperature state

Subscripts

0	Start of the interaction
∞	Free stream properties
a	Ambient
aw	Adiabatic wall
e	Edge of boundary-layer
L	Ramp leading edge
r	Recovery
s	Surface
t	Total quantity
w	Wall quantity
x	Locally

1 Introduction

1.1. Historical Background

The start of Hypersonic research can be traced back until the end of WW2. During this period the hypersonic flight regime was primarily investigated for military dominance, which resulted in the first rocket that could reach a Mach number just below the hypersonic speed region: the V2.

When the war ended, the responsible scientists for the V2 were brought back to the Sovjet Union and the United States. There they continued working on hypersonic missiles. They found, that the pointy shape of the V2 could not withstand the thermal loads present at hypersonic speeds and design changes were required.

During the space race, reentry vehicles were developed which could withstand high hypersonic Mach numbers. These capsules operated at very low L/D ratios. A low L/D ratio results in a near ballistic reentry which results in a deceleration at low altitudes where high densities are present. This creates very high thermal loads on the structure. Furthermore, a ballistic reentry vehicle has the downsides of high g-loads and low maneuverability.

Another approach is to do the complete opposite and use vehicles with a considerable higher L/D ratio. This approach counters all the downsides stated above. Low maneuverability can be solved using conventional control surfaces. The g-loads can be lower because it is possible to extend the deceleration time. Furthermore, because the deceleration can be started at higher altitudes, it is possible to lower the overall thermal loads loads.

However, these benefits come with a cost. Lifting vehicles have a more complex geometry with junctions, sharp edges and compression surfaces. At these locations very high local heat fluxes can be present due to shock wave boundary-layer interactions. Furthermore, these heat fluxes are present for a prolonged time due to the longer deceleration time.

1.2. Control Surfaces in Hypersonic Flows

One of the most critical locations is on deflected control surfaces. Figure 1.1 shows the Space Shuttle. This is the only lifting reentry vehicle that was used regularly and had control surfaces for maneuvering. The figure shows that the Space Shuttle had elevons and rudders for controlability and a body flap to trim the vehicle. During the first flight, the body flap caused a trim anomaly. It was found, that at a certain flight phase a relative pitching up motion of $\Delta C_M = 0.03$ was found compared to predictions. Later investigations showed that this error came from neglecting the compressibility and viscous interaction effects on the body flap [1].

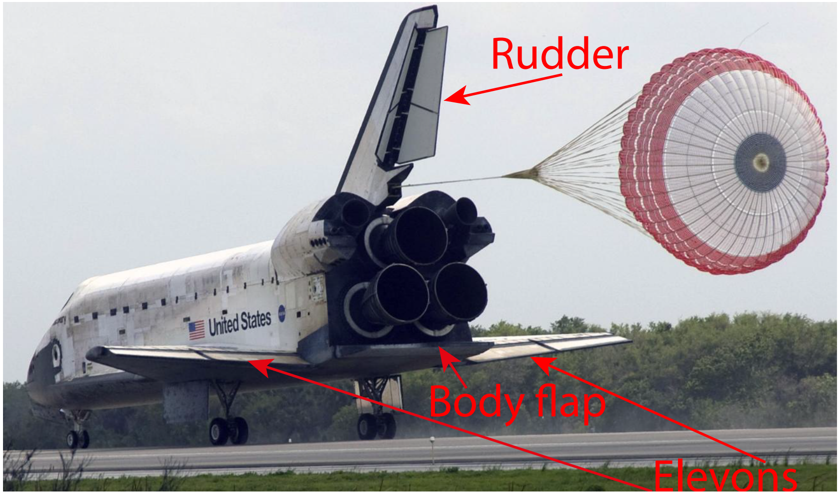

Figure 1.1: Control surfaces on the Space Shuttle. [2]

The working principle of a control surface is based on creating a pressure difference between the top and the bottom. In supersonic flow, this is done by creating a shock wave on the side that is turned into the flow. On the other side an expansion fan is present that expands the flow. On the compressing side, severe shock wave boundary-layer interactions can be present that can create significant elevated heat fluxes.

1.3. The Hypersonic Environment

It is commonly known that the definition of subsonic flow and supersonic flow lies at $M = 1$. However, the boundary between the supersonic and hypersonic flow is not so clearly defined. This is because the characteristics of a hypersonic flow become gradually more important when increasing the Mach number. Conventionally the limit of supersonic flow lies at a Mach number of 5.

Going higher than Mach 5, the oblique shock wave angle starts to become very small and as a result lies very close to the surface of the object. Furthermore, the boundary-layer becomes thicker at higher Mach numbers. Combining these two effects results in an interaction between the shock wave and boundary-layer. Also, the temperature effects in the boundary-layer cannot be ignored anymore and have a profound effect on the heat flux. Furthermore, very high temperature can be reached in hypersonic flows, especially in shock wave boundary-layer interactions. At these temperatures the chemistry of gasses becomes important and as a result the ratio of specific heats (γ) are not constant anymore.

At last, hypersonic conditions are usually found during reentry of space vehicles. During this reentry a lot of different velocity and densities are encountered. As a result, a large Reynolds number range is present during reentry. This has a profound effect on the boundary-layer, resulting in the presence of laminar, transitional and turbulent boundary-layers in different flight phases. The state of the boundary-layer has a big influence on the heat fluxes present on the surface. A turbulent boundary-layer can increase the heat flux with three times the value found in a laminar boundary-layer [3]. This shows the importance of correctly predicting the boundary-layer state during reentry.

1.4. Research Objective

The aim of this thesis is to investigate the strong shock wave boundary-layer interactions found in hypersonic compression ramp flows with emphasis on the structures found in the shear layer. This is done by doing Schlieren, Quantitative InfraRed Thermography (QIRT) and Background Orientated Schlieren (BOS) measurements in the HTFD wind tunnel in Delft.

The Schlieren measurements are used to investigate the general flow topology of the shock wave boundary-layer interaction and to give qualitative information on the shear layer. The QIRT data is then used to give a quantitative description of the heat fluxes on the ramp. At last, it was intented to use BOS for spanwise information on the shear layer, but it did not work out as expected.

1.5. Report Outline

This report consists of eight chapters. Chapter 2 gives an introduction in hypersonic compression ramp flows. This consists of describing the general flow lay-out of compression ramp flows. Also typical pressure and heat flux distributions are given. Furthermore, theoretical approximations are stated which will later be tested against the experimental results.

After that, Chapter 3 describes the wind tunnel used for the experiments. Also, the design and design decisions for the wind tunnel model are explained in this chapter.

Chapter 4 gives the physical principles and applicability of the different flow measurement techniques used during the experiments. Next to that, the data processing techniques are explained.

Chapter 5, 6 and 7 explain the results found for respectively the Schlieren, QIRT and BOS measurement campaigns.

In Chapter 8 the conclusions found in the report are discussed. At last, some recommendations for future research are given in Chapter 9.

2

Hypersonic Compression Ramp Flows

In this chapter the flow characteristics of a compression ramp flow over a flat plate are explained. This is done to give an idea of the background of the performed experiments. Also, it helps understanding the usefulness of the results and aids understanding them.

First, the inviscid case is explained in Section 2.1. The results of the inviscid case act as input for the viscous case which is explained in Section 2.2. In that section an method is given to estimate the flat plate boundary-layer properties such as the incoming boundary-layer thickness, skin-friction coefficient and Stanton number. These properties are important for the flow topology of the weak interaction and strong interaction between the shock wave and boundary-layer, which is treated after that. Then typical pressure and heat flux distributions are discussed in respectively Section 2.3 and Section 2.4. Both these quantities are of great importance in compression ramp flows as the pressure influences the mechanical loads and the heat flux causes the thermal loads present on the ramp. At last, some commonly used correlations related to compression ramps are given in Section 2.5.

2.1. Inviscid Flow Topology

In Figure 2.1, a schematic representation of a compression ramp on a flat plate is given. In order to compare the results obtained in this chapter with the results in Chapter 5 and Chapter 6, the set-up is equivalent to the set-up explained in Section 3.2. This means, that the flat plate is at an angle of 1° and a leading edge shock is present.

The inviscid analysis starts with the inflow conditions explained in Section 3.1.4. As the flow accelerates throughout the entire test section, the inflow Mach number has to be estimated. The following calculations are therefore performed at $M_0 = 7.5$. The importance of the inviscid calculations lies in the fact that even when viscosity is added, the majority of the flow is still inviscid. Also, the inflow conditions after the leading edge shock are not affected by viscous phenomena. This section will quickly explain the inviscid field and how it is calculated.

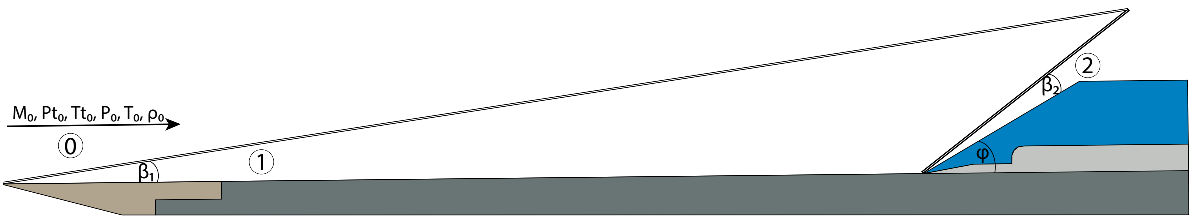

Figure 2.1: The inviscid flow topology of the experiments.

The strength of an oblique shock wave depends greatly on the shock wave angle. The relation between the incoming Mach number, the flow deflection and the shock wave angle is the following:

$$\tan\varphi = \frac{2}{\tan\beta}\frac{M_0^2\sin\beta^2 - 1}{M_0^2\left(\gamma + \cos 2\beta\right) + 2} \tag{2.1}$$

After solving for the shock wave angle (β), the normal component of the flow with respect to the shock wave is calculated using the following equation:

$$M_{n_0} = M_0 \sin\beta \tag{2.2}$$

This normal component can then be plugged into the normal shock wave jump equations. For the normal component of the Mach number after the shock wave, this is the following:

$$M_{n_1}^2 = \frac{1 + \left(\frac{\gamma-1}{2}\right) M_{n_0}^2}{\gamma M_{n_0}^2 - \left(\frac{\gamma-1}{2}\right)} \tag{2.3}$$

For the thermodynamic variables the following equations are used:

$$\frac{\rho_1}{\rho_0} = \frac{(\gamma+1) M_{n_0}^2}{2 + (\gamma-1) M_{n_0}^2} \tag{2.4}$$

$$\frac{p_1}{p_0} = 1 + \frac{2\gamma}{\gamma+1}\left(M_{n_0}^2 - 1\right) \tag{2.5}$$

$$\frac{T_1}{T_0} = \frac{p_1}{p_0}\frac{\rho_0}{\rho_1} \tag{2.6}$$

The total temperature of the flow remains constant over a shock wave. The total pressure jump is calculated using:

$$\frac{p_{t_1}}{p_{t_0}} = \left(\frac{(\gamma+1) M_{n_0}^2}{(\gamma-1) M_{n_0}^2 + 2}\right)^{\frac{\gamma}{\gamma-1}} \left(\frac{\gamma+1}{2\gamma M_{n_0}^2 - (\gamma-1)}\right)^{\frac{1}{\gamma-1}} \tag{2.7}$$

The last step is to convert the normal component of the Mach number back to the total Mach number parallel to the geometry:

$$M_1 = \frac{M_{n_1}}{\sin\beta - \varphi} \tag{2.8}$$

The example given above is for the leading edge shock wave. The variables after the shock wave due to the compression ramp are computed in a similar way. This time, instead of using the inflow conditions before the leading edge shock wave, the conditions after the leading edge shock wave have to be used as input.

From these calculations the flow properties stated in Table 2.1 are found. These values will be used in the next section, as well as in Chapters 5 and 6 to compare the results with the theoretical values.

Table 2.1: Quantities at different stages of the inviscid compression ramp flow at $M_0 = 7.5$.

Stage	θ (°)	β (°)	M	ρ (kg/m^3)	p (Pa)	T (K)	p_t (Pa)	T_t (K)
0	0	/	7.5	0.035	470	47.3	$30.23 \cdot 10^5$	579
1	1	8.3	7.29	0.040	564	49.8	$30.22 \cdot 10^5$	579
2	31	39.65	2.50	0.19	$14.1 \cdot 10^3$	259.6	$24.53 \cdot 10^5$	579

2.2. Viscous Flow Topology

In this section the viscous flow topology is explained. First, this is done for the flat plate. After that the shock wave boundary-layer interaction due to the presence of the ramp will be treated.

2.2.1. Reference Temperature Method

The reference temperature method is used to determine boundary-layer properties like the boundary-layer thickness (δ), skin friction coefficient (c_f) and Stanton number (St). The method is based on the fact that the only difference between compressible boundary-layers and incompressible boundary-layers is the temperature distribution in the boundary-layer. To compensate for this, the incompressible boundary-layer equations have to be applied at a reference temperature (T^*).

The flow topology of the flat-plate is shown in Figure 2.2. The edge of the boundary-layer is shown in orange and is steadily growing when traveling from the leading edge. As the boundary-layer starts growing after the leading edge shock, the conditions at stage 1 of Table 2.1 have to be used.

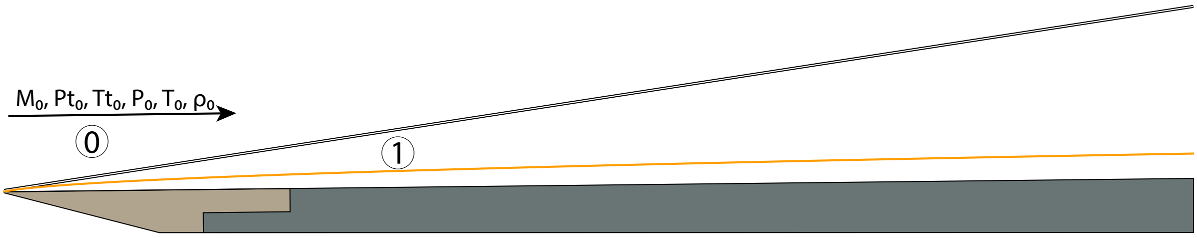

Figure 2.2: The viscous flow topology over the flat plate.

As said, the starting point is to obtain a reference temperature at which the other quantities are calculated. The equation used is the following [3]:

$$\frac{T^*}{T_e} = 1 + 0.032 M_e^2 + 0.58\left(\frac{T_w}{T_e} - 1\right) \tag{2.9}$$

It shows that the reference temperature depends on the wall temperature, the temperature at the edge of the boundary-layer and the Mach number at the edge of the boundary-layer. At the edge of the boundary-layer the values are equal to the inviscid values in region 1. This means that $M_e = M_1 = 7.29$ and $T_e = T_1 = 49.8$ K. The only variable that is still unknown is the wall temperature (T_w) which is found using the following equation:

$$\frac{T_w}{T_e} = 1 + r\frac{\gamma - 1}{2} M_e^2 \tag{2.10}$$

Where r is the recovery factor and is equal to $r = \sqrt{Pr}$. The Prandtl number (Pr) is approximately constant and equal to $Pr = 0.71$. Plugging in all the values gives a reference temperature of $T^* = 393.1$ K.

In order to find the boundary-layer thickness of the boundary-layer, the incompressible flow relation has to be used at the reference temperature. The incompressible Blasius boundary-layer relation is as follows [4]:

$$\delta = \frac{5x}{\sqrt{Re_x^*}} \tag{2.11}$$

The local Reynolds number must then be computed at the reference values as shown in:

$$Re_x^* = \frac{\rho^* u_e x}{\mu^*} \tag{2.12}$$

The reference density is computed as follows:

$$\rho^* = \frac{p_\infty}{RT^*} \tag{2.13}$$

In this equation, T^* is the reference temperature computed above. In the boundary-layer, $\frac{\partial p}{\partial y} = 0$ meaning that the pressure at the edge of the boundary-layer is imposed throughout the boundary-layer. Therefore $p^* = p_e = p_1$. The dynamic viscosity is also a function of temperature and therefore it has to be evaluated at the reference temperature. This is done using Sutherland's law:

$$\frac{\mu^*}{\mu_{ref}} = \left(\frac{T^*}{T_{ref}}\right)^{\frac{3}{2}} \frac{T_{ref} + S}{T^* + S} \tag{2.14}$$

Sutherland's law depends on several reference conditions which are stated in Table 2.2. The velocity at the edge of the boundary-layer equals the value outside the boundary-layer which is equal to the velocity in region 1. By using the temperature and Mach number it is computed in the following way:

$$u_e = M_1\sqrt{\gamma R T_1} \tag{2.15}$$

Table 2.2: Reference quantities for Sutherlands law.

T_{ref} (K)	μ_{ref} $(kg/(m\cdot s))$	S (K)
273.15	$1.716\cdot 10^{-5}$	110.4

Now that the local Reynolds number is known, it is plugged into Equation 2.11. Plotting the boundary-layer thickness as a function of x gives the line in Figure 2.3. The figure shows, that at the location of the ramp around 415 mm from the leading edge, a boundary-layer thickness of 6.7 mm is expected.

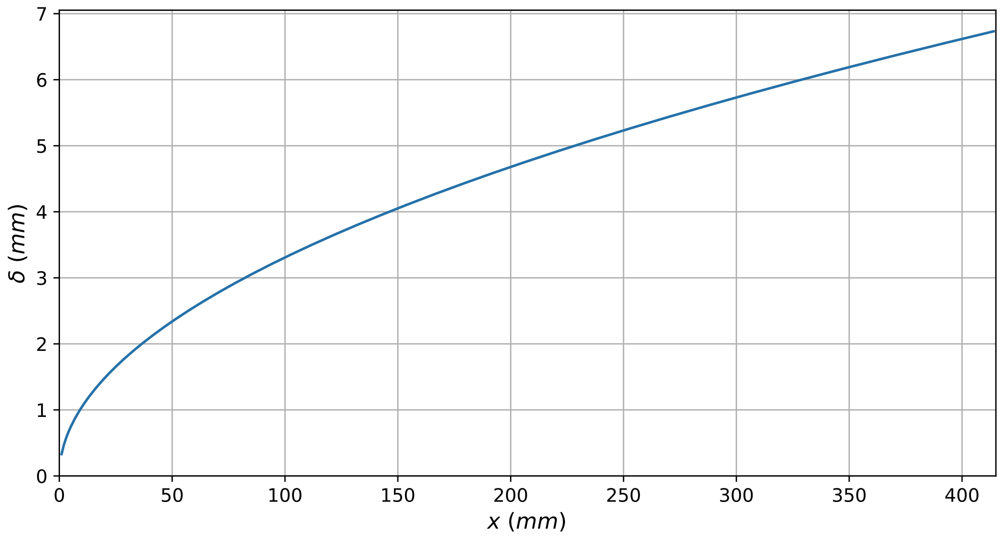

Figure 2.3: Boundary-layer thickness (δ) as function of x.

Apart from Equation 2.11, several other incompressible flow relations exist for a flat plate. The for compressibility corrected relation for the skin friction coefficient is the following:

$$c_f = \frac{0.664\sqrt{C^*}}{\sqrt{Re_x}} \tag{2.16}$$

In this equation, the incompressible relation is corrected with C^*, which is given by:

$$C^* = \frac{\rho^*\mu^*}{\rho_1\mu_1} = \frac{T_1\mu^*}{T^*\mu_1} \tag{2.17}$$

The ratio of dynamic viscosity is calculated using Sutherland's law shown in Equation 2.14. This results in the following expression:

$$C^* = \left(\frac{T^*}{T_1}\right)^{1/2} \frac{T_1 + S}{T^* + S} \tag{2.18}$$

Using Reynolds analogy the relation of the Stanton number is derived, which is the following:

$$St = \frac{0.332}{\sqrt{Re_x}}\sqrt{C^*}\left(Pr^*\right)^{-\frac{2}{3}} \tag{2.19}$$

In the last equation the Prandtl number (Pr) is evaluated at reference conditons using the following equation:

$$Pr^* = \frac{\mu^*}{c_p^*}k^* \tag{2.20}$$

With $c_p^* = 1004\ J/(K\cdot kg)$. The thermal conductivity (k^*) is evaluated in the same way as the dynamic viscosity (μ):

$$\frac{k^*}{k_{ref}} = \left(\frac{T^*}{T_{ref}}\right)^{\frac{3}{2}} \frac{T_{ref} + S_k}{T^* + S_k} \tag{2.21}$$

The reference values are found in Table 2.3. Plugging in all the values gives Figure 2.4 for the skin friction coefficient and Figure 2.5 for the Stanton number. The Stanton number will act as validation for the data reduction method explained in Section 4.3.4.

Table 2.3: Reference quantities for Sutherlands law.

T_{ref} (K)	k_{ref} $(W/(m \cdot K))$	S_k (K)
273.15	0.0241	194

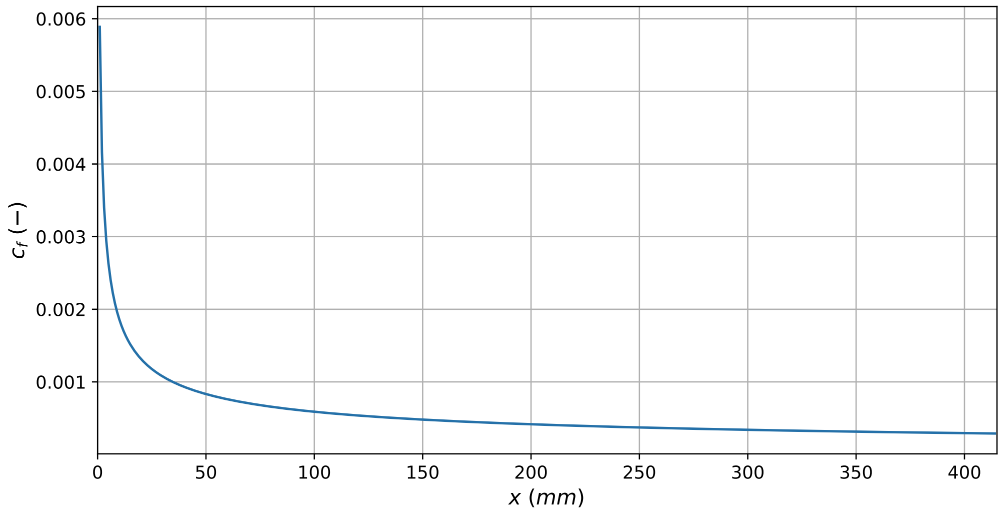

Figure 2.4: Local skin friction coefficient (c_f) as function of x.

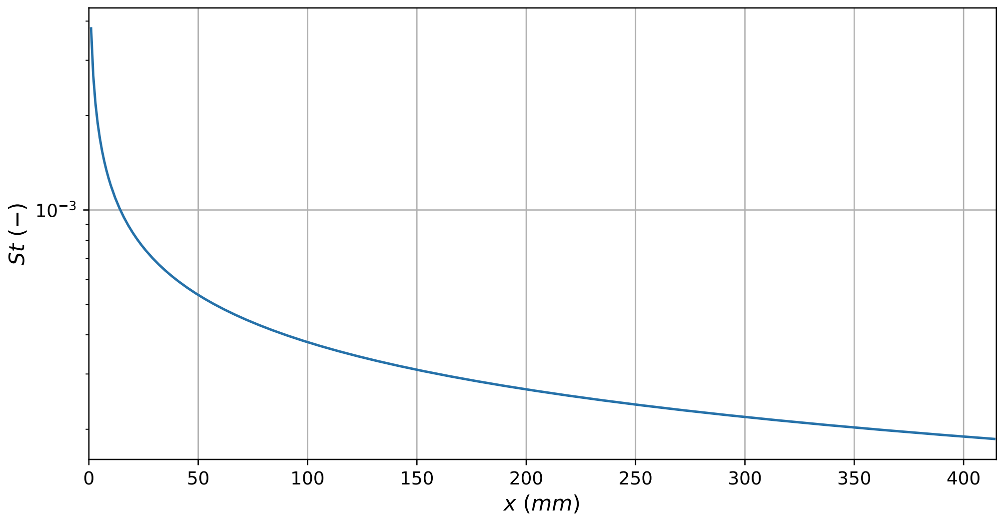

Figure 2.5: Stanton number (St) as function of x.

2.2.2. Weak Shock Wave Boundary-Layer Interactions

In the inviscid case the complete flow is supersonic, meaning that a pressure increase cannot propagate upstream. As a result, the shock wave starts at the leading edge of the ramp. When the boundary-layer is added the flow topology changes. This section discusses the case where the flow is only slightly changed. This is called a weak shock wave boundary-layer interaction.

In Figure 2.6 the flow field is given. Still the leading edge shock wave and the shock wave due to ramp are present. Also, the boundary-layer (in orange) seems to be unaffected.

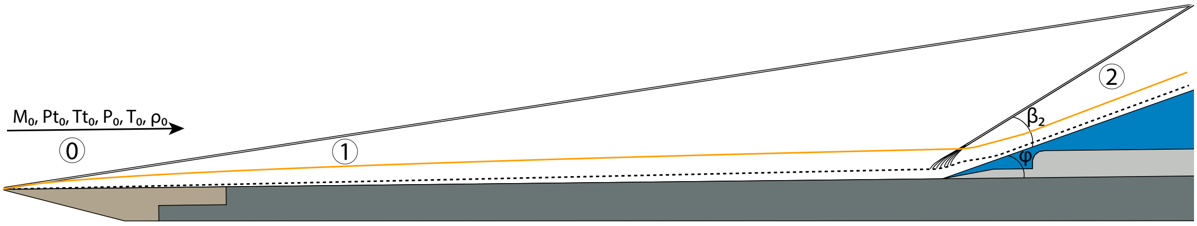

Figure 2.6: The flow topology for a weak shock wave boundary-layer interaction.

When zooming in on the region near the compression ramp, the flow of Figure 2.7 is found. Because of the no slip condition at the wall, the flow velocity is zero at the wall. The boundary-layer is characterized by a velocity distribution which starts with zero at the wall and equals the free stream velocity (u_1) at the end of the boundary-layer. This means that at some point in the boundary-layer profile, the Mach number gets below 1. This is shown by the dashed line in Figure 2.7. Underneath this line the flow is subsonic.

Through this subsonic channel the pressure increase, imposed by the ramp propagate upstream. This locally reduces the velocity resulting in that the subsonic channel dilates to preserve mass conservation. Because of this dilation of the boundary-layer, several compression waves form locally. These compression waves coalesce in the free-stream into a shock wave. When all the compression waves have coalesced, the shock wave in the free-stream equals the shock wave that would be obtained in the inviscid case.

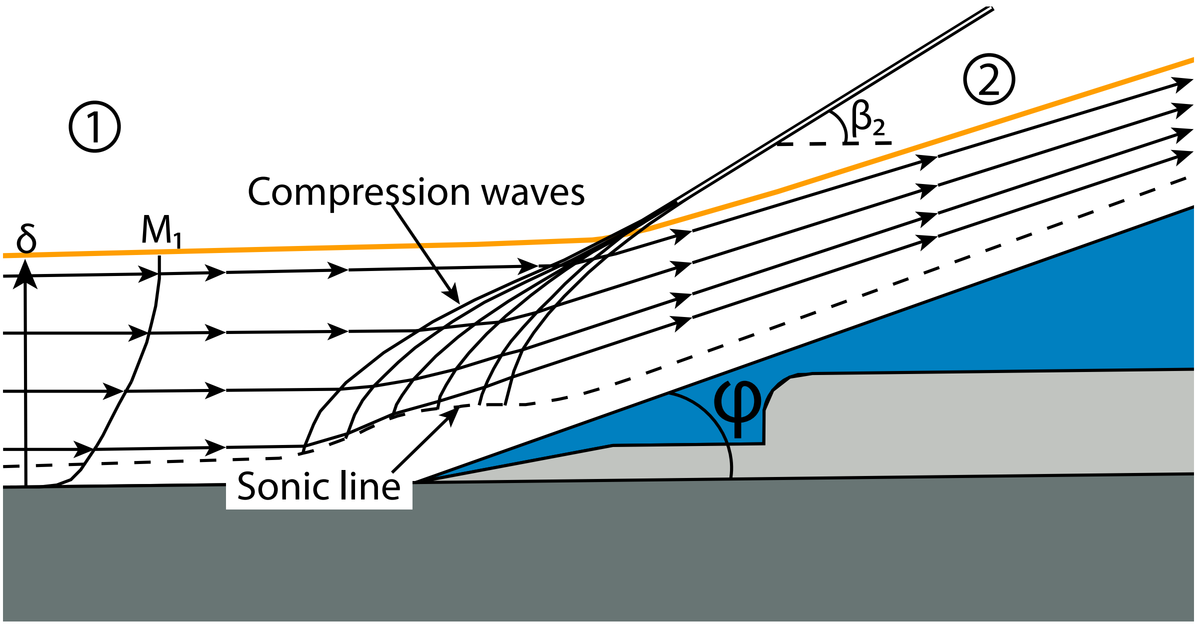

Figure 2.7: Close up of a weak shock wave boundary-layer interaction.

2.2.3. Strong Shock Wave Boundary-Layer Interactions

When the compression ramp angle is further increased, the strength of the required shock wave is also increased. This means that a larger adverse pressure gradient is present in the subsonic channel. At some point the boundary-layer cannot cope with the adverse pressure gradient anymore and it separates. This point is called the incipient separation point. This phenomena significantly alters the flow field as shown in Figure 2.8.

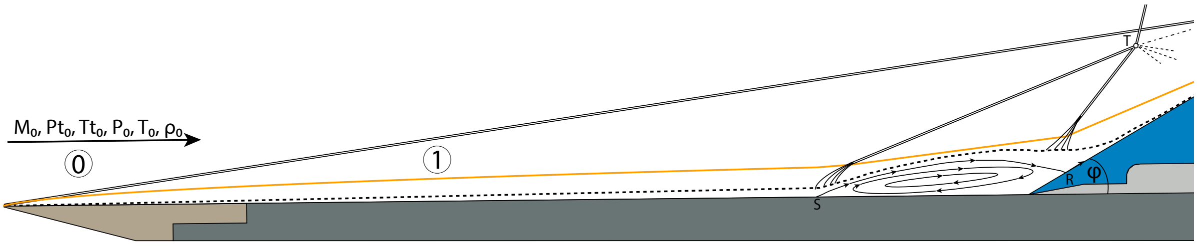

Figure 2.8: The flow topology for a strong shock wave boundary-layer interaction.

In Figure 2.9, a close-up of the shock wave boundary-layer interaction is given. On the left it is clearly visible that compression waves form on the separation bubble. The compression waves coalesce together into the separation shock. On top of the separation bubble a strong shear layer is present which travels downstream. Near the ramp, the flow has to be deflected further in order to follow the ramp. This creates compression waves that focus into the reattachment shock. Just downstream of the reattachment, the boundary-layer on the ramp reaches its thinnest point and therefore the highest peak heating is expected at that location.

Because the Mach number is first reduced after the separation shock wave, the reattachment shock wave always has a larger shock angle. This means, that the two shock waves intersect at point T creating a shock-shock interaction. At the Mach numbers of these experiments, an Edney Type VI interaction is expected. Above the shock-shock interaction, the shock wave which is expected from the inviscid calculations is present.

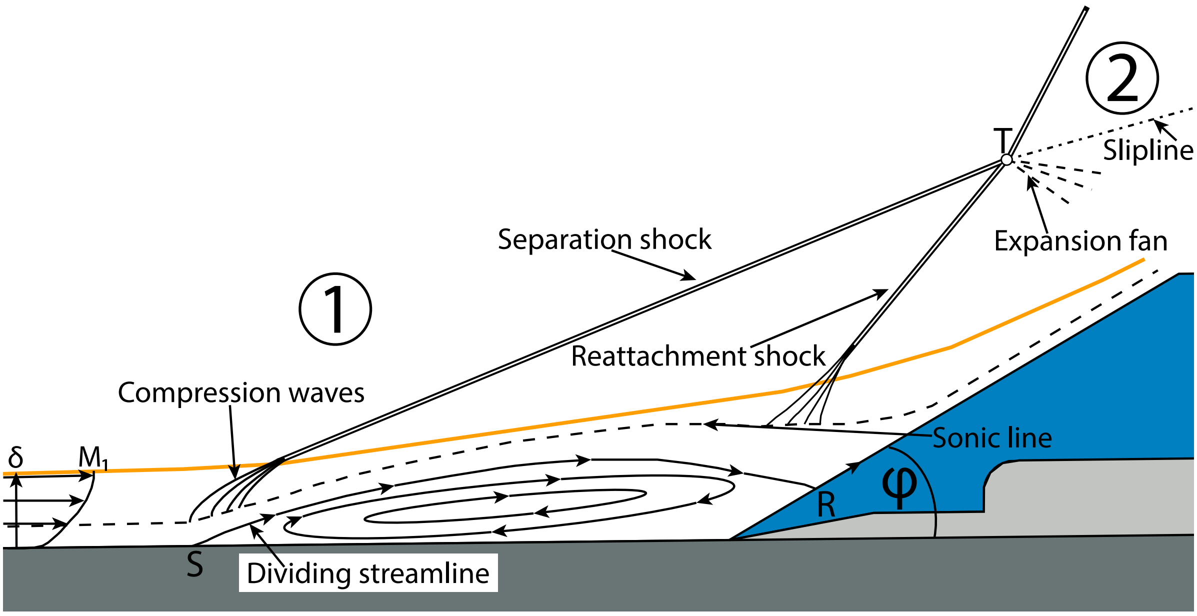

Figure 2.9: Close up of a strong shock wave boundary-layer interaction.

2.3. Typical Pressure Distributions

In this section typical pressure distributions are given for the compression ramp flows. In Figure 2.10 the expected pressure distributions for an inviscid flow and weakly interacting viscous flow are given.

Behind the leading edge shock wave, the pressure (p_1) is constant both in the viscous case and the inviscid case as $\partial p/\partial y = 0$ in the boundary-layer. The only observed difference between the viscous and inviscid case, is the distance it takes before the pressure jump is complete. For the inviscid case this is achieved almost instantly with a shock wave. For the viscous case the pressure jump starts with compression waves due to the presence of a subsonic channel. As the compression waves coalesce into the inviscid shock wave, the final pressure is expected to be the same as the invisicid value.

The location where the pressure starts increasing, is called the interaction origin. The distance between the interaction origin and the ramp is then the interaction length (L_i). Experiments have shown that the interaction length is influenced by the compression ramp angle, the Mach number and the boundary-layer thickness Reynolds number (Re_δ) [5].

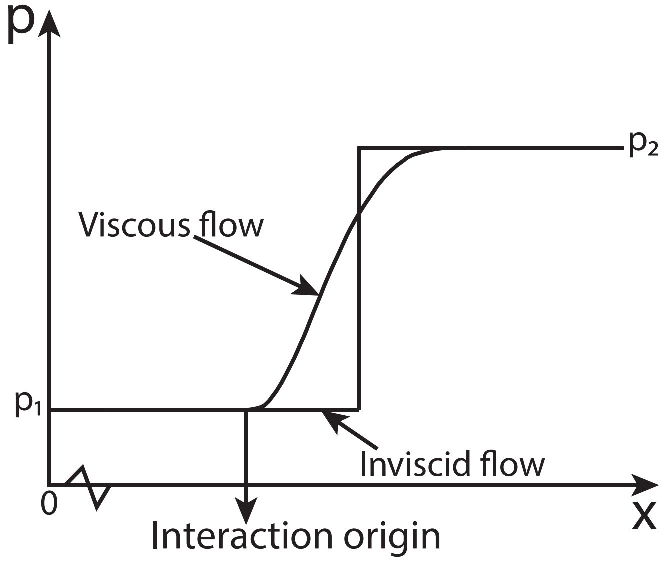

Figure 2.10: Theoretical pressure distribution for a weakly interacting flow.

Figure 2.11 shows the pressure distribution for the strongly interacting flow and the inviscid flow. The inviscid flow still consists of one pressure jump due to one oblique shock wave. The viscous flow now consists of two jumps. The first jump starts with the compression waves coalescing into the separation shock wave. After that the so called plateau pressure is reached. Near the reattachment point, compression waves start to form, which initiates the second pressure rise. When all the compression waves are coalesced, the inviscid flow value is reached.

The interaction origin is now located at the first compression wave of the separation shock, which is much further upstream than for weak shock wave boundary-layer interactions. The distance between the interaction origin and the ramp leading edge is called the separation length (L_{sep}).

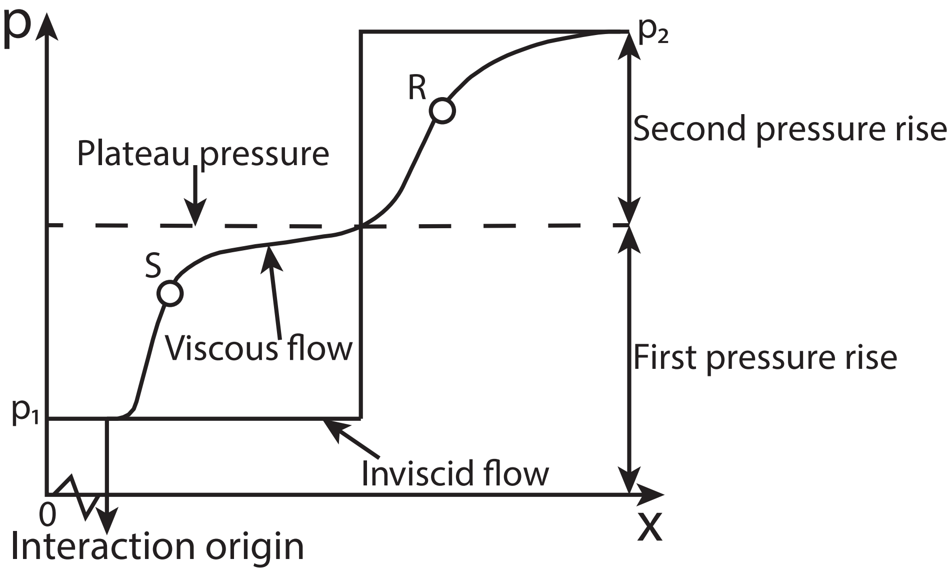

Figure 2.11: Theoretical pressure distribution for a strongly interacting flow.

Measured pressure distributions for different compression ramp angles at hypersonic Mach numbers are given in Figure 2.12. For the lowest ramp angles (15°, 26° and 30°) the pressure profile of the weakly interacting flow is found. After the interaction, they nicely converge to the inviscid value for their respective ramp angle. Also, increasing the ramp angle increases the interaction length (L_i).

When the compression ramp angle is further increased, pressures higher than the inviscid pressure are found. This is different from the expectations given by Figure 2.11. The reason for this, is that in the hypersonic regime the shock waves angles are very small. This means that triple point T in Figure 2.9 lies very closely to the boundary-layer or even inside the boundary-layer. The total compression by the separation shock wave and reattachment shock wave results in a higher pressure increase than only the single inviscid shock wave. This causes the peak pressures shown in Figure 2.12, after the peak an expansion fan is present which reduces the peak pressure to the expected inviscid value.

For the highest compression ramps, the pressure distributions clearly reach the same plateau pressure. The only thing that changes when increasing the ramp angle, is the separation length. This phenomena is explained in Section 2.5.1. This section gives theoretical evidence that the plateau pressure is independent of the compression ramp angle.

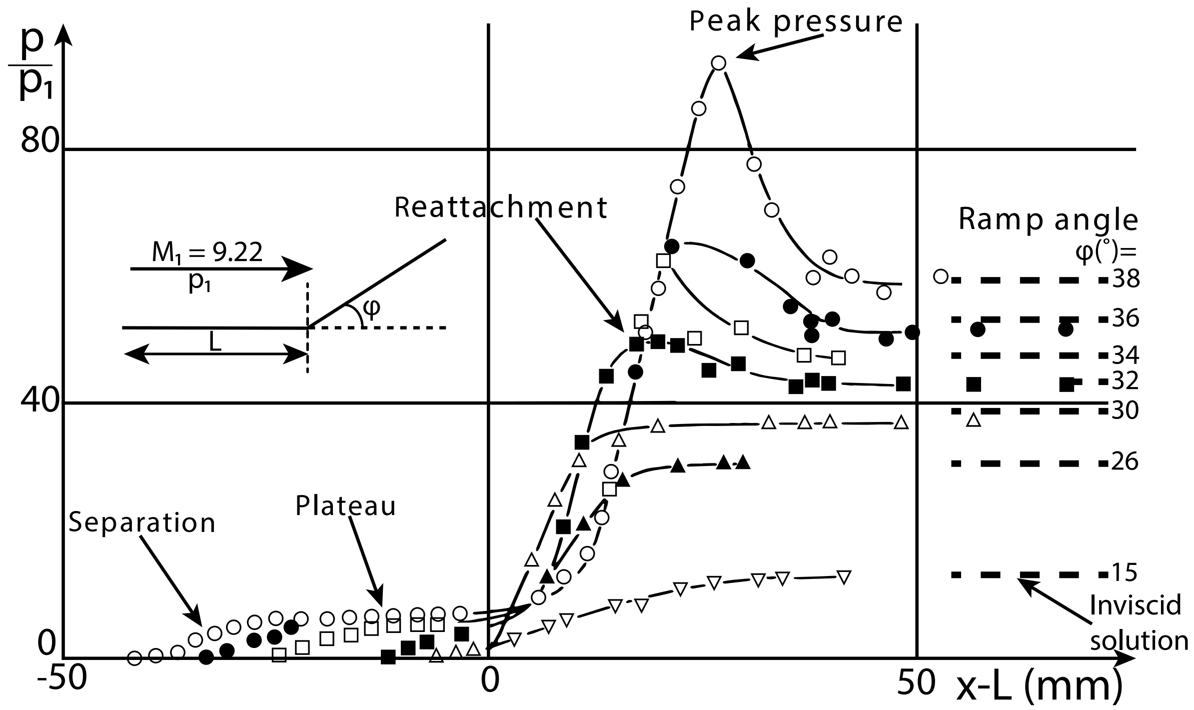

Figure 2.12: Measured pressure distributions over different compression ramp angles at $M_1 = 9.22$, $Re_\delta = 4 \cdot 10^5$ and $T_w/T_0 = 0.28$ [6].

2.4. Typical Heat Flux Distributions

After looking at different pressure distributions, this section will show typical heat flux distributions over compression ramps. Figure 2.13 gives a theoretical heat flux distribution for a strong shock wave boundary-layer interaction. First, a sharp decrease at the leading edge of the flat plate is seen, this is the same as in Figure 2.5. After that, the heat flux drops due to the increase in boundary-layer thickness.

When reaching the separation point, the heat flux has a significant drop for a laminar flow. This is due to the dead air region underneath the separation bubble. In the case of a turbulent flow, the heat flux increases slightly before reaching a plateau value. This is a result of the large turbulent eddies promoting the exchange of flow near the wall and the outer high energy flow [6].

At the reattachment point, the expected peak in heat flux is seen. This is the result of a very thin boundary-layer near the reattachment point, the so called necking region. The peaks can rise even further due to the presence of high peak pressures as discussed in Section 2.3.

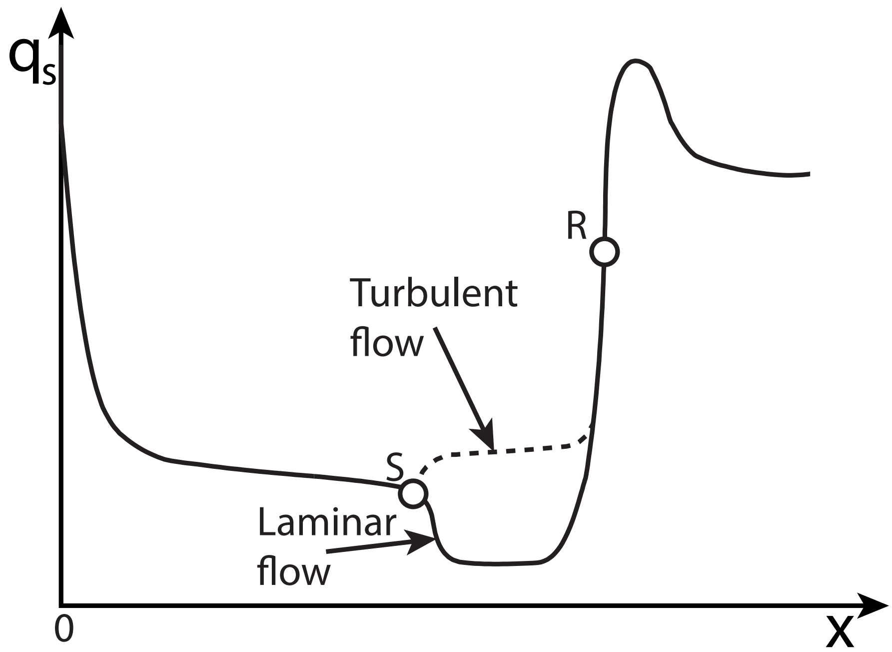

Figure 2.13: Theoretical heat flux distribution for a strongly interacting flow.

Figure 2.14 shows the heat fluxes of the same experiment performed as in Figure 2.12. As expected, there are very high peak heat fluxes present near the reattachment regions. As after separation, the heat flux reaches an elevated plateau, it has to be a turbulent interaction.

Looking at the peak values, the problem of thermal loads in hypersonic flows becomes clearly visible. For the highest compression ramp angle an increase of 36% is found, compared to the already high heat flux after the shock wave boundary-layer interaction. Depending on the inflow conditions, this can result in very high temperatures at the reattachment point.

It is known, that even higher heat fluxes can be found when the shear layer transitions from laminar to turbulent. The large coherent transition structures promote the exchange of energy towards the wall creating even larger peaks either in spanwise or streamwise direction.

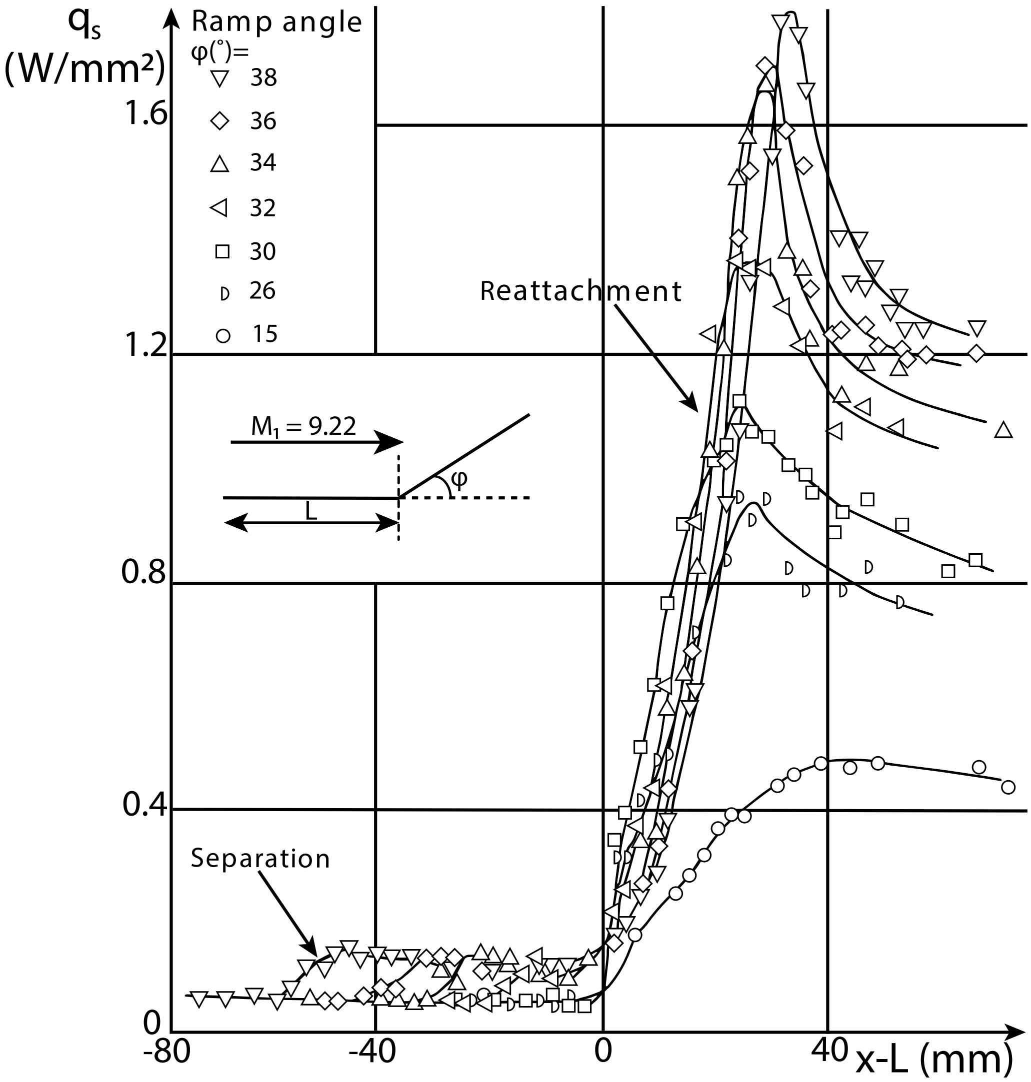

Figure 2.14: Measured heat flux distributions over different compression ramp angles at $M_1 = 9.22$, $Re_\delta = 4 \cdot 10^5$ and $T_w/T_0 = 0.28$ [6].

2.5. Compression Ramp Correlations

This section is used to give some correlations for compression ramp flows. These can be used to predict certain flow phenomena or for designing an experiment. The section is divided in subsections based on the different flow features as seen in the previous flow distributions.

2.5.1. Free-interaction Theory/Plateau Pressure

The characteristics of the flow during separation in supersonic and hypersonic flow can be interpreted by the free-interaction theory [6]. This theory can be used to derive the following equation:

$$\begin{aligned}
&\frac{p(\bar{x}) - p(\bar{x}_0)}{q_0} = F(\bar{x})\sqrt{\frac{2C_{f_0}}{\left(M_0^2 - 1\right)^{1/2}}} \\
&\text{Where :} \\
&\bar{x} = \frac{x - x_0}{L} \\
&F(\bar{x}) = \sqrt{f_1(\bar{x}) f_2(\bar{x})}
\end{aligned} \tag{2.22}$$

In this equation the subscript 0 means the starting location of the interaction. The equation correlates the pressure in the interaction with the pressure at the interaction origin. In Table 2.4 the correlation constants for the pressure at the separation location and the plateau pressure are stated. For the interaction extent the following equation is derived:

$$\frac{L_s}{\delta_0^*} = \sqrt{2\frac{f_2(\bar{x})}{f_1(\bar{x})}}\frac{1}{\sqrt{c_{f_0}}}\left(M_0^2-1\right)^{-\frac{1}{4}} \tag{2.23}$$

Table 2.4: Correlation values for F at the separation point and the plateau value [5]

	F (separation location)	F (plateau value)
Laminar flow	0.8	1.5
Turbulent flow	4.2	6

Equations 2.22 and 2.23 show that the plateau pressure and the interaction extend depend on quantities at the interaction location and not on downstream quantities such as the shock strength or compression ramp angle. This means, that the location of the separation point and the angle of the shear layer are determined only by the required pressure increase for incipient separation. The whole pressure rise required for a compression ramp is therefore split into two parts, a part at the separation shock wave and a part due to the reattachment shock wave. The compression at separation is fixed at the incipient separation value because it is not dependent on the compression ramp angle. This means, that an increase in overall pressure rise requires an additional pressure rise at reattachment. Therefore, increasing the compression ramp angle will increase the peak pressure found at reattachment of the shear layer.

The length of the shear layer is fixed such, that it obtains sufficient momentum to overcome the required reattachment pressure rise. The only possible way to gain momentum is a higher shear layer velocity. This is obtained by increasing the shear layer length. As the reattachment point is fixed, an increase in compression ramp angle will move the separation point forward.

Looking at Figure 2.12, the theory as described above is confirmed. Increasing the compression ramp angle indeed increases the shear layer length. Also, a nearly constant plateau pressure is found for different compression ramp angles. As a result, the compression at reattachment is increased for higher compression ramp angles.

The effect of the Reynolds number can also been found using the free-interaction theory. It is observed that the overall pressure increase is lowered when increasing the Reynolds number. Furthermore, the interaction extent is increased with increasing Reynolds number. As a result, a stronger shock wave is required to separate the boundary-layer at lower Reynolds numbers. This behavior is confirmed for Reynolds numbers up to $Re_\delta = 10^5$, for higher Reynolds numbers the effect is reversed. Then the boundary-layer is less prone to separation with increasing Reynolds number. The reason that free-interaction is not able to describe this behavior, is that inertia forces are neglected and only the viscous forces are taken into account in the form of the skin friction coefficient (c_{f_0}). At higher Reynolds numbers the viscous contribution reduces compared to the inertial forces, so the error becomes larger.

2.5.2. Incipient Separation

A lot of shock wave boundary-layer correlations depend on the hypersonic viscous parameter given by the following equation:

$$\begin{aligned} \chi_{LE} &= \frac{M_\infty^3\sqrt{C}}{\sqrt{Re_L}} \\ \text{Where:} & \\ C &= \frac{\rho_w \mu_w}{\rho_\infty \mu_\infty} \end{aligned} \tag{2.24}$$

In this equation, C is the Chapman-Rubesin linear viscosity parameter. A correlation for the incipient separation compression ramp angle (φ) is given by [7]:

$$M_\infty \varphi_{incip} = 4.32\sqrt{\chi_{\varepsilon_L}} \tag{2.25}$$

In this case the correlation depends on a wall temperature corrected hypersonic viscous parameter which is given by:

$$\chi_{\varepsilon_L} = \frac{\gamma - 1}{\gamma + 1}\left(0.664 + 1.73\frac{T_w}{T_t}\right)\chi_L \tag{2.26}$$

2.5.3. Shear Layer Length

Several relations exist to determine the length of the shear layer. In this section, two are discussed, one which is partly based on theory and another one which is correlated to several experiments performed in wind tunnels.

The following relation is based on computational results of 2D shock wave boundary-layer interactions [8]:

$$\frac{L_{sep}}{\delta_0^*} = 4.4\frac{p_3 - p_{inc}}{p_1 \cdot \chi} \tag{2.27}$$

The p_{inc} is found using a relation that is partly based on the free-interaction theory and partly correlated to data:

$$\frac{p_{inc} - p_1}{p_1} = \frac{1}{2}\gamma M_\infty^2 1.85\sqrt{2}\sqrt{\frac{c_{f0}}{\left(M_\infty^2 - 1\right)^{1/2}}} \tag{2.28}$$

The other approximation is based on the correlation of several experiments. These results are combined into Figure 2.15. Based on that figure, a trendline of the form $L_{sep}/\delta_0 = a\left(\frac{(M_0\varphi)^2}{\chi_0}\right)^b$ is correlated to the data. This gives $a = 1.09$ and $b = 2.44$ and results in the following relation [9]:

$$\frac{L_{sep}}{\delta_0} = 1.09\left(\frac{\left(M_\infty\varphi\right)^2}{\chi_0}\right)^{2.44} \tag{2.29}$$

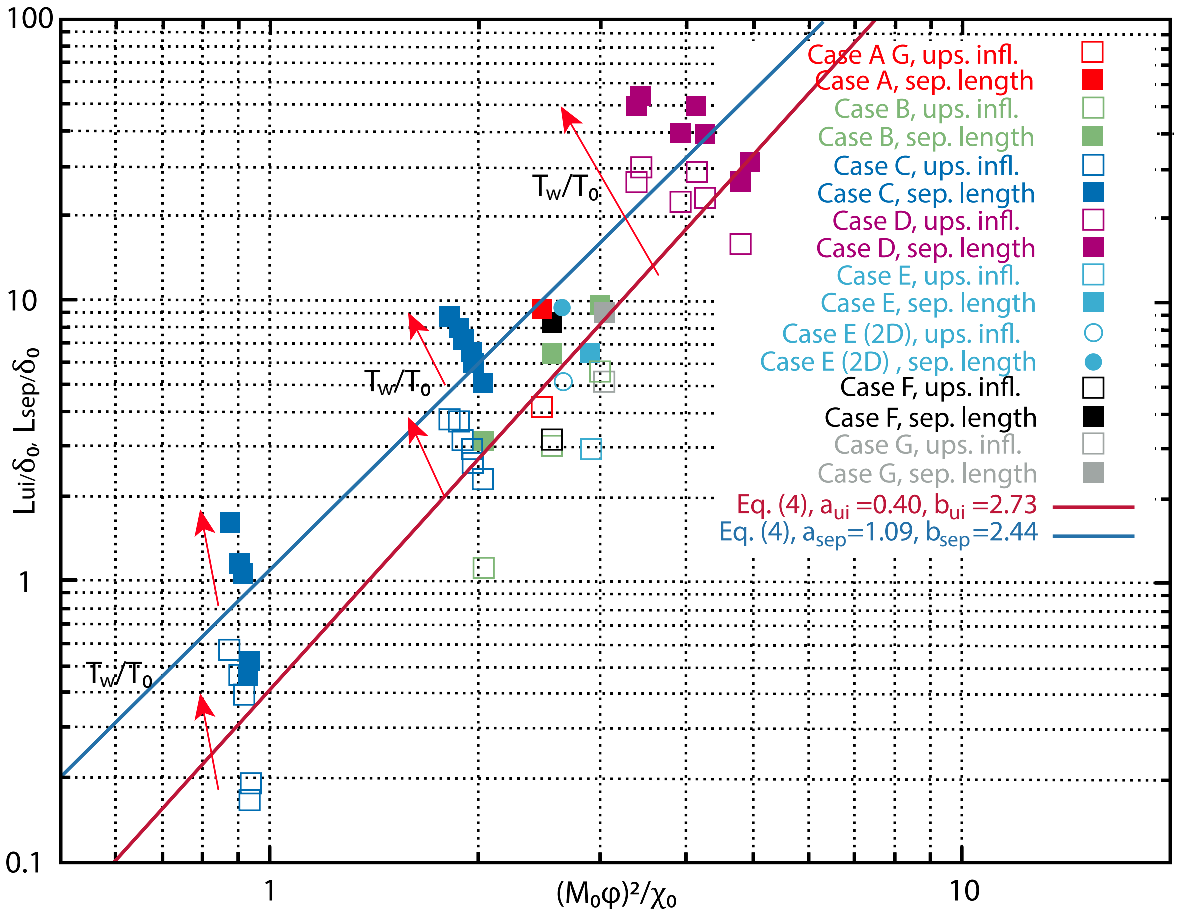

Figure 2.15: Upstream influence and separation length correlation [9].

2.5.4. Peak Heating

As shown in Section 2.4, there are large peaks present in the heat flux distribution near reattachment. There are several relations available to predict the peak heat flux. One of the simpler methods is the following relation [10]:

$$\frac{c_{h_{peak}}}{c_{h_0}} = a\left(\frac{p_3}{p_1}\right)^b_{theoretical} \tag{2.30}$$

In this equation the theoretical inviscid pressure is used to correlate the peak heat flux. The constants a and b depend on the flow state. For turbulent flow $a_{turb} = 1$ and $b_{turb} = 0.8$ is found and for laminar flow $a_{lam} = 0.13$ and $b_{lam} = 1.13$. In the case when the laminar shear layer transitions to a turbulent shear layer, higher peak heat values are expected. The laminar relation is corrected for that in the following way [10]:

$$\frac{c_{h_{peak}}}{c_{h_0}} = 0.468\left(Re_{L_0}\cdot 10^{-6}\right)^{1.85}\left(\frac{p_3}{p_1}\right)^{1.13}_{theoretical} \tag{2.31}$$

Holden in [11] uses instead of the theoretical inviscid pressure jump, the actual pressure jump to correlate the data. The following equation is then found:

$$\frac{c_{h_{peak}}}{c_{h_{ref}}} = \left(\frac{p_{peak}}{p_{ref}}\right)^{0.7} \tag{2.32}$$

A different approach for calculating the peak heat flux is assuming a new very thin boundary-layer near the reattachment point [12]. An approximation of a hypersonic boundary-layer using the reference temperature method explained in Section 2.2.1 is:

$$c_h (Re_x)^n = \frac{A}{s} \left(\frac{u_e p_e}{u_\infty p_\infty} \right)^{1-n} \left(\frac{T_\infty}{T^*} \right)^{1-2n} \left(C^* \right) \left(\frac{T_r - T_w}{T_t - T_w} \right) \tag{2.33}$$

Table 2.5: Correlation values for Equation 2.33 [12].

	n	A	s
Laminar flow	0.5	0.332	$Pr^{2/3}$
Turbulent flow	0.2	0.0296	1

Depending on the boundary-layer state, different correlation constants have to be used. In Table 2.5 the different constants are given. Equation 2.33 can then be used to compute the boundary-layer with origin near the reattachment region. As a reference condition, a normal flat plate boundary-layer with sharp leading edge is used. The peak heat flux can be found by dividing the reattachment boundary-layer with the reference boundary-layer. The following equation is then obtained:

$$\frac{c_{h_{peak}}}{c_{h_{ref}}} = B \left(Re^*_{x_{peak}} \right)^a \left(\frac{p_{peak} u_{peak}}{p_{ref} u_{ref}} \right)^{1-n} \left(\frac{x_{peak}}{L_{peak}} \right)^n \tag{2.34}$$

The different constants are given in Table 2.6. The last thing that is required is the growth length of the boundary-layer (L_{peak}). This length scale is approximated using the following equation:

$$L_{peak} = \frac{\delta_{reattachment}}{\sin\left(\varphi - \varphi_{sep}\right)} \tag{2.35}$$

Table 2.6: Correlation values for Equation 2.34 [12].

	n	a	B
Laminar peaking	0.5	0	1
Turbulent peaking	0.2	0	1
Turbulent peaking and laminar reference	0.2	0.3	0.072

3

Experimental Apparatus

This chapter is used to explain which experimental apparatuses are used in the experiments. This explanation is split into two parts, the first part describes the working principle and the operational envelope of the Hypersonic Test Facility Delft (HTFD) in Section 3.1. Furthermore, the free-stream conditions used during the different tests are given. The second part of this chapter explains the design choices of the models used in the HTFD in Section 3.2.

3.1. Hypersonic Test Facility Delft

The Hypersonic Test Facility Delft (HTFD) is a wind tunnel based on the Ludwieg tube concept. The benefit of using the Ludwieg tube principle is the relatively low turbulence uniform flow, the long run time and the possibility of attaining high unit Reynolds numbers.

3.1.1. Operating Principle

Figure 3.1 gives a schematic representation of the Ludwieg tube principle. As seen in the figure, a Ludwieg tube consist of four main sections: a storage tube, a nozzle, a test section and a vacuum tank.

In the storage tube, the fluid is pressurized and heated to the desired conditions. Between the storage tube and the nozzle, a fast acting piston is placed which holds the fluid into the storage tube at high temperature and high pressure. When the piston is pulled back, the fluid flows into the nozzle where it is accelerated to the desired Mach number depending on the area ratio between the throat and the test section. In the test section the flow then reaches the desired flow conditions. The vacuum tank ensures that there is a sufficient pressure ratio present over the nozzle such that the tunnel is able to start and sustain the flow conditions.

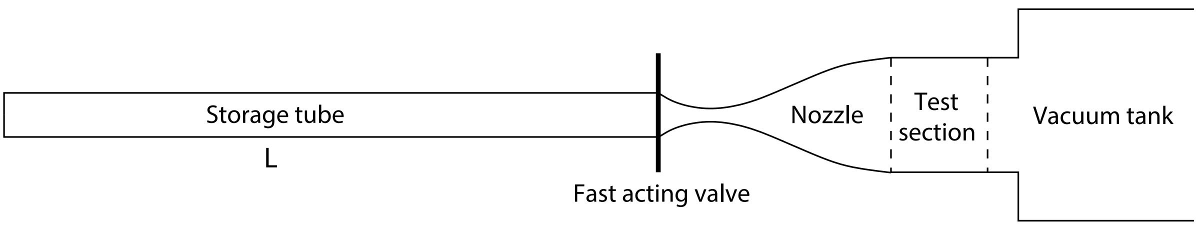

Figure 3.1: Schematic representation of a Ludwieg tube wind tunnel [13].

The process in the storage tube after pulling back the piston is shown in the $t,x-$ diagram given in Figure 3.2. At $t = 0$ the piston is pulled back and an expansion wave starts to form at the valve. This expansion wave moves into the storage tube and away from the valve. At the end of the tube, the expansion wave reflects back towards the nozzle. When the reflected expansion wave reaches the valve again, the run is over.

Because the piston is pulled back very fast, the expansion wave can be treated as a centered expansion wave. The location of the valve is at location $x = 0$ in Figure 3.2. The beginning of the wave is then shown by the line OA and the end by line OSB. The reflection of the wave is shown by the lines ASE and BF. The end of the run is then found at location E at $x = 0$ and $t = t_1$. The conditions over the expansion wave (from 0 to 1) are computed using "simple wave" theory. Along a characteristic the following holds:

$$u_0 + \frac{2a_0}{\gamma - 1} = u_1 + \frac{2a_1}{\gamma - 1} \tag{3.1}$$

In region 0 the air in the tube is at standstill so $u_0 = 0$, this results in:

$$\frac{2a_0}{\gamma - 1} = u_1 + \frac{2a_1}{\gamma - 1} \tag{3.2}$$

Rewriting this equation gives the following expression for the velocity in the storage tube:

$$\frac{u_1}{a_0} = \frac{M_1}{1 + \frac{\gamma-1}{2} M_1} \tag{3.3}$$

During this process, the total temperature also changes. The ratio of the total temperature over the expansion wave may be derived as follows [14]:

$$\frac{T_{t_1}}{T_{t_0}} = \frac{1 + \frac{\gamma-1}{2} M_1^2}{\left(1 + \frac{\gamma-1}{2} M_1\right)^2} \tag{3.4}$$

Because an expansion wave is an isentropic process, the isentropic relations can be used to calculate the pressure jump. This results in:

$$\frac{p_{t_1}}{p_{t_0}} = \left(\frac{1 + \frac{\gamma-1}{2} M_1^2}{\left(1 + \frac{\gamma-1}{2} M_1\right)^2} \right)^{\frac{\gamma}{\gamma-1}} \tag{3.5}$$

As said, the duration of the run is determined by the time it takes for the expansion wave to travel to the end of the tunnel and back again. In Figure 3.2 this point is shown as t_1. The total running time is calculated with the following equation [14]:

$$t_1 = \frac{L}{a_0} \frac{2}{1 + M_1} \left(1 + \frac{\gamma - 1}{2} M_1\right)^{\frac{\gamma+1}{2(\gamma-1)}} \tag{3.6}$$

All of these parameters depend on the Mach number after the expansion wave. The Mach number is found using conservation of mass and depends directly on the ratio between the storage tube diameter and the critical throat diameter. The relation between the ratio and the Mach number is as follows:

$$\left(\frac{d_{tube}}{d_{crit}}\right)^2 = \frac{1}{M_1} \left(\frac{2}{\gamma + 1} \left(1 + \frac{\gamma - 1}{2} M_1^2\right)\right)^{\frac{\gamma+1}{2(\gamma-1)}} \tag{3.7}$$

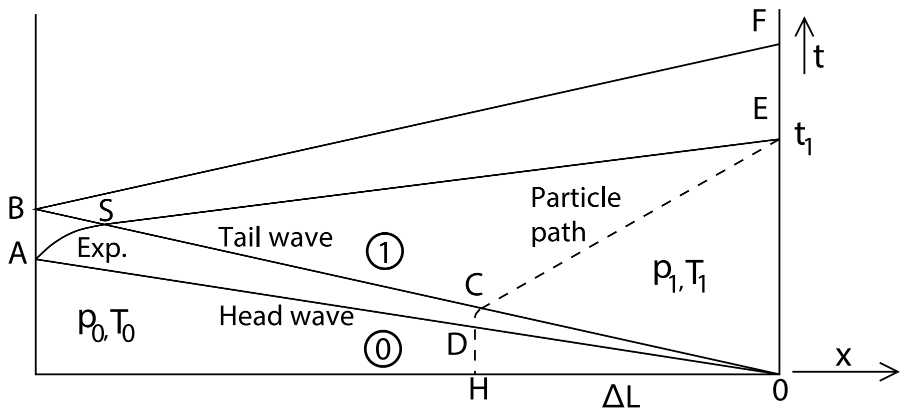

Figure 3.2: $t, x-$diagram of the storage tube [13].

3.1.2. Operation Envelope HTFD

In the previous section the general working principle of a Ludwieg tube was given. In this section, this is translated to the operational envelope of the HTFD. Equation 3.7 shows that the Mach number (M_1) and therefore the run time and total quantities depend on the ratio between the tube diameter (d_{tube}) and the critical throat diameter (d_{crit}). This ratio also determines what Mach number is reached in the test section (because of d_{crit}), provided that the pressure ratio is large enough.

As the test section in the HTFD is fixed, it is only possible to vary the Mach number by changing the throat diameter. The throat diameter in the HTFD is varied by inserting different nozzles. Unfortunately, for Mach numbers lower than 9, the throat diameter is limited by the size of the piston and cannot be increased. In order to reduce the Mach number below 9, a so called tandem nozzle is used. This will be explained further in Section 3.1.3. The properties over the expansion wave for different free stream Mach numbers are shown Table 3.1.

Table 3.1: HTFD expansion wave properties for different nozzles [13].

M	M_1	T_{t_1}/T_{t_0}	p_{t_1}/p_{t_0}	$t_1 a_0/L$
6-9	0.09	0.97	0.89	1.94
10	0.05	0.98	0.93	1.96
11	0.03	0.99	0.95	1.97

Because the temperature of air in the test section drops very fast, it may happen that the air starts to condensate. To prevent this from happening, the storage tube is heated. To reduce the energy consumption only the part of the storage tube that contains the air that is used during a run is heated to a temperature of around 773 K. This is between point H and 0 in Figure 3.2. From the total length of 29 m, only the first 6 m of the storage tube is heated to 773 K.

The temperature difference between the hot tube and the cold tube results in a contact discontinuity on which the expansion wave can reflect, reducing the effective run time of the wind tunnel. This effect is severely reduced by keeping the mass flow constant on the junction between the hot and cold tube. Using this, the following relation between the tube diameter and temperature can be derived [14]:

$$\frac{d_{hot}}{d_{cold}} = \left(\frac{T_{cold}}{T_{hot}}\right)^{\frac{1}{4}} \tag{3.8}$$

This means, that for the HTFD the remainder of the storage tube has to be heated to 375 K. In Figure 3.3 the static pressure upstream of the piston as function of time is given for the $M = 7$ configuration. Before opening the valve, the flow is at standstill and the total pressure equals 99.8 bar. When the valve is opened, the pressure rapidly drops to around 83 bar due to the expansion wave. The small oscillation at $t = 130$ ms is due to a small reflection of the expansion wave on the contact discontinuity between the hot and cold tube. The last thing that is observed, is that the pressure is slightly increasing after the expansion wave hits the discontinuity. The reason for this, is that cold air from the cold part of the storage tube is heated under constant volume in the hot part, effectively increasing the pressure.

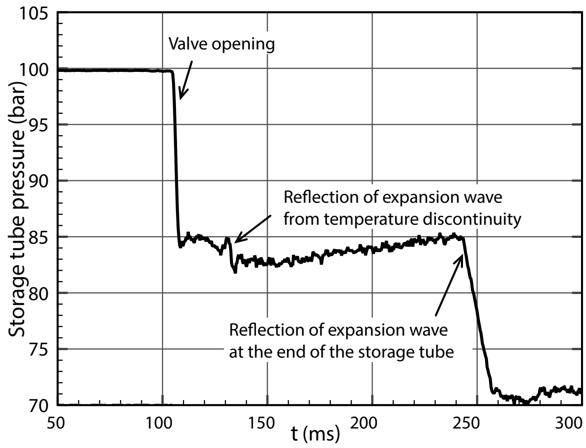

Figure 3.3: Static storage tube pressure for the $M = 7$ configuration [13].

3.1.3. Tandem Nozzle

As stated above, the free stream Mach number is changed by changing the throat diameter of the nozzle. However, for Mach numbers lower than 9 the throat diameter has to become larger than the piston diameter resulting in non-sonic conditions in the throat.

In order to reduce the Mach number below 9, a tandem nozzle is used as shown in Figure 3.4. First the $M = 9$ nozzle is used to accelerate the flow to supersonic conditions, then a normal shock wave slows down the flow to subsonic conditions. Over the normal shock wave, a total pressure drop occurs making it possible to increase the throat diameter of the second nozzle. The total pressure loss as function of the nozzle diameters is calculated using normal shock wave theory in the following equation [13]:

$$\frac{p_{t_2}}{p_{t_1}} = \left(\frac{d_{crit_1}}{d_{crit_2}}\right)^2 \tag{3.9}$$

In Table 3.2 the throat diameters for the different nozzles are stated. For the results presented in this thesis the $M = 7$ nozzle is used, which has a diameter of 34.3 mm. Plugging in the diameters in Equation 3.9 gives a total pressure loss of 32% for the tandem nozzle configuration.

In [13] the pressure in the settling chamber is measured for this particular tunnel. There it is found, that the total pressure loss is slightly less than the theoretical value found with Equation 3.9. A possible reason for this, is that the flow is not slowed down with one shock wave, but with multiple shock waves, which is more efficient.

Table 3.2: HTFD throat diameters for different nozzles [13].

M	6	7	8	9	10	11
d_{crit} (mm)	48.0	34.3	25.38	19.35	15.12	12.06

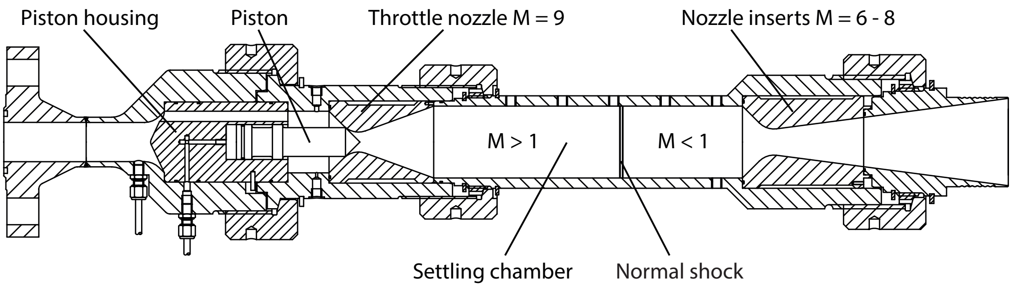

Figure 3.4: Schematic diagram of the tandem nozzle in the HTFD [13].

3.1.4. Free Stream Conditions

There are a couple of things that influence the free stream conditions in the test section. One of them is, that the flow keeps on diverging due to the outflow of the nozzle. As a result, the Mach number keeps on increasing throughout the test section. This effect is partly counteracted by the increasing wall boundary-layer in the test section. The boundary-layer reduces the effective cross-section and therefore the diverging behavior. A combination of these effects results in $M_\infty \approx 7.5$ for the $M = 7$ nozzle. The quantities of the remaining nozzles are given in Table 3.3.

The other effect originates from the discontinuity between the nozzle and the test section. Due to the slight change in angle at that location, Mach waves with the following Mach angle start forming:

$$\mu = \arcsin\frac{1}{M_\infty} = \arcsin\frac{1}{7} = 8.3° \tag{3.10}$$

As the Mach waves travel into the test section they shrink the usable test area. This gives a usable test area of around $200x200$ mm^2 around the center line of the test section.

Table 3.3: HTFD free-stream conditions for different nozzles [13].

Nozzle	M_∞	p_t (bar)	T_t (K)	$Re/L \cdot 10^6$ (m^{-1})
$M = 6$	6.4	2.8	579	1.61
	6.5	14.3	579	7.90
$M = 7$	7.4	5.4	579	2.22
	7.5	28.0	579	11.05
$M = 8$	8.4	10.0	579	3.07
	8.5	51.2	579	15.08
$M = 9$	9.4	20	585	4.65
	9.5	88	585	19.70
$M = 10$	10.3	20	585	3.76
	10.5	88	585	15.85

3.2. Test Model

The test model is used to create the desired flow topology in the HTFD. The goal of the model is to simulate the separation and reattachment of the flow and the instabilities in the shear-layer. The model consists of two separate parts: a flat plate and the compression ramps. There are several requirements made, which the model has to fulfill:

REQ-MODEL-01 The model should be able to operate at varying local Reynolds numbers;

REQ-MODEL-02 The model should be able to operate at different pressure jumps;

REQ-MODEL-03 The model should not be influenced by external disturbances;

REQ-MODEL-04 The model should fit in the HTFD test section;

REQ-MODEL-05 The model should not prevent the HTFD from starting;

REQ-MODEL-06 The model should have a low thermal product ($\rho c k$);

REQ-MODEL-07 The model should have a high emissivity (ε);

REQ-MODEL-08 The model should be optically visible through the HTFD windows.

3.2.1. Flat Plate

The basis of the set-up is the same large flat plate in the middle of the test section used in [15]. Several changes are made to the plate, in order to make it suitable for experiments with large compression ramps.

The flat plate is shown in Figure 3.5. As seen in the figure, the plate consists of three parts: the leading edge (shown in beige), an aluminum frame (shown in grey) and in the middle a Makrolon plate (shown in blue). The leading edge is separable in the case of damage or blunt leading edge experiments need to be performed. For the experiments performed in this report, a sharp leading edge of 50 μm is used to prevent the occurrence of blunt leading edge instabilities. The overall dimensions of the plate are 800 mm × 350 mm ($L \times B$).

During the experiments of [15] there was an attachment point for micro ramps. For these experiments the Makrolon plate is changed to a fully flat plate to prevent radiation changes in the Quantitative InfraRed Thermography (QIRT) runs. To have a high contrast between the infrared radiation from the ambient air and the radiation from the plate, a high emissivity is required. Furthermore, REQ-MODEL-06 states that a low thermal product is required. The reason for this, is that with a low thermal product a larger resolution in the temperature signal is obtained. It is found that Makrolon has these favorable thermal properties, therefore the middle part of the flat plate is made of Makrolon. In Table 3.4 the Makrolon properties of importance for the QIRT are summarized.

Table 3.4: Makrolon material properties.

Material	ρ (kg/m^3)	c $(J/(kg \cdot K))$	k $(W/(m \cdot K))$	ε $(-)$
Makrolon	$1.2 \cdot 10^3$	$1.17 \cdot 10^3$	0.2	0.88

In Figure 3.5, also the Mach waves traveling from the sides of the leading edge towards the middle of the test section are shown (in orange). The angle μ is calculated using Equation 3.10 and is found to be 8.3° for a Mach number of 7.0, this Mach number is chosen because the leading edge of the plate is at the start of the test section. To fulfill requirement REQ-MODEL-03, it is important that the ramp is not placed outside the orange lines.

Finally, requirement REQ-MODEL-01 states that the local Reynolds number should be variable. This is partly achieved by varying the total pressure in the hot tube, but in order to fine-tune the local Reynolds number it is beneficial to vary the location of the ramp. Therefore screw holes are added on the sides of the flat plate. In Section 3.2.2, the location of the holes and how they influence the design of the model are elaborated upon.

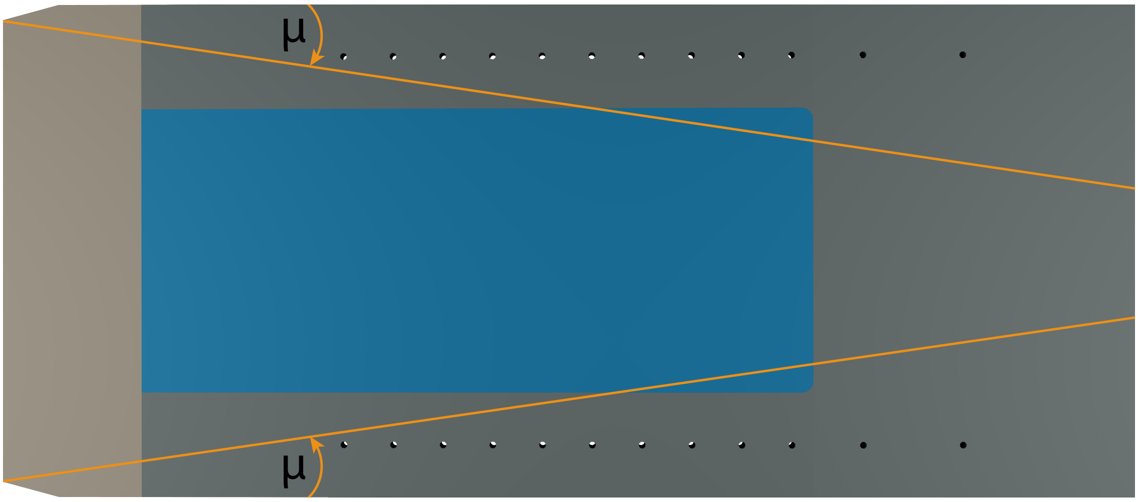

Figure 3.5: Top view of the adapted flat plate.

The reason for choosing a large flat plate with a compression on top instead of only a ramp, is the boundary-layer thickness (δ). As explained in Section 2.2, the boundary-layer thickness grows when going further from the leading edge. This means that with the configuration of the flat plate plus a ramp a very thick boundary-layer is present. In Section 2.5 it is shown that the absolute size of the separation bubble is greatly influenced by the boundary-layer thickness. On top of the large separation bubble, strong and long shear-layers are expected. In these shear-layers the instabilities have a lot of time to grow and are therefore more visible and stronger. This makes it possible to see the effect of transitional shear-layers on the heat fluxes better.

During the experiments, the ramps are placed on a distance from the leading edge of $x_{LE} = 417\ mm$. The experiments are performed in a total pressure range of the hot tube of $p_t = 30 - 95\ bar$. In combination with the leading edge distance of 417 mm, this gives the leading edge Reynolds numbers as stated in Table 3.5.

Table 3.5: Leading edge Reynolds numbers.

$p_t\ (bar)$	30	40	50	60	70	80	90	95
$Re_L \cdot 10^6$	1.67	2.23	2.79	3.35	3.91	4.46	5.02	5.30

3.2.2. Compression Ramps

The compression ramps are used to create the shock wave boundary-layer interaction. The strength of the interaction is determined by the pressure jump imposed on the boundary-layer. The pressure jump is varied by varying the compression ramp angle. To reduce the complexity of the model, five discrete ramps were made instead of a continuous model. The angles of the ramp are 10, 15, 20, 25 and 30° based on the data in [12].

From [16] it is known that the HTFD has trouble with starting because the large frontal area of the model is blocking the test section too much. Therefore the frontal area of the model in [16] is taken as a maximum for the model. The frontal area of that model is equal to 130 cm^2.

As a large part of the frontal area is already consumed by the flat plate (70 cm^2), it is not possible to use a compression ramp over the full width of the flat plate. This is also not necessary as a large part of the flat plate is excluded due to the Mach waves initiated at the leading edge. Another consideration for the width of the ramp, is the presence of 3D effects when the width becomes too small. Therefore an optimum has to be found between a large width to avoid 3D effects and a frontal area which cannot be too large. From [14] it was found that at a width of 115 mm the flow is nearly uniform in spanwise direction. Therefore a width which is slightly increased is opted, this gives a width of 120 mm for the compression ramps.

Looking at the frontal area, this means that the 20, 25 and 30° ramps will be too high. Therefore, these ramps are clipped to a height matching with a frontal area of 50 cm^2. The correlations of Section 2.5 were used to determine whether the shear-layer would still reattach on the ramp, which was still the case. This results in the ramp of Figure 3.6. All the ramps are made out of Makrolon just as the middle part of the flat plate.

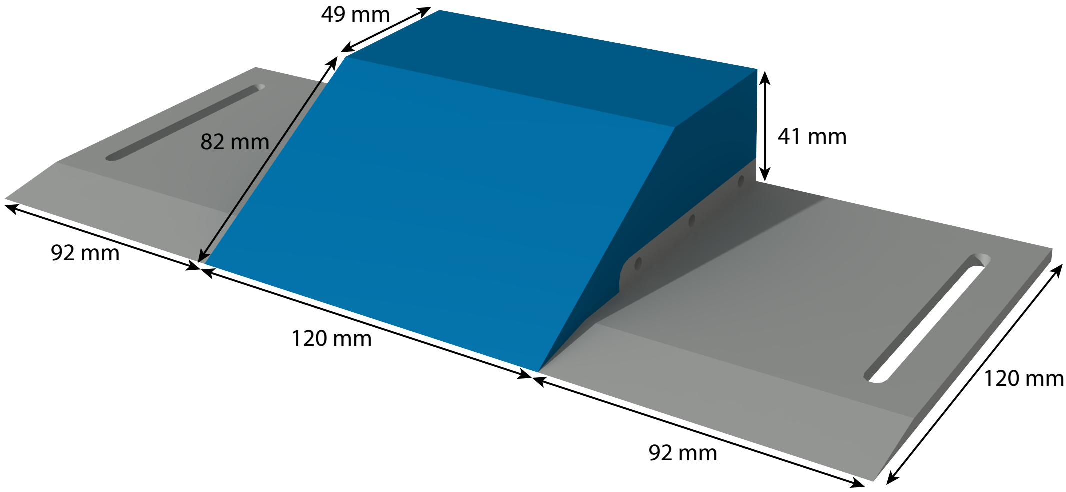

Figure 3.6: Isometric view of the 30° compression ramp.

Because the ramps could not extent over the full width of the flat plate, clamps had to be made to fix the ramps on the flat plate. As shown in Figure 3.6, the clamps are fixed to the ramp with three screws, to prevent the ramp from torquing up, a pin is placed between the leading edges of the clamp and ramp. The slit in the clamps are made such that it can exactly be fastened on the flat plate with three screws. As a result it can be moved between every hole. Furthermore, one screw is always at the beginning of the slit ensuring that the leading edge is always perpendicular with the flow. Because the clamps have to transfer the loads from the ramp to the holes without translation they have to be very stiff. Therefore they are made out of stiffned stainless steel.

Furthermore, the clamp insert in the ramp is too large for the 10 and 15° ramps. To solve this issue a second set of clamps with a smaller insert and only two holes is made, as shown in Figure 3.7. Also the head of the screws near the leading edge are too high, making them visible in the Schlieren images, therefore countersunk screws are used.

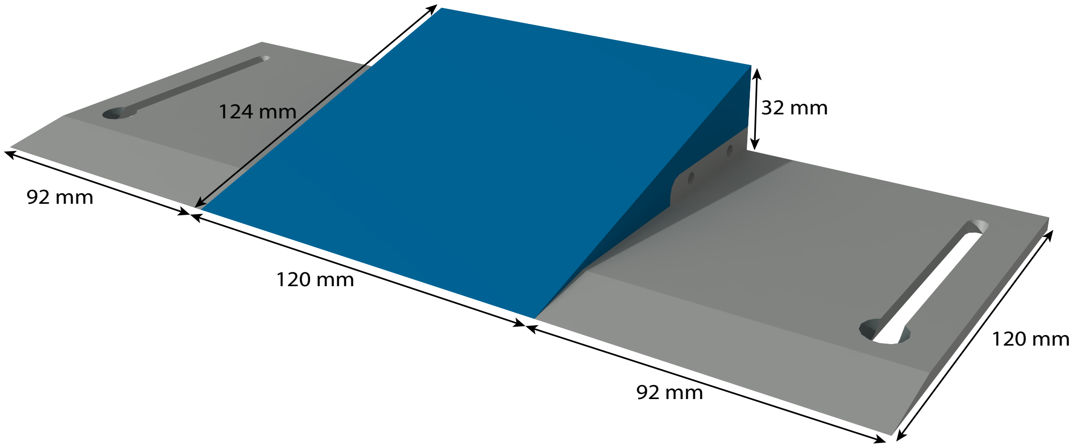

Figure 3.7: Isometric view of the 15° compression ramp.

The complete model in the test section of the HTFD is shown in Figure 3.8. The ramp is placed on the same location as it is placed during the experiments. The images for the other ramps can be found in Appendix A

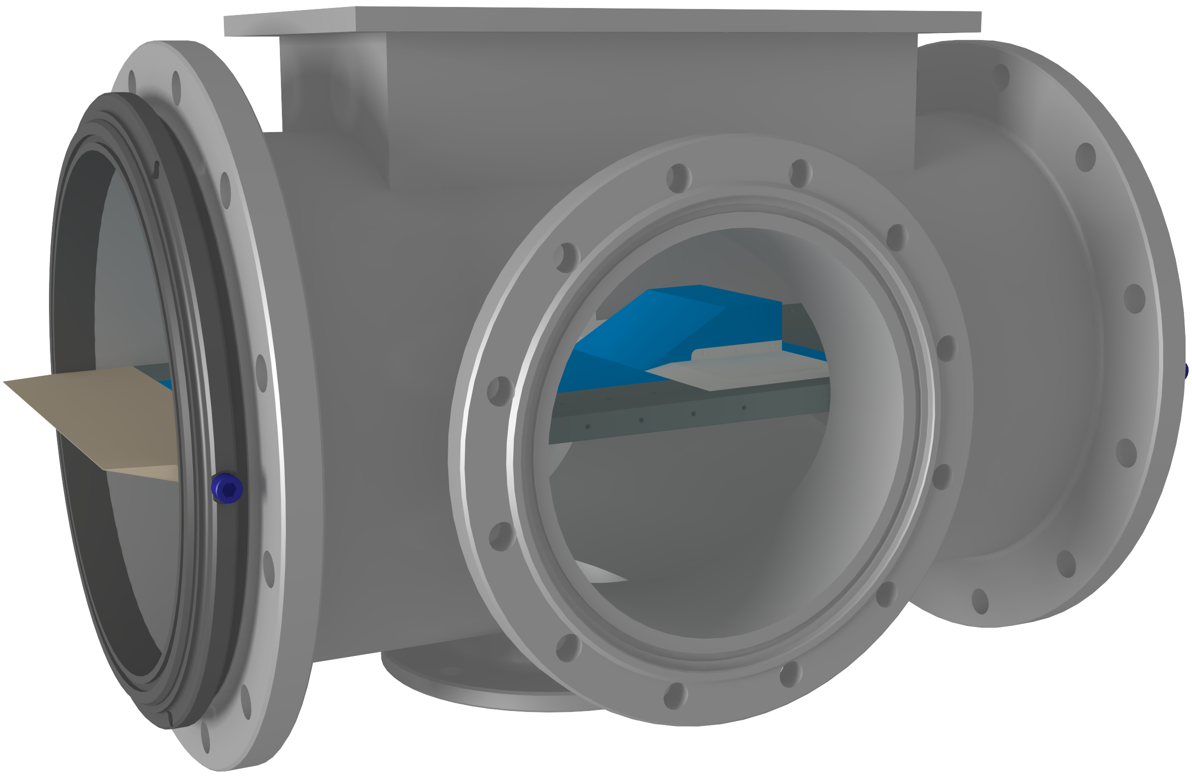

Figure 3.8: The 30° ramp placed in the test section.

3.2.3. Coordinate System

For the remainder of the report, a consistent coordinate system has to be created. It is chosen to have the origin of the x-axis at the leading edge of the ramp. This means, that everything before the ramp has a negative x-coordinate and everything on the ramp, a positive x-coordinate. Furthermore, the x-axis touches the flat plate at the leading edge of the ramp and is pointing to the left with an angle of 0°. As a result, the x-axis does not lie on the top surface of the flat plate but above it due to the 1° angle of the flat plate. The origin of the y-axis is placed in the middle of the ramp. Looking towards the front of the ramp, the y-axis is positive towards the right. At last, the z-axis is positive upwards and is perpendicular to the x- and y-axis. Figure 3.9 gives an overview of the coordinate system.

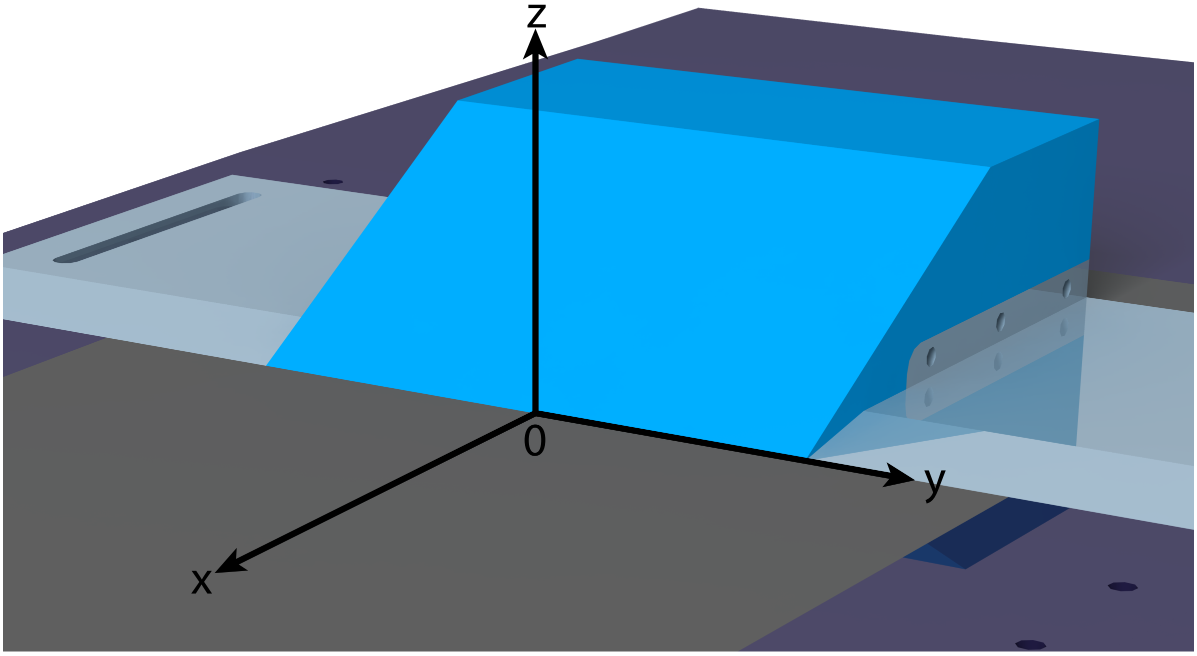

Figure 3.9: Visualization of the coordinate system on the ramp.

4
Flow Measurement Techniques

This chapter describes the flow measurement techniques used during the experiments. The background theory, the required equipment and the processing of the data is discussed. First, this is done for Schlieren imaging in Section 4.1. Then Background Orientated Schlieren (BOS) is discussed in Section 4.2. At last, Quantative Infrared Thermography (QIRT) is treated in Section 4.3.

4.1. Schlieren Imaging

Schlieren imaging is used to obtain a qualitative description of the compression ramp flow. From this, several quantitative values are extracted. This consists of shock wave angles, shear layer angles and shear layer lengths. Furthermore, the growth rate of the waves in the shear layer is determined.

The section, covering Schlieren imaging consists of four parts. First the physical principles of Schlieren imaging are discussed in Section 4.1.1. After that, the application of these principles to Schlieren imaging is explained in Section 4.1.2. Then the measurement set-up is treated in Section 4.1.3. At last the procedures of getting the desired quantitative data is discussed in Section 4.1.4.

4.1.1. Light Refraction Theory

It is known that the speed of light depends on through which medium it is traveling. The ratio between the local speed of light (C) and the vacuum speed of light (C_0) is called the refractive index and is given by the following equation:

$$n = \frac{C_0}{C} = 1 + K\rho \tag{4.1}$$

This equation is dependent on K, which is the Gladstone-Dale constant, and the density (ρ) of the medium. The Gladstone-Dale constant varies with the composition of the medium and the wavelength of the light. The latter can be observed in a rainbow for example. For air, $K_{air} = 2.24 - 2.33 \cdot 10^{-4}$ in the range from infrared to ultraviolet light. The result of a change in refractive index is given by Snell's law in the following equation:

$$n_1 \sin(\alpha_1) = n_2 \sin(\alpha_2) \tag{4.2}$$

Snell's law indicates that light rays are deflected when they travel to a medium with a different refraction index. In Figure 4.1, this is given in a schematic representation for the case that $n_2 > n_1$. It can then be concluded that light rays are deflected towards the direction of the increasing refractive index. As the refractive index increases for an increase in density, the light rays are deflected over a shock wave.

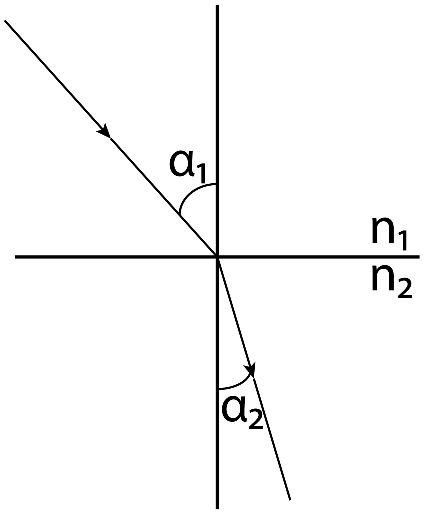

Figure 4.1: Deflection of light rays.

4.1.2. Schlieren Method

In the previous section, it is explained that a shock wave deflects light rays towards the higher density medium. Schlieren imaging is based on this deflection of light. This is visualized in Figure 4.2. In the focal point of the lens a Schlieren knife is placed, which shields a part of the incoming rays. When the light ray hits the shock wave it is deflected as explained by Snell's law. As a result, it is shielded by the Schlieren knife and will be shown as a dark line on the image.

Also the opposite is true, when the density gets lower the rays are deflected away from the Schlieren knife. Locally this increases the light intensity and brighter lines are observed.

How much the rays are deflected, depends on the change in refractive index. When this change is larger, larger deflections are created and the effect is larger. Therefore, Schlieren imaging visualizes ∇n. As a result also $\nabla \rho$ is observed by Schlieren imaging. Because the density gradients are very large over shock waves, they are clearly visible in Schlieren images.

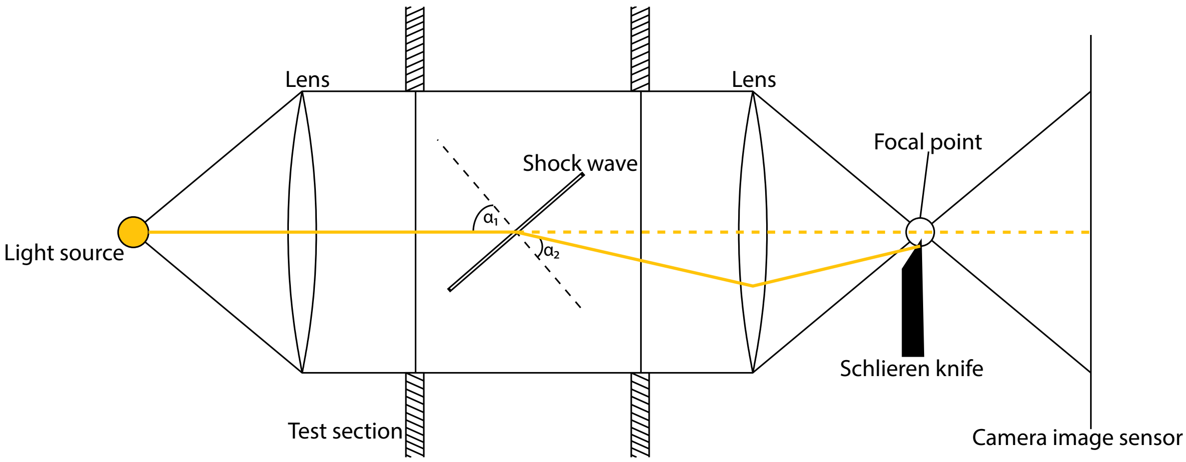

Figure 4.2: Working principle of Schlieren imaging.

4.1.3. Schlieren Measurement System

The Schlieren measurement system consists of a high speed camera, mirrors, lenses, a Schlieren knife, a pinhole and a light source. The set-up as used during the experiments is shown in Figure 4.3. The set-up is a derivative of a conventional Z-set-up, however due to the limited space this was not fully possible. Instead, the parallel beam through the test section is deflected with a mirror before it hits the parabolic mirror.

The camera used is the LaVision Imager pro HS 4M. This camera has a resolution of 2016 × 2016 pixels and can reach a frame rate of 1280 fps at full resolution. When the resolution is cropped, the frame rate can be increased. For the experiments the Schlieren knife is placed horizontally with the shielded side on the bottom. This means, that compressions are shown in black and expansions are shown in white in the images. The parabolic mirrors are used to make a parallel beam through the test section. In the focal point of the parabolic mirror the pin hole is placed. This pinhole determines how much light is shining through the test-section. When more light is available, the Schlieren knife can be closed further. This results in more sensitivity for density fluctuations. However, too much light will result in overexposure of the camera, so an optimum has to be found.

During the experiments two different light sources are used, a normal continuous LED lamp and a spark lamp. The majority of the time a LED lamp is used combined with a exposure time of 1 μs of the camera. To have a closer look at the unsteady features of the flow, the spark lamp is used. This lamp is able to give pulses in the order of nano seconds.

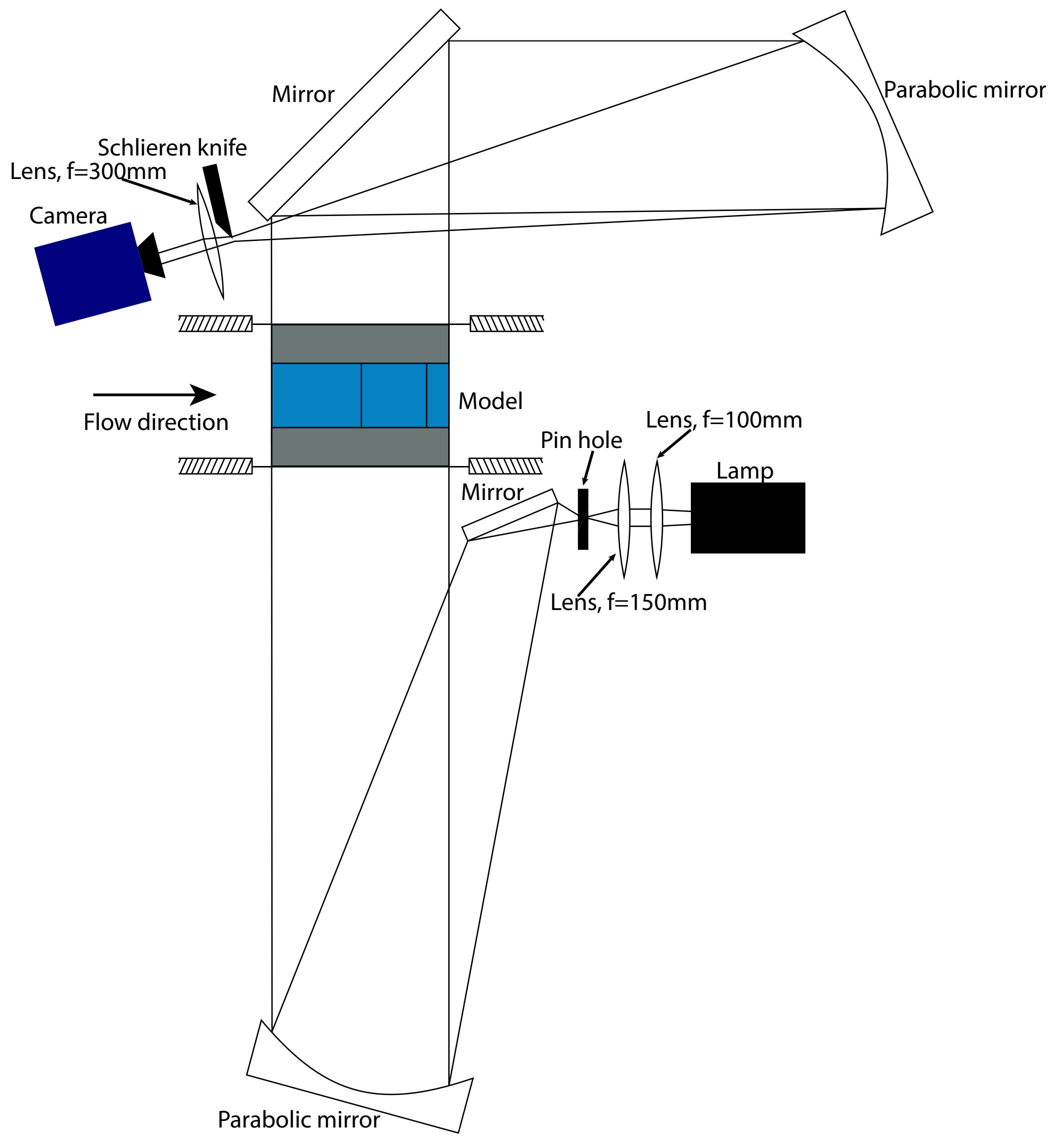

Figure 4.3: Test set-up during the Schlieren measurements.

4.1.4. Image Data Processing

The Schlieren images are further processed to get quantitative data. This consists of two different parts, one part is focused on the overall flow topology and the other part on the instability waves in the shear layer. The flow topology consists of the shear layer angle, the shear layer length and the corresponding shock wave angle. These results are discussed in Section 5.2. From the instability waves, the growth rate is deducted. These results are presented in Section 5.3. The full flow chart of the process is given in Figure 4.4. In the flowchart all the different data processes are summarized

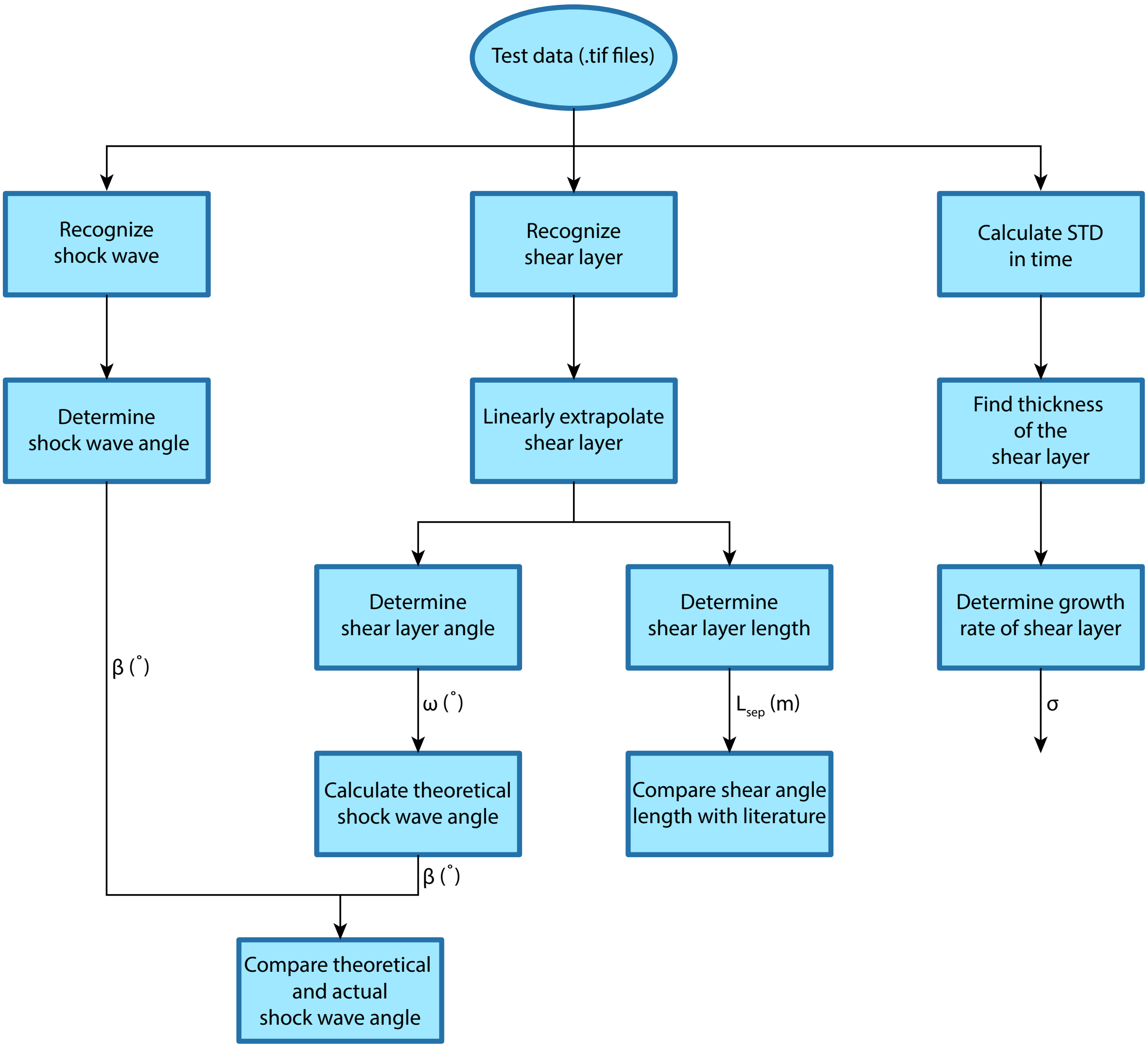

Figure 4.4: Flow diagram of the processing of the Schlieren data.

Starting on the left in Figure 4.4, the recognition of the shock wave is stated. In the data the shock waves are almost straight, therefore the shock wave is recognized by looking for minimum intensities at the edges of the images. Because multiple shock waves are present in the image, it is not always possible to use the minimum intensity, in that case the parameter is tuned per experiment. Because the shock wave is nearly linear, a linear regression line is made based on the shock wave. The slope of the regression line is then converted to the shock wave angle (β) by simple trigonometric functions.

The recognition of the shear layer is done by finding the maximum intensity in every pixel row. This is possible due to the strength of the shear layer, it has by far the highest intensity in the image. Because of the size of the shear layer, the separation point lies outside the image. Therefore, an extrapolation has to be performed to find the shear layer length. As the shear layer is very linear at the beginning, a linear extrapolation is performed for the first 300 pixels in the image. The hardest part is to determine a criteria for the start of the shear layer, or in other words, when does the linear extrapolation stop?

One of the options is to stop the shear layer at the intersection with the flat plate. However, in this case this is not possible, due to the small angle of the shear layer near separation, the angle of the flat plate and the thick boundary-layer. The flat plate is at an angle of 1°, initial runs show that the shear layer is at an angle of approximately 5°. This means that the flat plate and shear layer are closing in on each other with only a rate of 4°. Due to this slow convergence, crossing the additional distance of the thick boundary-layer gives a very large increase in total shear layer size. For example: with a boundary-layer of 2 mm and a shear layer angle of 5°, the shear layer length is increase by 29 mm by taking the intersection at the flat plate compared to the intersection at the boundary-layer edge. If the boundary-thickness is 2.5 mm, the additional shear layer length increases even to 36 mm. This shows the sensitivity of this solution. Therefore this solution is not used in the post-processing.

Another option is to let the shear layer start at the edge of the boundary-layer. But, the thickness of the boundary-layer is not known so it had to be taken from the reference temperature method. This mixing of experimental and theoretical data is unfavorable and therefore not used. Another feature of the start of the shear layer is that it induces the separation shock wave. This means, that the origin of the shock wave and the origin of the shear layer should be very close to each other. Therefore, the shock wave is linearly extrapolated and the intersection of this line and the shear layer extrapolation is taken as the starting point of the shear layer. The slope of the linear extrapolation is converted to the shear layer angle (φ_{SL}) with trigonometric functions. The theoretical shock wave angle is then calculated by using the equations in Section 2.1 and can be compared with the measured shock wave angle.

Near the ramp the shear layer is moving up due to the compression waves. Therefore reattachment is not clearly defined. As end point the shear layer is linearly extrapolated to the ramp. The distance between the intersection with the shock wave and intersection with the ramp is the shear layer length (L_{sep}). This length can then be compared to the correlations given in Section 2.5.

Looking more closely to the shear layer, it is observed that waves are traveling through it. It is interesting for the transition behavior to see what the growth rate (σ) is. The growth rate is determined by taking the standard deviation (STD) of all the pixels in time. This gives a field of STD values that represent the fluctuations. Around the shear layer the STD value is the largest. The STD values around the shear layer are the results of the fluctuations inside the shear layer. If the waves grow bigger, the spread of the STD value around the maximum will increase. For every pixel row, the STD peak is found. The STD value found 50 px next to the peak is subtracted. The first roots next to the peaks are then found. The shear layer width is defined as the distance between the roots. The slope of the linear regression line through the width distribution is the growth rate (σ).

4.2. Background Orientated Schlieren (BOS)

Background Orientated Schlieren (BOS) is a method based on the same physical principle as explained in Section 4.1.1. In section 4.2.1, it is explained how this theory is used to obtain a flow field. Then, the used measurement system is treated in Section 4.2.2. At last, the image processing is discussed in Section 4.2.3.

4.2.1. Theory of BOS

As said, BOS is based on the same physical theory as conventional Schlieren. This theory is based on the fact that the refractive index of a medium depends on the density. As a result, a change in density results in a change in refractive index. Snell's law states that light rays deflect when meeting a change in refractive index. This means that a change in density can be observed by looking at the deflection of light rays.

BOS uses this principle by placing a speckle pattern on the background of the image. A camera is placed in focus on this pattern. If then a density change is present in front of the pattern, the light rays will deflect. On the image this will manifest as a movement of the speckles. This is shown in Figure 4.5. The displacement on the image is given by the following equation [17]:

$$\Delta y = f\left(\frac{Z_D}{Z_D + Z_A - f}\right)\varepsilon_y \tag{4.3}$$

In this equation, f is the focal distance of the lens. The other variables are defined as in Figure 4.5.

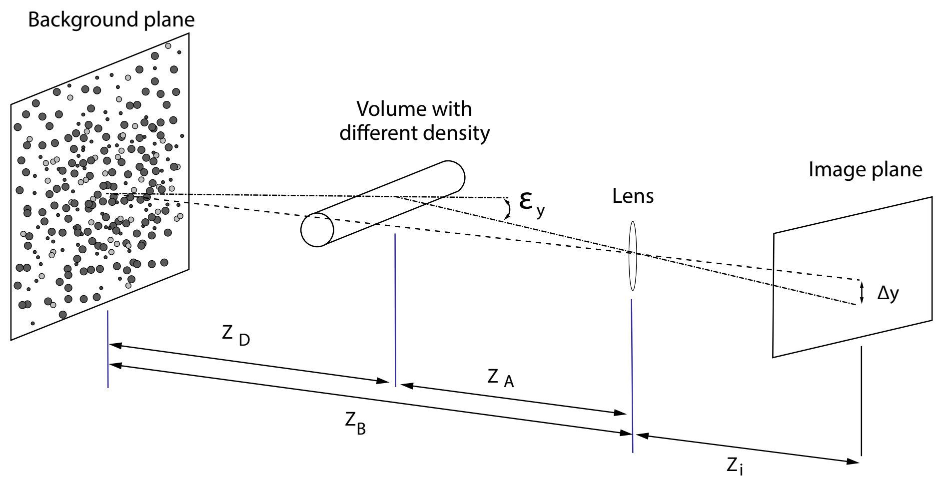

Figure 4.5: Principle of BOS [17].

It is required for BOS to have a relative displacement of the speckles, therefore two camera shots have to be performed. In one shot there are no density changes present so it can act as a reference. The other shot is then the image, with density changes present. These two runs can then be correlated using the same correlation methods used in PIV. This will then create a density change field. Because the same software is used as for PIV, it is desired to have the same speckle size for which the software is optimized. This means that the speckles should have a size of around 3 – 5 pixels in the image.

4.2.2. BOS Measurement System

The measurement system used during the experiments is shown in Figure 4.6. The set-up consist of LED lamps, a speckle pattern and the same camera used during the conventional Schlieren imaging. On the camera lenses with different focal points are placed. The exposure time and which lenses are used, is treated in Section 7.2.

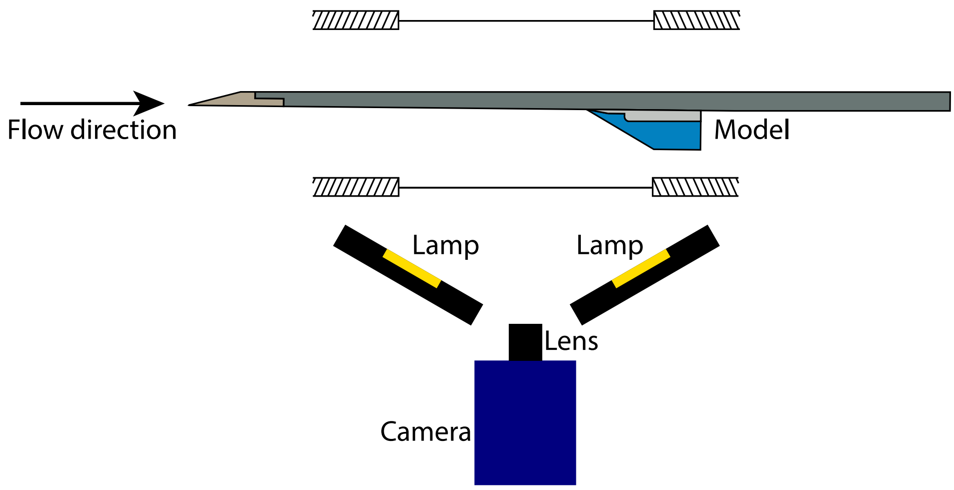

Figure 4.6: Test set-up during the BOS measurements.

For the experiments the model configuration is used, which is expected to give the clearest contrast between the two shots. A high Reynolds number will results in the strongest density changes. Therefore, the test is performed at a high total pressure of 95 bar. From theory it is also known that shear layer gets longer for higher pressure jumps. Therefore the 30° ramp is used during the experiment. The speckle pattern has a speckle size such that it covers around 4 or 5 $pixels$ in the image. However, it is possible that due to the very small speckles, the shape of the speckles is lost. This affects the accuracy of the correlation and therefore also a speckle size of 10 $pixels$ is used during the experiments.

4.2.3. BOS Image Processing

As mentioned above, the images are processed using PIV correlation software. The software used in this case is DaVis 8. Several choices can be made in DaVis for the correlation. These consist of the interrogation window, overlap and passes. Because the density changes are expected to be small, computationally heavy settings are used. These are an interrogation window of 64 × 64 pixels, 75% overlap and 3 passes.

4.3. Quantitative InfraRed Thermography (QIRT)

Quantitative InfraRed Thermography (QIRT) is used to look at the heat fluxes present near the reattachment region. The principle of the method is based on the detection of radiation coming from the surface. This section will start with an explanation of the infrared theory in Section 4.3.1. After that, the measurement system is explained in Section 4.3.2. Then the calibration procedure is treated in Section 4.3.3. This calibration procedure is required to find the heat flux, which is explained next in Section 4.3.4. At last, the processing of the heat flux data to the desired results is explained in Section 4.3.5.

4.3.1. Infrared Theory

A body with a temperature above 0 K radiates electromagnetic waves. The amount of radiation is a function of the surface temperature and wavelength. For a blackbody the spectral exitance, which is the amount of energy transmitted per area per wavelength, can be calculated using the following equation:

$$E_{b_\lambda} = \frac{C_1}{\lambda^5 \left(e^{\frac{C_2}{\lambda T_s}} - 1 \right)} \tag{4.4}$$

This equation is called Planck's law. C_1 and C_2 are called respectively the first- and second radiant constant where: $C_1 = 3.7415 \cdot 10^{-16}\ Wm^2$ and $C_2 = 1.4388 \cdot 10^{-2}\ mK$. Figure 4.7 gives the spectral exitance as a function of wavelength for different temperatures.

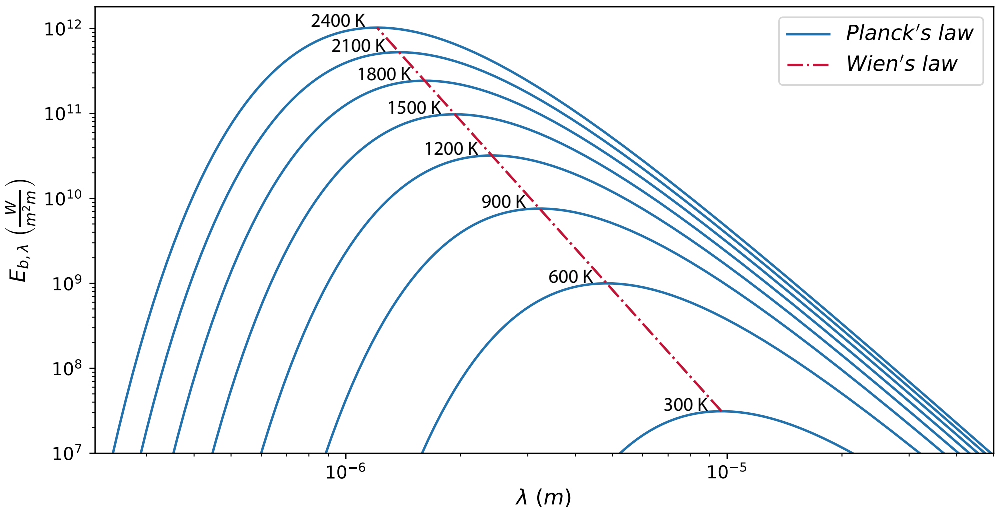

Figure 4.7: Planck's law.

Looking at the graph, it is shown that the maximum spectral exitance for a temperature lies on a line in the logarithmic plane. This line is called Wien's law and is described by the following equation:

$$\lambda_{max} T_s = 2.896 \cdot 10^{-3} \tag{4.5}$$

To find the total radiation per surface area for a given temperature, Planck's law has to be integrated over all wavelengths:

$$E_b = \int_0^\infty E_{b_\lambda}\, d\lambda = \sigma T_s^4 \tag{4.6}$$

This equation is the well known Stefan-Boltzmann law with $\sigma = 5.670 \cdot 10^{-8}\ W/(m^2 \cdot K^4)$ and represents the area underneath each Planck curve. All the equations stated above can only be used for blackbodies, however in reality objects do not act as blackbodies over the whole range of wavelengths and therefore emit less energy. The total real body radiation is then:

$$E_r = \int_0^\infty \varepsilon(\lambda) E_{b_\lambda} d\lambda \tag{4.7}$$

$\varepsilon(\lambda)$ is the emissivity of the body and in some cases it depends on the wavelength as is shown in Figure 4.8. The gray body hypothesis states, that the emissivity is not dependent on the wavelength. This is a valid assumption as the emissivity of most materials is nearly independent of wavelength. As a result the following equation is valid:

$$E_r = \varepsilon \sigma T_s^4 \tag{4.8}$$

In reality, the emissivity has a directional dependence, however for angles less than 50° this is negligible. Another dependency is on the surface temperature. The reason for this, is that the wavelength band changes for a different surface temperature, as seen in Figure 4.7. As a result, also the gray-body emissivity has to change [18].

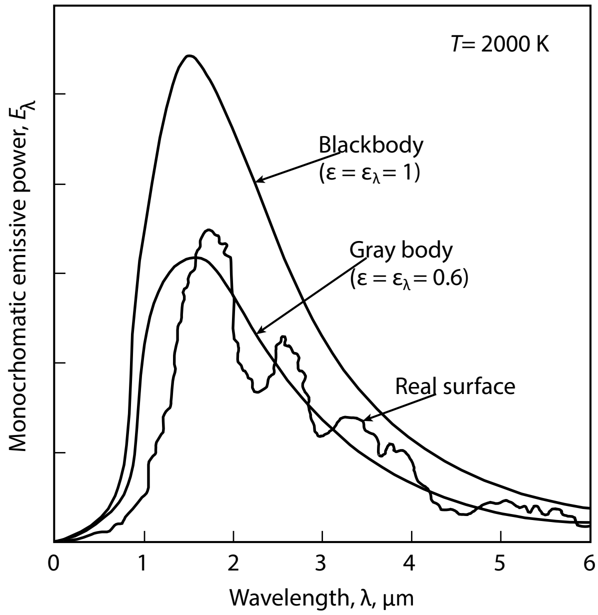

Figure 4.8: Radiation of a black body, gray body and real body [18].

The remainder of the incoming radiation can either be absorbed (α_λ), reflected (ρ_λ) or transmitted (τ_λ). The λ means that the quantities depend on the wavelength. As radiation cannot be destroyed the following has to hold:

$$\alpha_\lambda + \rho_\lambda + \tau_\lambda = 1 \tag{4.9}$$

Kirchoff's law states that in a thermal equilibrium the absorption equals the emissivity for all temperatures and wavelengths ($\varepsilon_\lambda = \alpha_\lambda$). For non-transparent gray bodies the equation above becomes:

$$\varepsilon + \rho = 1 \tag{4.10}$$

The radiated energy by a gray body is then:

$$E_r = \varepsilon \sigma (T_s^4 - T_a^4) \tag{4.11}$$

Where T_a is the ambient temperature. However, during the experiments the infrared camera is not operating in vacuum, this means that also the environmental disturbances have to be taken into account. This means that Equation 4.9 also has to hold for air. For the test it is beneficial that no radiation is lost in the air, so all the radiation is transmitted. Therefore, the air should not absorb or reflect the radiation. It is known that without additional particles, air is non-reflective in the infrared spectrum. However, in Figure 4.9 it is shown that for some parts in the infrared spectrum there is a lot of absorption and therefore less transmissivity present. The absorption is the result of CO_2 and H_2O in the air. Looking at Figure 4.9 there are two possible measurement regions:

- Short Wave Band (SWB): 3 μm − 5 μm,
- Long Wave Band (LWB): 8 μm − 12 μm.

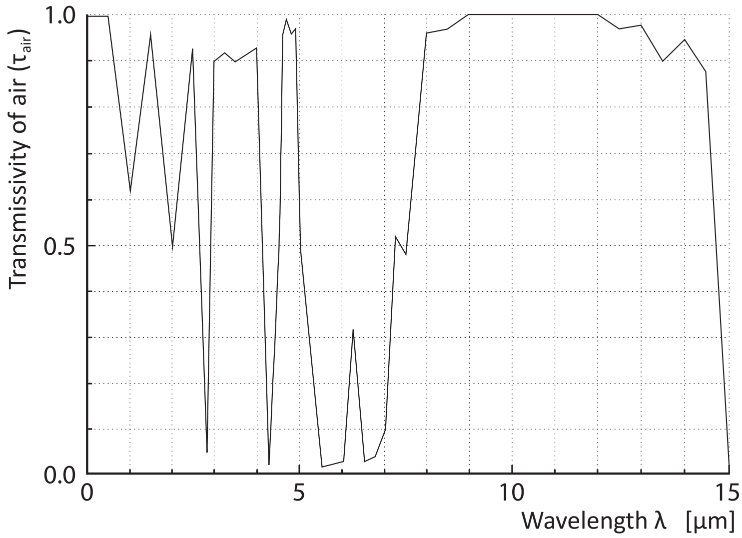

Figure 4.9: Transmissivity of air for different wavelengths (1 atm, 25 °C, 25% relative huminity and 30 m distance) [19].

4.3.2. Infrared Measurement System

The infrared measurement system consists of an infrared camera, a germanium window, the test model discussed in Section 3.2 and a tripod.

The camera used is the CEDIP Titanium 530L which is shown in Figure 4.10. This camera uses a quantum detector. The detector consists of an array of 320 × 256 Mercury Cadmium Telluride (MCT) quantum detectors. The spectral response is 7.7 − 9.3 μm which lies in the LWB band explained above. The camera has a maximum frame rate of 250 Hz using the full resolution. For the experiments the frequency is limited to 200 Hz to prevent an information overflow for the processing computer.

As said, the camera consists of 320 × 256 individual detectors, to get the same response on radiation a Non-Uniformity Correction (NUC) procedure is done. This NUC procedure makes sure that the gain and offset of the detectors are such, that an uniform response is created. The NUC is performed by covering the lens with a black cylinder, with this the gain and offset is calculated for each pixel. For the noisy pixels a Bad Pixel Reduction (BPR) procedure is performed. In this procedure a weighted average of the surrounding pixels replaces the noisy pixel.

The sensitivity of the camera is determined by the exposure time. As a result, the exposure time determines which temperature range can be measured. To determine the required temperature range, an experiment is done with the internal calibration of the camera. From this, a maximum temperature of around 383 K is found near reattachment. As a higher exposure time is beneficial, the upper limit of the temperature range is fixed to 393 K. This results in an exposure time of 144 μs. The full range is then 261 $K \leq T \leq$ 393 K.

Figure 4.10: The Cedip Titanium 530L infrared camera.

Section 4.3.1 explained that a high transmissivity is required for the air inbetween the camera and the model. The same holds for the wind tunnel windows. Unfortunately, normal glass windows are opaque in the infrared spectrum and cannot be used. Therefore, a germanium window is used during the test. Germanium has a transmissivity of approximately $\tau_{GE} \approx 0.8$ [20].

A tripod is used to put the camera at the correct height and at an angle with respect to the wind tunnel. Without this angle the camera would see his own reflection. The angle chosen is 15°. The complete measurement system is shown in Figure 4.11.

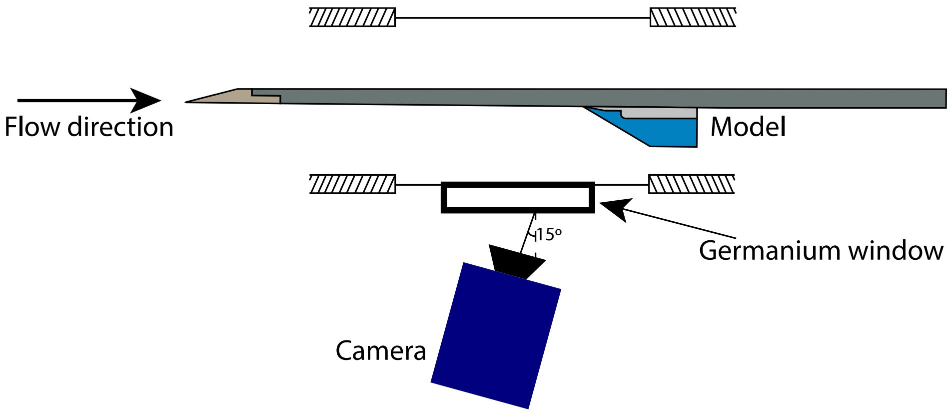

Figure 4.11: Test set-up during the QIRT measurements.

4.3.3. Calibration Procedure

The infrared camera explained in the previous section has digital levels (DL) as output. As the temperature change is required for calculating the heat fluxes, these digital levels have to be converted to temperatures. This is done by calibrating the camera with a blackbody in conditions which are representative of the actual experiments.

As mentioned in Section 4.3.1, a blackbody is a perfect emitter and therefore also a perfect absorber. However, in reality such a body does not exist. To get as close to a blackbody, the geometry in Figure 4.12 is used. The high emissivity is obtained in two ways, first the inside of the cylinder is painted black. This already increases the emissivity to $\varepsilon \approx 0.9$. To increase the emissivity even more, the opening of the cylinder is narrowed and a cone is placed on the back. As a result, the incoming radiation reflects on the cone towards the wall where it is reflected again etc. Because of the narrow opening, the radiation cannot easily escape from the cylinder. Furthermore, because the sides are black, after every reflection a large part of the radiation is absorbed. With this configuration an emissivity of $\varepsilon = 0.999$ is obtained [21].

The temperature is controlled by pumping water through the blackbody. The temperature is monitored by three J-type thermocouples placed at the inlet, the cone and the outlet. The thermocouple at the cone is used for the calibration, as the camera is pointing directly at it. The other thermocouples are used to check if the temperature is stable in the blackbody.

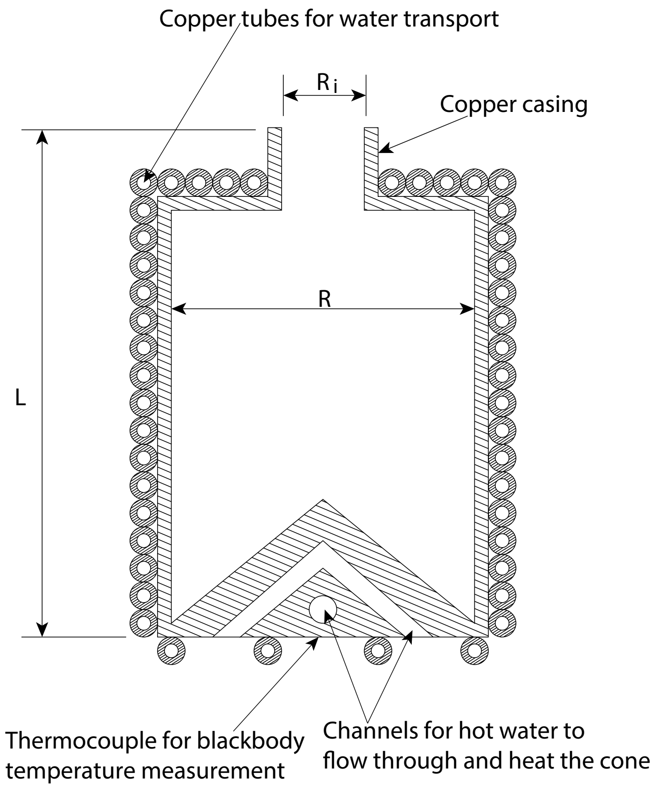

Figure 4.12: Schematic view of the blackbody [19].

In the experiment a germanium window is used because it has a high transmissivity in the infrared spectrum. However, the transmissivity is not equal to one and should therefore be compensated for. This is done by calibrating the camera while it looks through the germanium window. In this way the transmissivity of the windows is incorporated in the calibration curve. The window is placed under the same angle as is done during the experiment. At last, the whole is set-up is covered with a black cloth to avoid that background radiation influences the calibration. The full calibration set-up is shown in Figure 4.13.

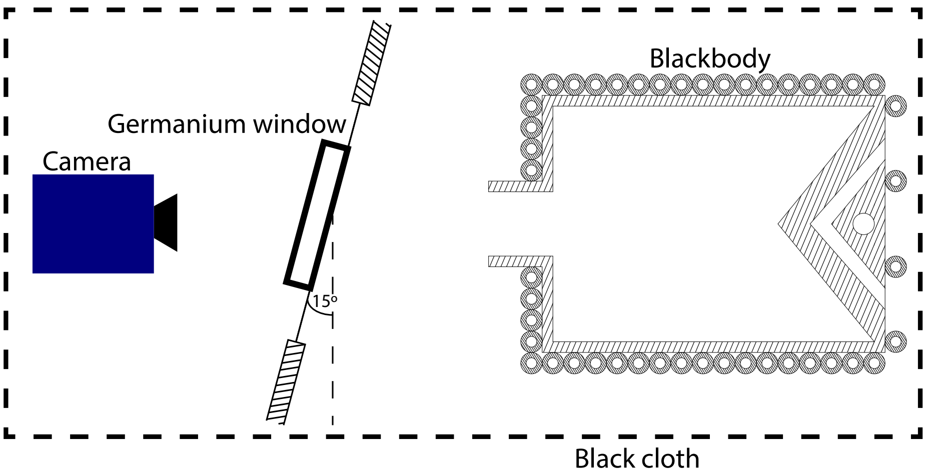

Figure 4.13: Set-up of the calibration procedure.

During the calibration, the temperature is increased from 10°C to 85°C. After every 5°C the cone in the blackbody is recorded with the infrared camera. The camera is configured at the same exposure time (144 μs) and frequency (200 Hz) as used during the experiments. The data is then fitted on the following equation:

$$T = \frac{B}{\ln\left(\frac{R}{I} + F\right)} \tag{4.12}$$

This gives the constants B, F and R as stated in Table 4.1. The result of the curve fit is shown on top of the data points in Figure 4.14.

Table 4.1: Calibration constants.

Constant	B	F	R
Value	$6.58 \cdot 10^2$	3.406	$2.47 \cdot 10^4$

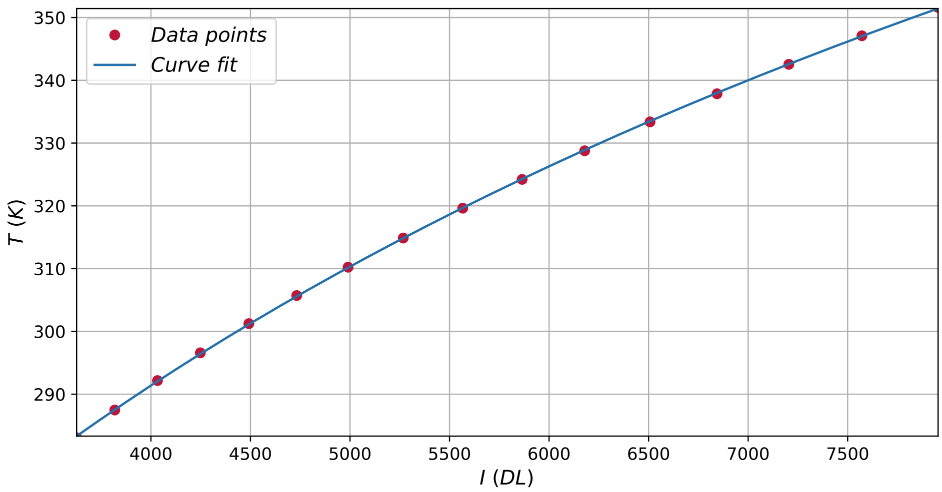

Figure 4.14: Calibration curve for the infrared camera.

The calibration process is summarized in the flowchart stated in Figure 4.15. In the next chapter this flowchart is extended for the heat flux data reduction procedure.

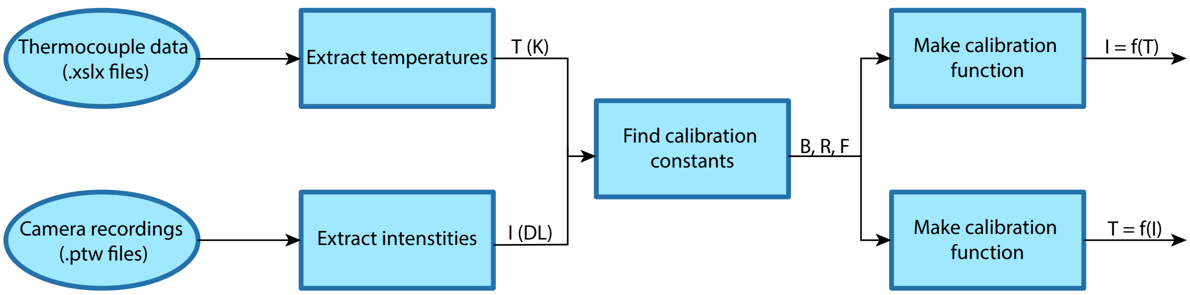

Figure 4.15: Flowchart of the calibration procedure.

4.3.4. Heat Flux Data Reduction Procedure

With the calibration curve ready, it is possible to find the surface temperatures and from that the heat flux can be deducted. But before it is possible to calculate the surface temperature, the measured intensity has to be corrected.

The measured intensity consists of two parts, the emitted radiation by the model (I_r) and the reflected radiation from the ambient air (I_a). The first one is required to calculate the surface temperature. Therefore the measured intensity has to be corrected as is shown by the following equation:

$$I_{meas} = \varepsilon I_r + \rho I_a \tag{4.13}$$

From Equation 4.10 it is known that $\rho = 1 - \varepsilon$. Plugging this in gives the following equation:

$$I_{meas} = \varepsilon I_r + (1 - \varepsilon) I_a \tag{4.14}$$

When the ambient intensity is known, the intensity emitted by the model is known. The intensity from the ambient is calculated as follows:

$$I_a = \frac{R}{e^{\frac{B}{T_a}} - F} \tag{4.15}$$

This is the inverse of Equation 4.12 with the calibration constants of Table 4.1. However, for the temperature the ambient temperature is plugged in. The emitted radiation by the model is then:

$$I_r = \frac{I_{meas} - (1 - \varepsilon) I_a}{\varepsilon} \tag{4.16}$$

This intensity is filled in Equation 4.12 to find the surface temperature of the model. This results in the following equation:

$$T_s = \frac{B}{\ln\left(\frac{R}{I_r} + F\right)} \tag{4.17}$$

From the surface temperature in time, the heat flux can be computed. This is done by using the theory of heat conduction in a semi-infinite one dimension wall. The model is treated as a thin-film sensor with only the Makrolon ramp as medium. This is possible, because the Makrolon already has favorable properties as is explained in Section 3.2. The heat flux is then calculated by solving the one dimensional heat equation. This results in the following equation for the heat flux:

$$q_s(t) = \sqrt{\frac{\rho c k}{\pi}} \int_0^t \frac{\frac{dT_s(\tau)}{d\tau}}{\sqrt{t - \tau}} d\tau \tag{4.18}$$

As all the variables are known in this equation, it is theoretically possible to directly numerically integrate the equation and find the heat flux in time. However, the equation requires the derivative in time of the surface temperature signal. Differentiating a measured signal significantly increases the noise and is therefore not desired. This is circumvented by looking at the cumulative heat input first:

$$Q(t) = \sqrt{\frac{\rho c k}{\pi}} \int_0^t \frac{T_s(\tau)}{\sqrt{t - \tau}} d\tau \tag{4.19}$$

This equation is numerically integrated in the following way [22]:

$$Q(t_n) = \sqrt{\frac{\rho c k}{\pi}} \sum_{i-1}^{n} \frac{\phi(t_{i-1}) + \phi(t_i)}{\sqrt{t_n - t_{i-1}} + \sqrt{t_n - t_i}} \tag{4.20}$$

In this equation $\phi(t) = T_s(t) - T_s(0)$, which is the temperature rise compared to the start of the run. The heat flux is then found by using a finite difference scheme on the previous equation:

$$q_s(t_n) = \frac{dQ(t_n)}{dt_n} = \frac{-2Q(t_{n-8}) - Q(t_{n-4}) + Q(t_{n+4}) + 2Q(t_{n+8})}{40(t_n - t_{n-1})} \tag{4.21}$$

For comparison it is convenient to non-dimensionalize the heat flux. In Section 2.2.1 the Stanton number (St) is introduced for a flat plate. The general definition is as follows:

$$St = \frac{q_s}{\rho_e u_e (h_t - h_{aw})} \tag{4.22}$$

In practical applications it is very hard to determine the adiabatic wall enthalpy. Therefore, an alternative definition of the Stanton number (c_h) is used in this report. Instead of using the adiabatic wall enthalpy, the total enthalpy is used. By using $h = c_p T$ the following equation is found for the alternative Stanton number:

$$c_h = \frac{q_s}{c_p \rho_1 u_1 (T_t - T_w)} \tag{4.23}$$

The wall temperature in this case is taken locally instead of using a global average of the wall temperature. The total data reduction procedure is then summarized in the flowchart in Figure 4.16.

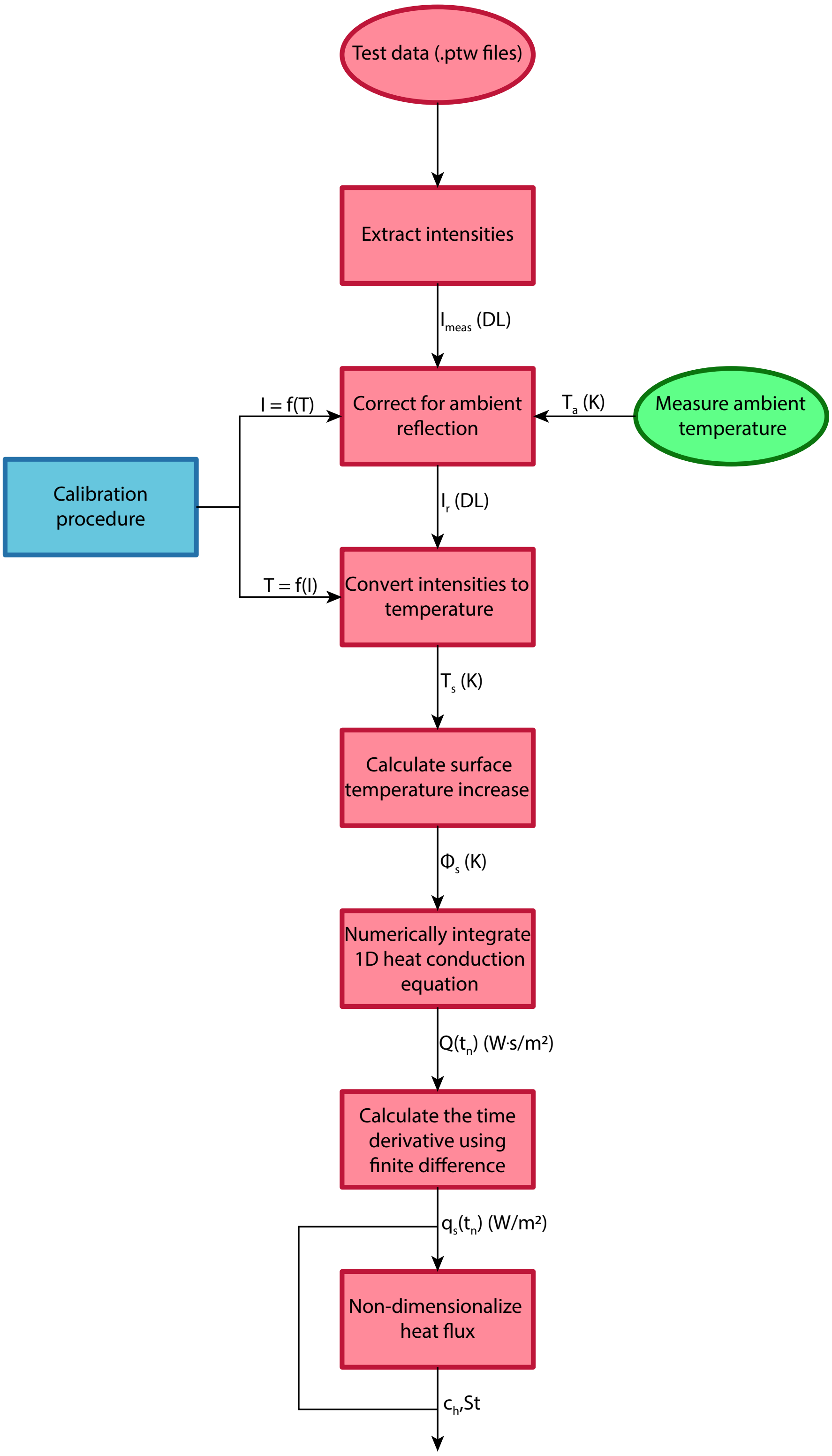

Figure 4.16: Flowchart of the total data reduction procedure.

The data reduction procedure is validated by doing a flat plate run in the HTFD. This data is converted to heat fluxes with the method stated above. This result is compared to the result found with the reference temperature method in Section 2.2.1. In Figure 4.17 the result is shown. The total pressure is varied to vary the Reynolds number. Good agreement between the reference temperature method and the data reduction method explained above is found. In this case x is the distance from the flat plate leading edge instead of the coordinate system explained in Section 3.2.3.

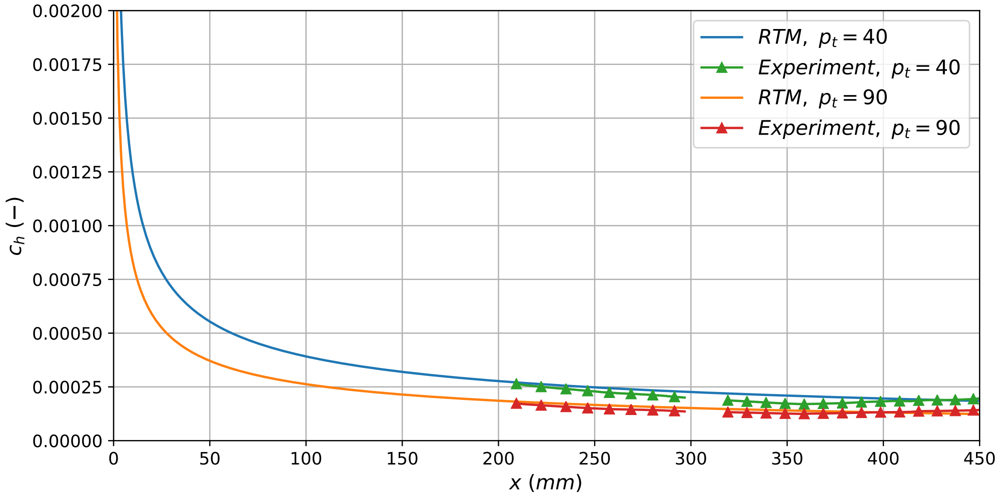

Figure 4.17: Comparison between the reference temperature method and a flat plate experiment for different total pressures.

4.3.5. Processing Heat Flux Data

Now, the heat flux data is processed further to get the desired results from it. These are the location and magnitude of the peak loads near reattachment. These results are presented in Section 6.2. The second part is looking at the wavelength of the spanwise variation of the peak heat flux. These results are presented in Section 6.3.

The first thing that is required, is the position of the ramp in the images. The data consists of 320×256 heat flux points. These points have to be related to physical coordinates. Because the camera is at an angle, it is not possible to simply scale the pixels to a distance. In order to solve this, three calibration plates are build for the two types of ramps and flat plate. The plates are shown in Figure 4.18.

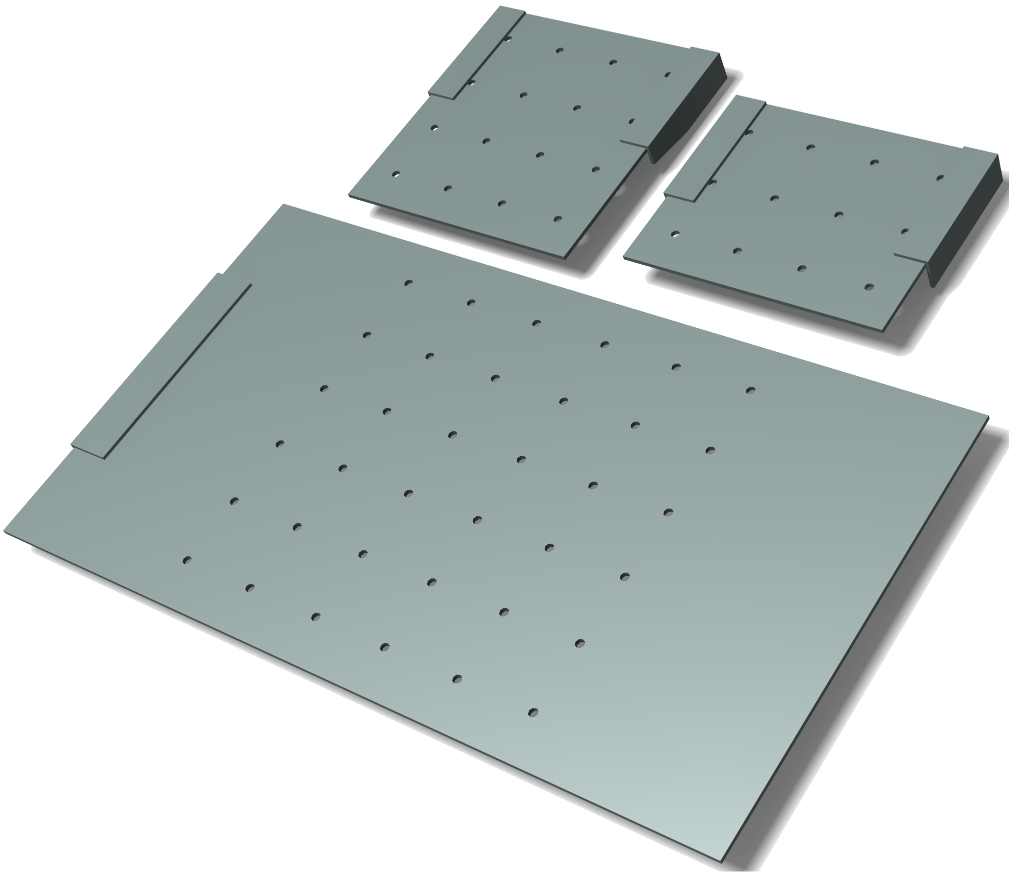

Figure 4.18: The different calibration plates.

The calibration plates are placed on the top of the model and are made of aluminum as shown in Figure 4.19. Due to the difference in emissivity of Makrolon and aluminum, the calibration plate is clearly visible with the infrared camera. To create additional calibration points, holes are made in the plates. The image shown in Figure 4.20 is then found when recording the calibration plates with the infrared camera. In this figure the holes in the plates can be seen clearly

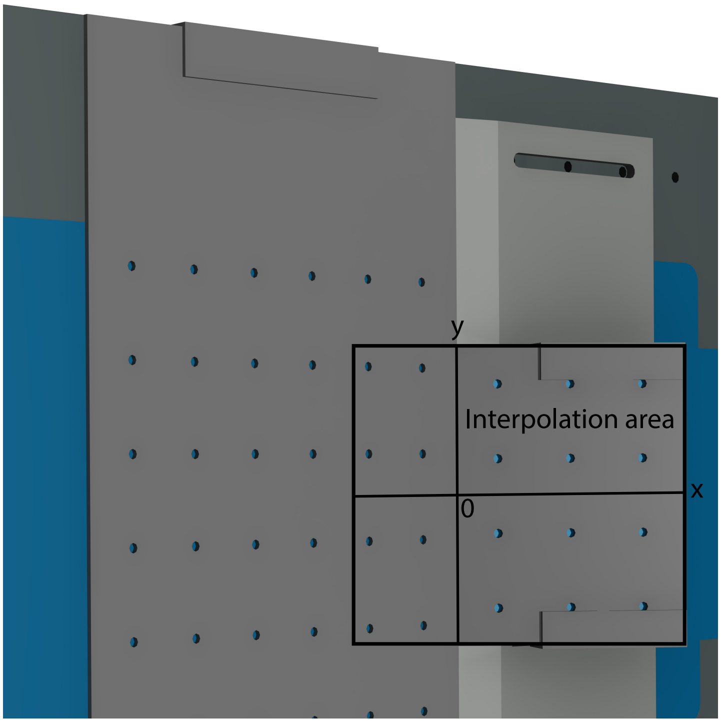

Figure 4.19: Reference coordinate axis for the interpolation with interpolation region.

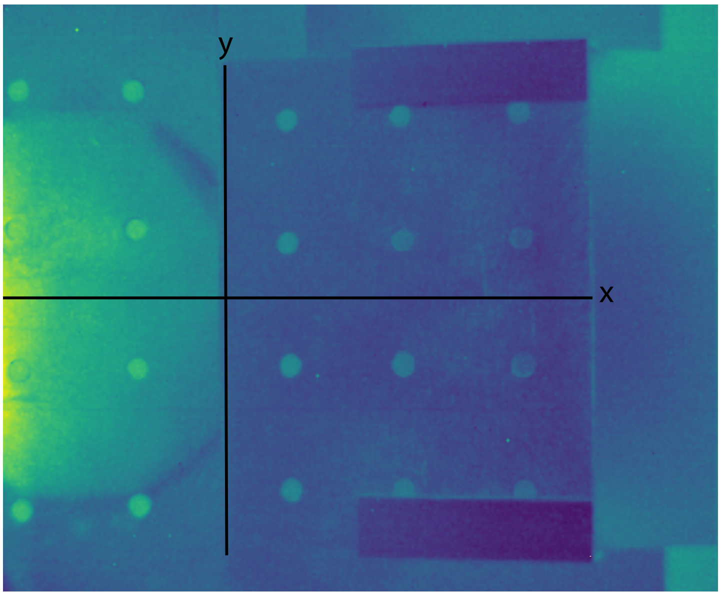

Figure 4.20: Infrared camera image of the model with calibration plates.

The coordinates of the heat flux image are then interpolated to the coordinates known from the CAD model. The idea behind this, is to have an array of actual x-coordinates. In this array the x-coordinates are the x-locations of two holes of the flat plate calibration plate, the leading edge of the ramp, the holes of the ramp calibration plate and the end of the ramp calibration plate. The origin of the x-coordinates is set at the ramp leading edge. For the 30° ramp this gives for example: $x_{act} = [-50, -20, 0, (17.5, 47.5, 77.5, 82) \cdot \cos(30°), 120]$. The cosine is to project the hole location on the ramp, to the flat plate underneath it. From Figure 4.20 the pixel locations are known, which are for the 30° ramp: $x_{meas} = [38.6, 86.1, 120.3, 146.0, 192.0, 239.2, 242.3, 316.8]$. A 1D interpolation function is made to map the measured x-coordinates to the actual coordinates ($x_{meas} \rightarrow x_{act}$). This makes it possible to enter the x-coordinate of the actual experiment in the interpolation function and the x-coordinates are converted to the actual coordinates. For the y-coordinates a similiar procedure is followed, but then in the spanwise direction. The interpolation locations are chosen to be in the centerline of the model and near the reattachment location, which is on the black lines in Figure 4.20 and 4.19. This means that the locations further away of the interpolation location have a slight error, but at the reattachment location and the centerline the interpolation is accurate.

The camera is configured to record for 1 s, but the actual run is in the order of 100 ms. This is done to make sure that the full run is captured. This means that at $f = 200$ Hz, 200 frames are obtained. In Figure 4.21 the variation heat flux in time is given for a point on the ramp. The actual usable run is between the red dots. The usable run is detected by looking at the gradients of the heat-flux in time. The first jump in the first derivative is the start of the run, the second jump is the end of the run.

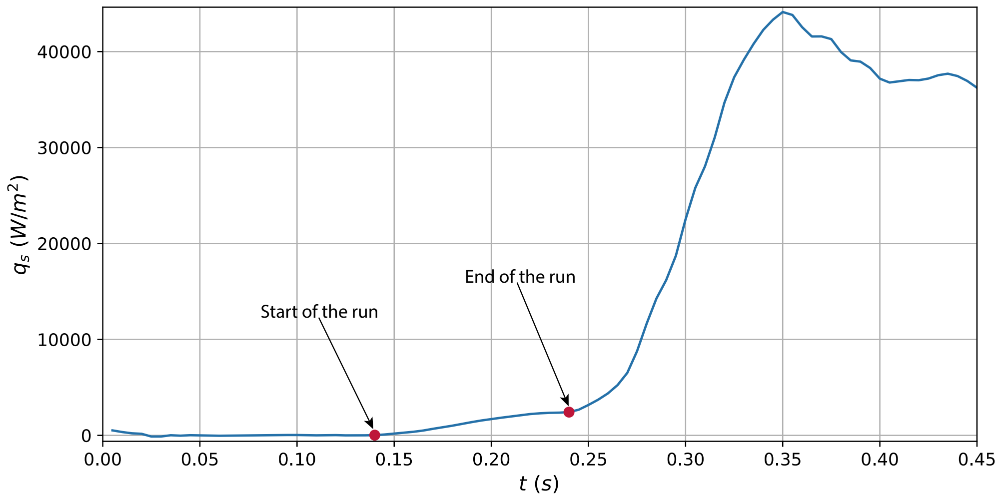

Figure 4.21: Heat flux during a run.

Now, the pixels are converted to physical locations and the frames of the run are known, the heat flux distribution can be found on the centerline. As seen in Figure 4.21, there is some variation in time, also there is some spanwise variation in heat flux over the ramp. Therefore, the data is averaged over the second half of the run in time and ±25% in spanwise direction. From this averaged centerline heat flux distribution, the peak heat flux can easily be recognized as shown in Figure 4.22. These peak heat fluxes can then be compared with the correlations given in Section 2.5.

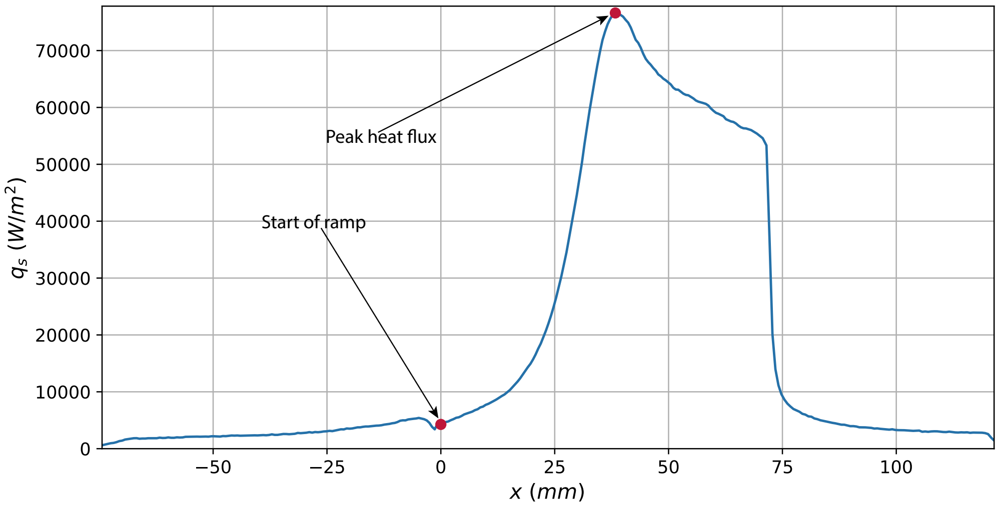

Figure 4.22: Heat flux taken over the centerline for the 30° compression ramp and $Re_L = 5.30 \cdot 10^6$.

In Figure 4.23 the heat flux field of a measurement is given. In this figure spanwise streaks are seen near the highest heat flux location. These streaks are better seen when looking at the spanwise cross section near the heat flux peak region in Figure 4.24. In this figure the ramp starts at $y = -60$, which is the result of the mapping explained above. Looking at the heat flux on the ramp, it is seen that there are some 3D effects present which influence the distribution near the side of the ramp. In order to perform a Fourier Transform on the data, this has to be corrected.

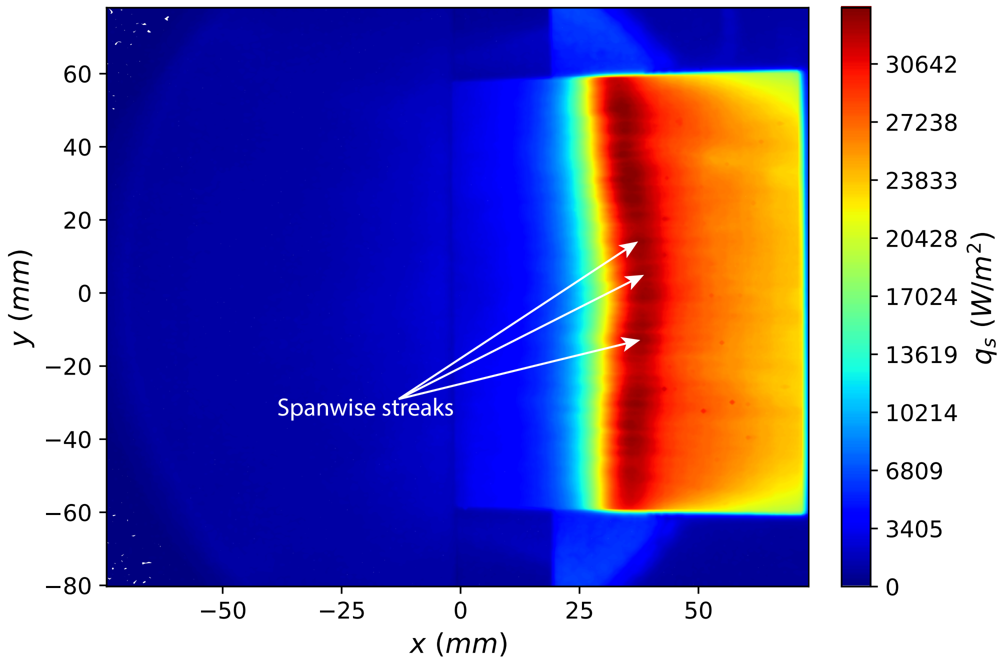

Figure 4.23: Heat flux distribution for the 30° ramp and a leading edge Reynolds number of $Re_L = 5.30 \cdot 10^6$.

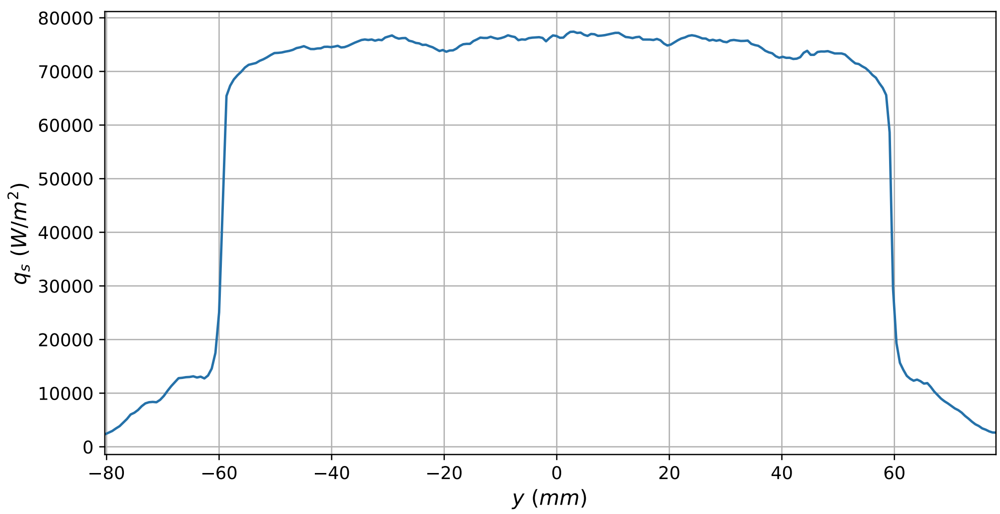

Figure 4.24: Spanwise distribution of the maximum heat flux for the 30° compression ramp and $Re_L = 5.30 \cdot 10^6$.

The correction is done by interpolating the plateau with a 8^{th} order polynomial, which is then subtracted from the raw data. The result is shown in Figure 4.25. In this figure, the original data minus the mean and the corrected data is given. In the corrected data it is observed that the 3D effects near the edge of the ramp are removed. This aids in finding the wavelength with a Fourier Transform.

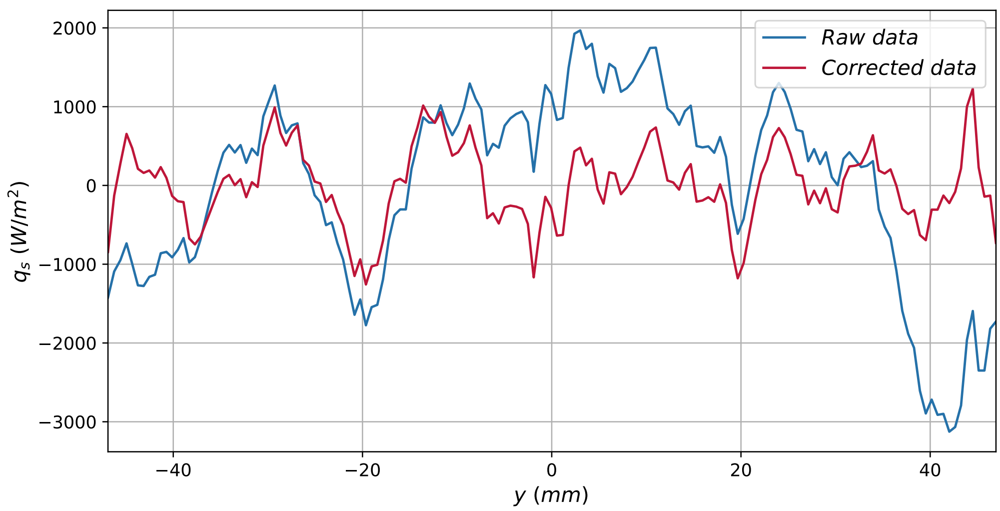

Figure 4.25: Corrected heat flux distribution of the maximum heat flux for the 30° compression ramp and $Re_L = 5.30 \cdot 10^6$.

Then, a Fast Fourier Transform (FFT) algorithm is performed. The whole second half of the run in time and ±25 data points before and after the peak value are used in the FFT. The highest peak is found to be the wavelength with the largest energy content and is taken to be the primary wavelength. Furthermore, a second relative peak is found as secondary wavelength. The wavelength is then non-dimensionalized with the following equation:

$$\Lambda = \frac{2\pi\delta_L}{\lambda} \tag{4.24}$$

In this equation Λ is the non-dimensional wavelength. δ_L is the boundary-layer thickness at the start of the ramp obtained with the reference temperature method of Section 2.2.1. λ is in this case the length of the span divided with the amount of waves found with the Fourier transform. The whole process is summarized in the flowchart given in Figure 4.26.

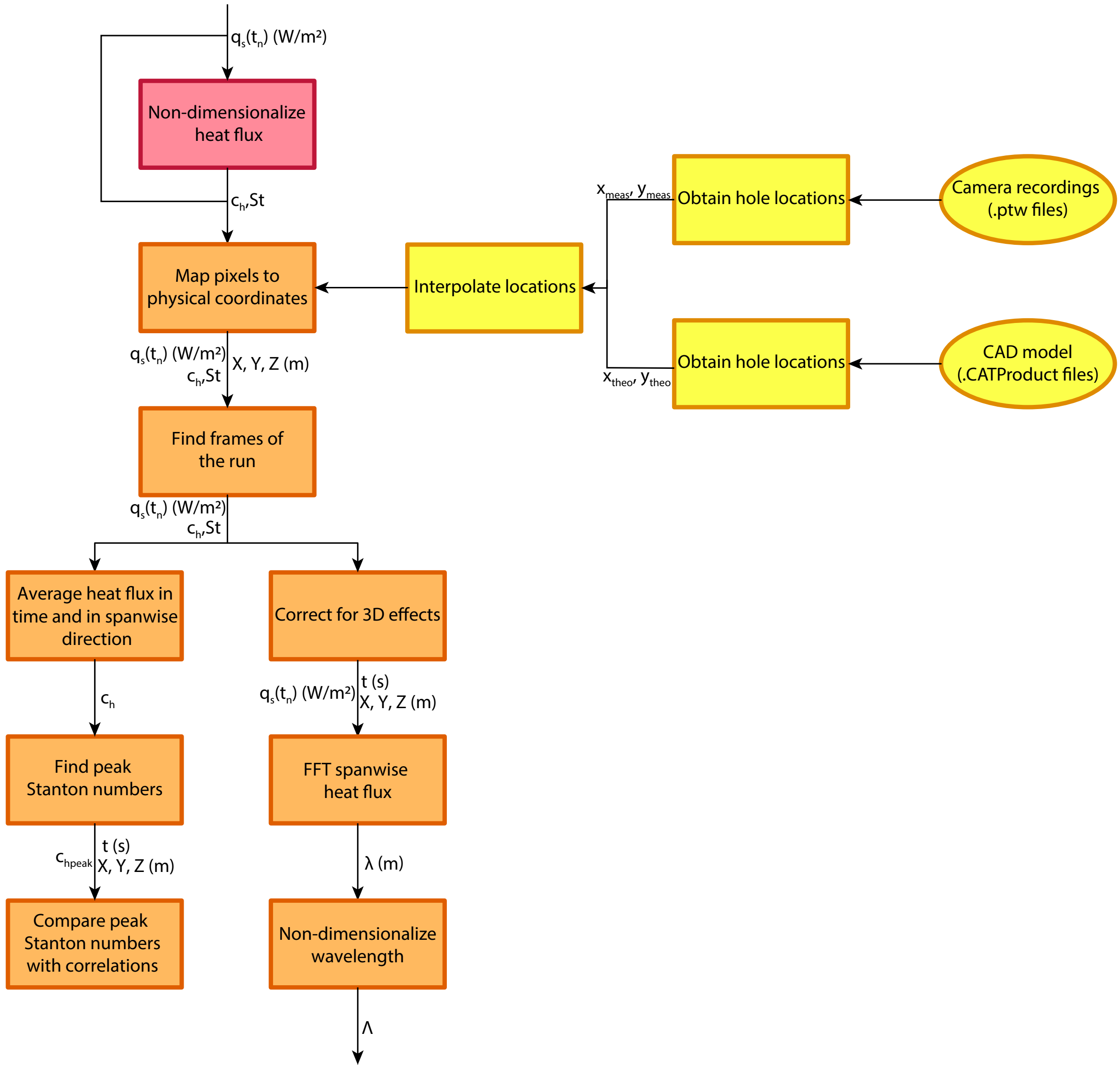

Figure 4.26: Flowchart of processing of the heat flux.

5

Schlieren Imaging Results

In this chapter the results obtained with Schlieren imaging are presented. First, the general flow lay-out is discussed in Section 5.1. In this section the different features found in the Schlieren images are briefly discussed. After that, Section 5.2 discusses the general flow topology. This means, that a closer look is taken at the shear layer angle and the shear layer length and what the effect of the ramp angle and Reynolds number is on them. This is then compared to theory and empirical correlations found in Section 2.5. Then, Section 5.3 focuses more on the transitional behavior of the shear layer. This consists of looking at the wavelength and growth rate of the waves. Also a close up of the waves is given. At last, in Section 5.4 the uncertainties of the analysis are discussed.

When data is presented in this chapter errorbars and means are used. The errorbars are calculated using the minimum and maximum rule of a boxplot. The markers in the figures are the means of the data with the outliers removed.

5.1. General Flow Topology

Figure 5.1 shows a Schlieren image for a 30° ramp at a ramp leading edge Reynolds number of $Re_L = 5.30 \cdot 10^6$. Comparing this figure with the theoretical flow field in Figure 2.9 shows several similarities such as a shear layer and a corresponding separation shock wave and reattachment shock wave. However, in Figure 5.1 extra phenomena are present, such as waves in the shear layer. Furthermore, the waves are so strong, that compression waves are formed. The waves point at a transitional shear layer instead of the laminar or turbulent shear layer. In this chapter, the phenomena captured in this and similar images obtained with Schlieren are discussed and analyzed.

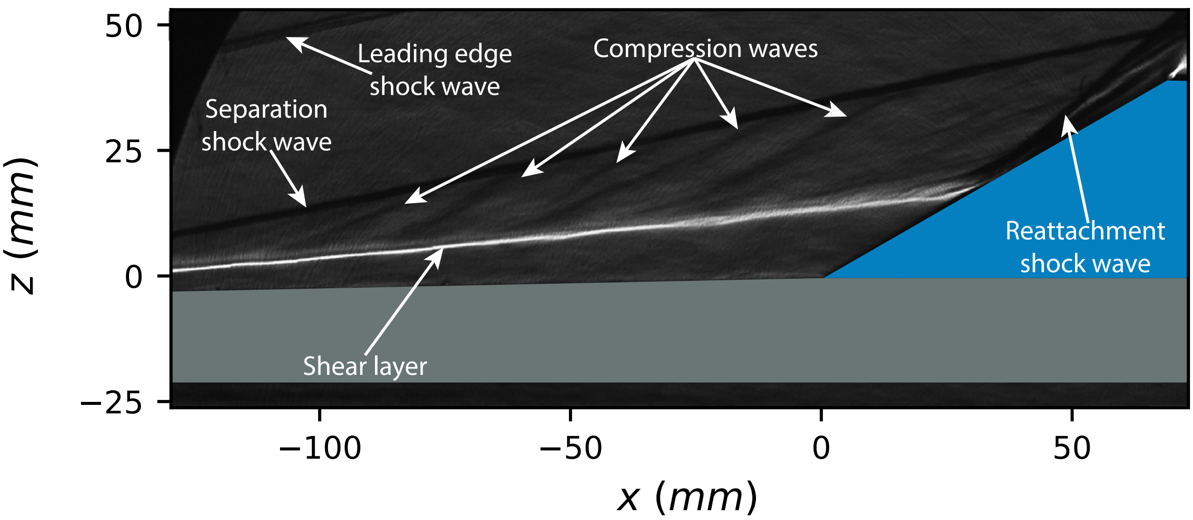

Figure 5.1: Example of a Schlieren image for the 30° ramp and a leading edge Reynolds number of $Re_L = 5.30 \cdot 10^6$.

5.2. Flow Topology

In Figures 5.3-5.7, Schlieren images are shown for the different ramps. All the images are made at a ramp leading edge Reynolds number of $Re_L = 5.30 \cdot 10^6$. At first, it is noticed that in all cases the flow is separated. Figure 5.2 shows the theoretical incipient separation ramp angles for different Reynolds numbers obtained with Equation 2.25. It shows that for the whole Reynolds number range, the incipient separation ramp angle is lower than 10°, the smallest ramp investigated. This is consistent with the results found during the experiments, where in all cases there was flow separation.

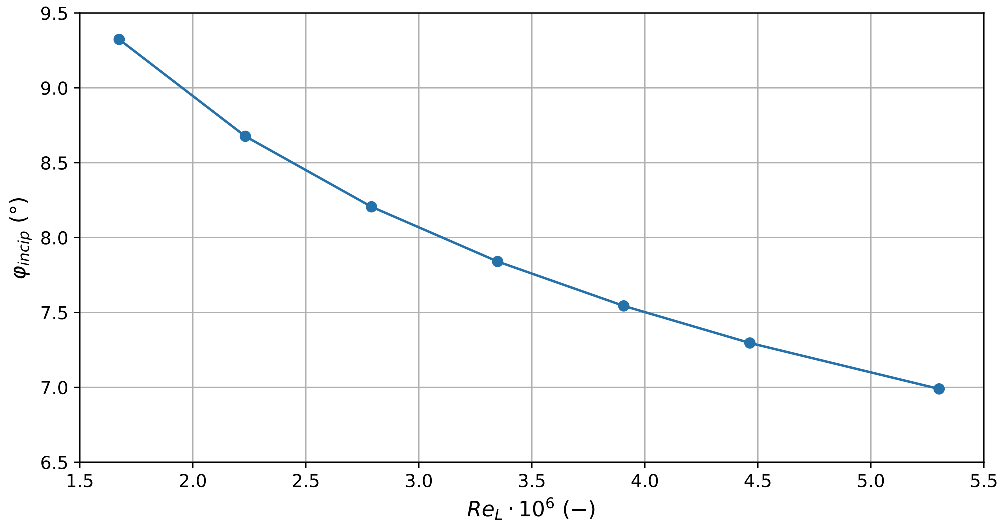

Figure 5.2: Incipient separation ramp angles (φ_{incip}) as function of Reynolds number.

The second thing that is observed, is that the flow does not reattach on the ramp in the case of the 10° ramp. The combination of the length of the shear layer and the shear layer angle results in the shear layer going over the ramp. This means that it is not a classical shock wave boundary-layer interaction, which is the topic of this research. Therefore, the 10° ramp is not used for the remainder of the experiments.

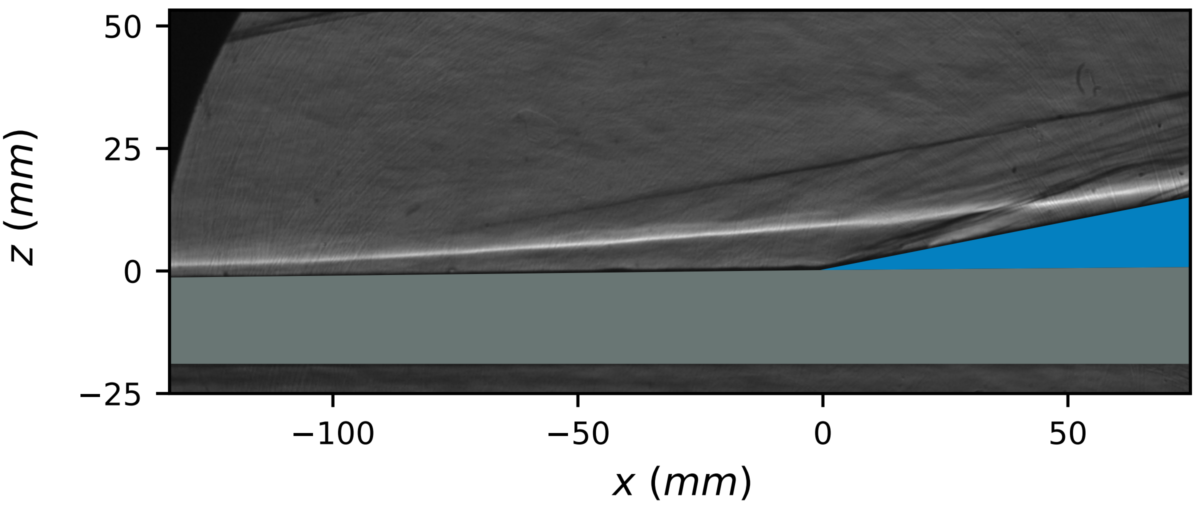

Figure 5.3: Schlieren image for the 10° ramp with $Re_L = 5.30 \cdot 10^6$.

The flow fields of the 15° and 20° ramps show the separation point of the boundary-layer. Increasing the ramp angle, shifts the separation point upstream, outside the image. Therefore an extrapolation has to be performed to find the shear layer length. As explained in Section 4.1, the shock wave and shear layer are linearly extrapolated until they intersect. The flow field of the 15° ramp angle is used to validate this approach. Figure 5.4 shows that near the separation region, both the shock wave and shear layer are very straight, and therefore a linear extrapolation is allowed. Furthermore, when the intersection between the shock wave and shear layer is compared to the actual separation point, a small error of 5 mm is found. However, it should be noted that finding the actual separation point is also prone to errors due to the gradual start of the separation as shown in Figure 5.4.

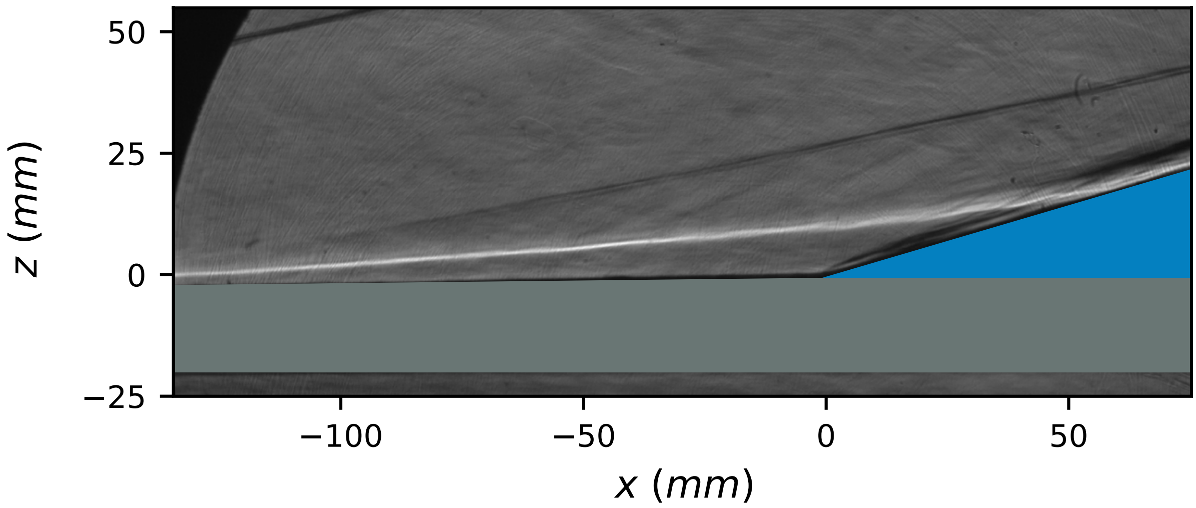

Figure 5.4: Schlieren image for the 15° ramp with $Re_L = 5.30 \cdot 10^6$.

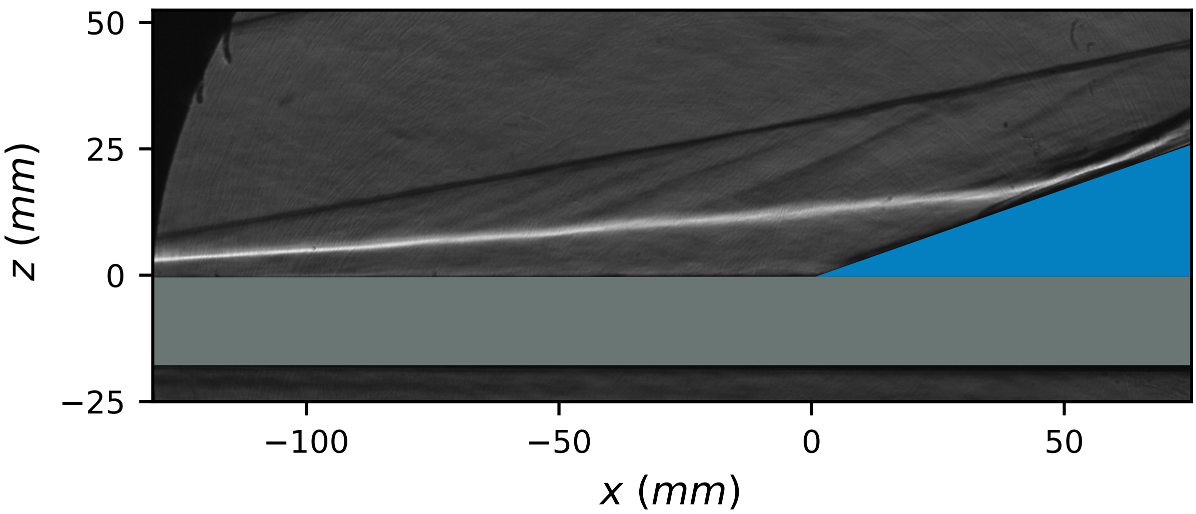

Figure 5.5: Schlieren image for the 20° ramp with $Re_L = 5.30 \cdot 10^6$.

On the 15° and 20° ramp, the reattachment shock wave angle has a very small angle and lies therefore almost flat on the ramp. Increasing the ramp angle further, requires the strength of the reattachment shock wave to increase. For an oblique shock wave this is manifested as an increase in shock angle. In Figures 5.6 and 5.7 this effect is observed, for both ramp angles the reattachment shock wave has a higher shock wave angle compared to the flatter ramps. The reattachment shock wave angle on the 30° ramp has become so large that, the shock-shock interaction is now present in the image.

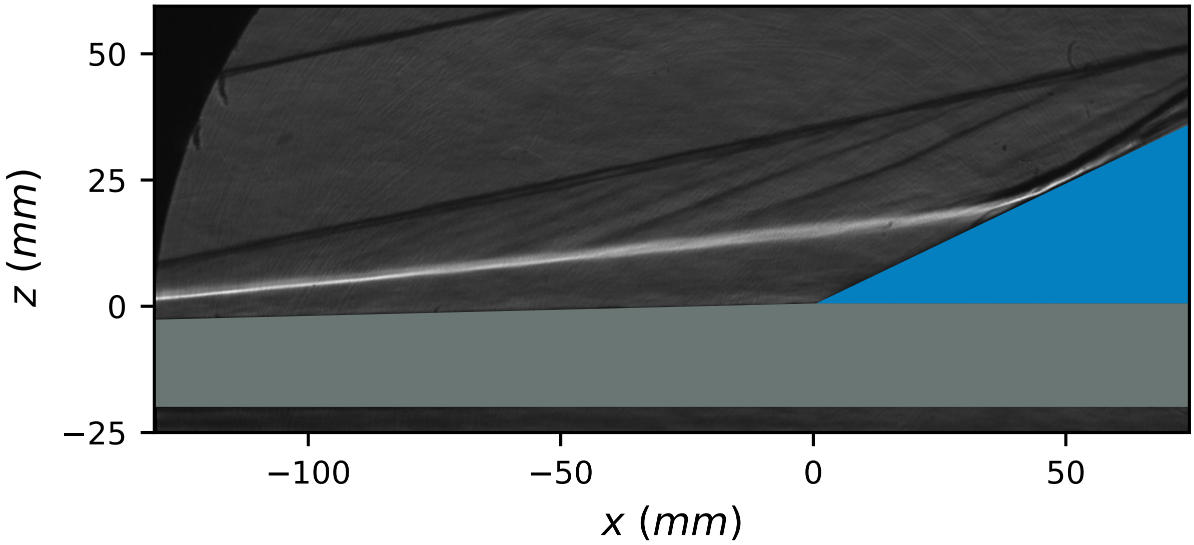

Figure 5.6: Schlieren image for the 25° ramp with $Re_L = 5.30 \cdot 10^6$.

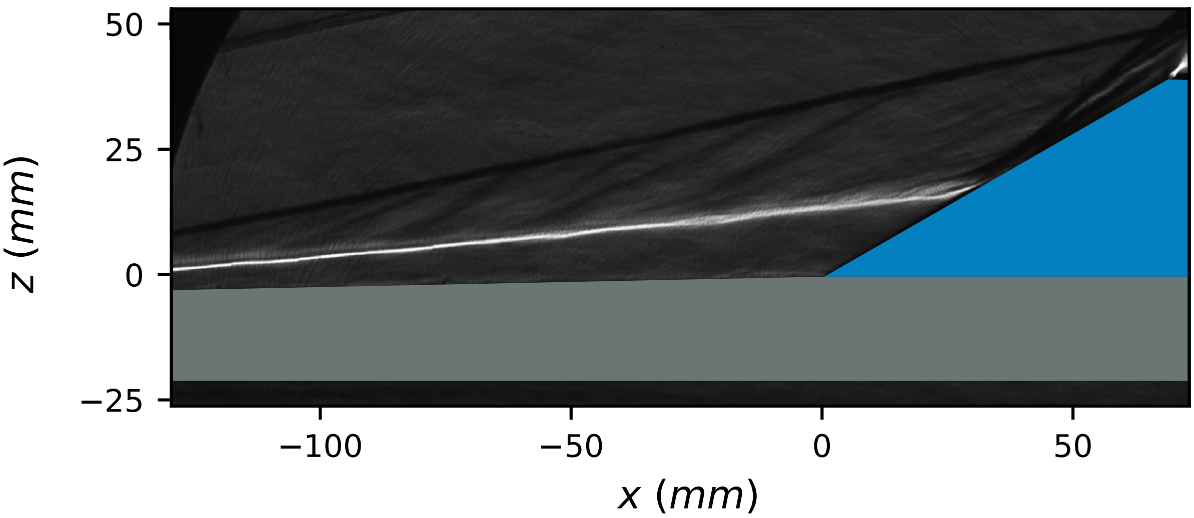

Figure 5.7: Schlieren image for the 30° ramp with $Re_L = 5.30 \cdot 10^6$.

As explained in Section 4.1.3, for the majority of the experiments a continuous burning LED lamp and a camera with an exposure time of 1 μs are used. This means that unsteady structures that move or rotate in a time in the order of 1 μs or larger, are captured by the camera. However, a lot of structures in turbulent and transitional flow have a time scale lower than that. This means, that the average of the these structures is found. To circumvent this, a spark light is used. This light flashes in the order of nano seconds meaning that high frequency structures are observed without the averaging effect. This result is shown in Figure 5.8. For this image the Schlieren knife is upside down, so compressions are shown in white and expansions in black. The figure shows that at reattachment a very sharp and strong shock wave is formed. Also, especially between the reattachment shock wave and the ramp incoherent, high frequency structures are present. Next to that, it appears that two separation shock waves are present instead of one. This is the result 3D effects in the spanwise direction.

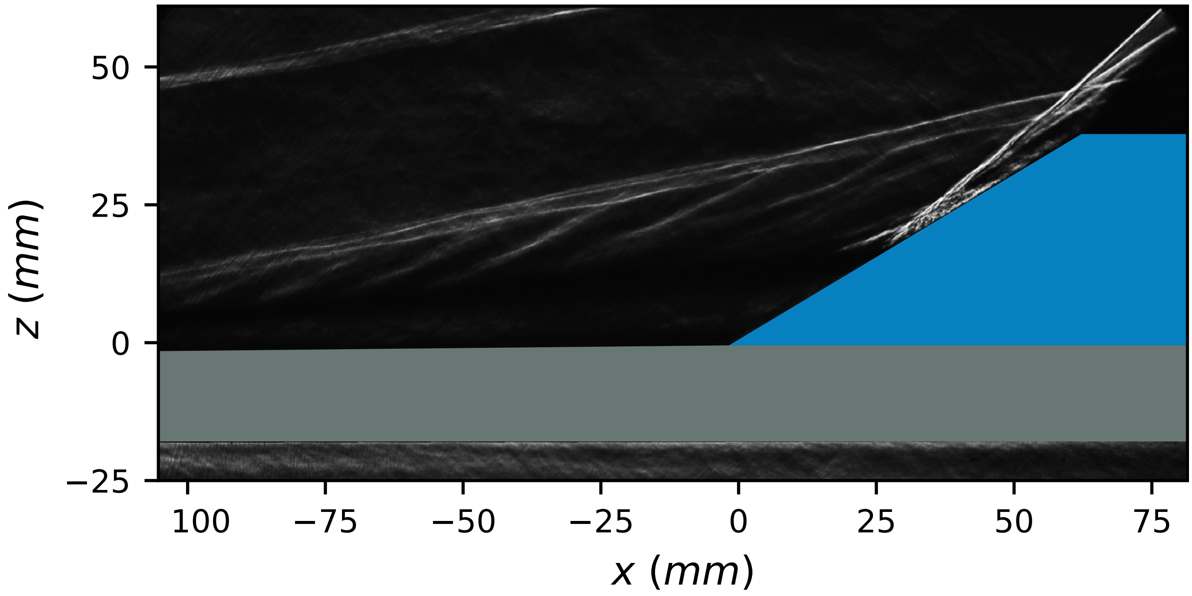

Figure 5.8: Schlieren image for the 30° ramp with $Re_L = 5.30 \cdot 10^6$.

Figure 5.9 shows the flow field at a Reynolds number of $Re_L = 1.67 \cdot 10^6$. Comparing this to the case of $Re_L = 5.30 \cdot 10^6$ in Figure 5.7 shows that the intensity of the shear layer in the image is a lot lower for the low Reynolds number case. As the intensity is coupled to density changes, this means that the expansion over the shear layer is a lot weaker for low Reynolds numbers than for high Reynolds numbers. The effect on the length of the shear layer and the shear layer angle is hard to observe. This is because the separation onset falls outside the image. A detailed description of this is given in respectively Section 5.2.1 and 5.2.2. Also the compression waves, which are clearly seen in the higher Reynolds number case, are not observed in Figure 5.9. This difference is discussed in Section 5.3.

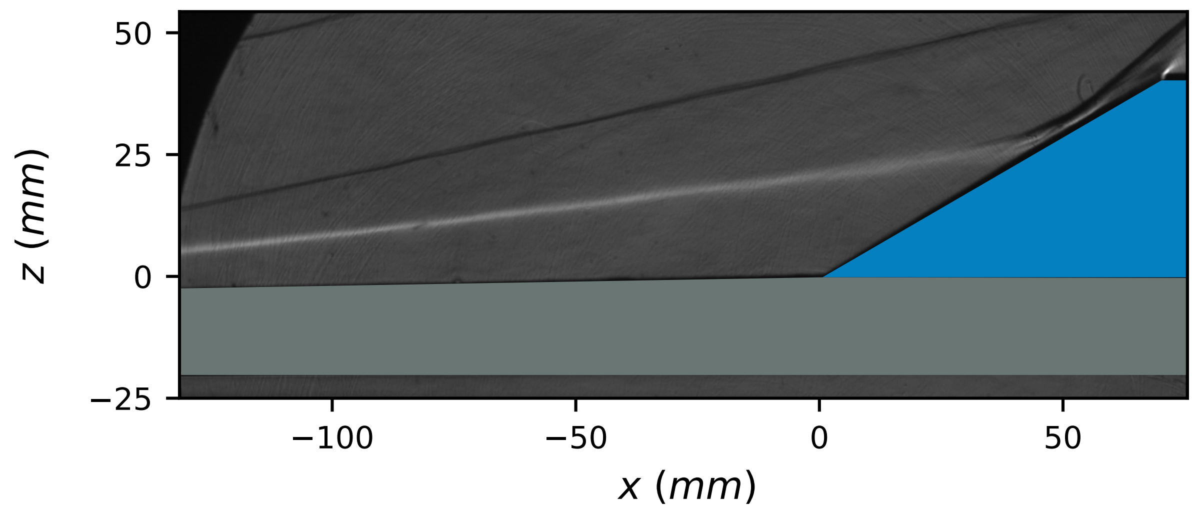

Figure 5.9: Schlieren image for the 30° ramp with $Re_L = 1.67 \cdot 10^6$.

5.2.1. Shear Layer Length

The shear layer length is determined by identifying the cross section of the separation shock wave and shear layer in every Schlieren image. An example of this procedure is shown in Figure 5.10. The green line is the shock wave, the blue line is the maximum intensity found in the image, which corresponds to the shear layer. The orange line is a straight line fitted to the first linear part of the shear layer as explained in Section 4.1.4. Only near reattachment the shear layer is not straight anymore and a difference between the blue and orange line is present. The curvature and how far it extends is not constant and also varies with the ramp angle and

Reynolds number.

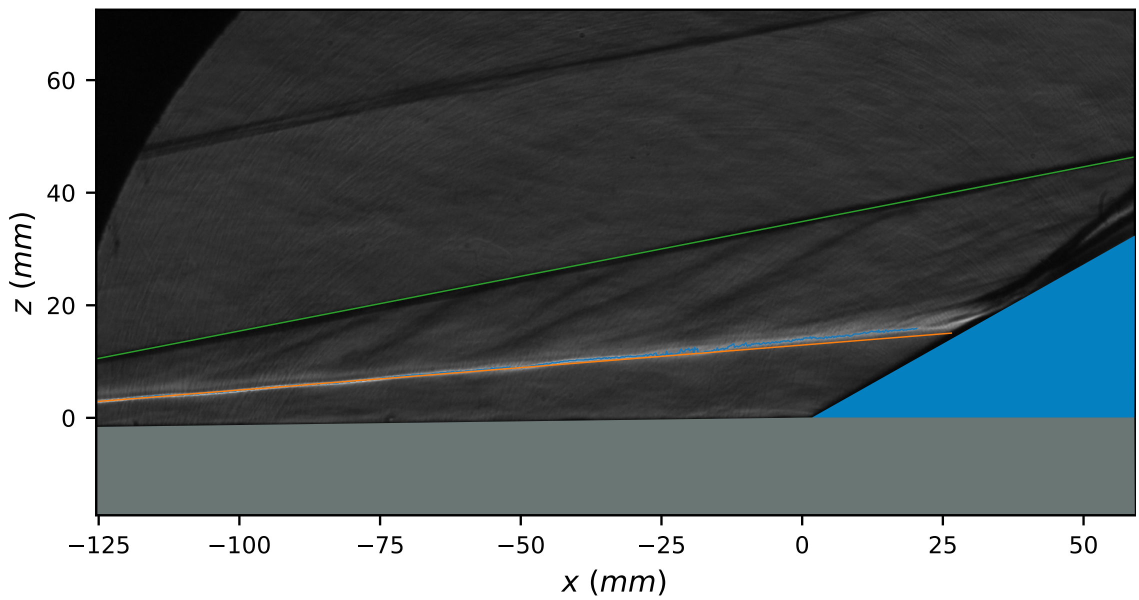

Figure 5.10: Processed Schlieren image for the 30° ramp with $Re_L = 5.30 \cdot 10^6$.

To obtain the shear layer length, the shock wave and shear layer are extrapolated. The result of the extrapolation is shown in Figure 5.11. The shear layer length is then defined by the length of the orange line.

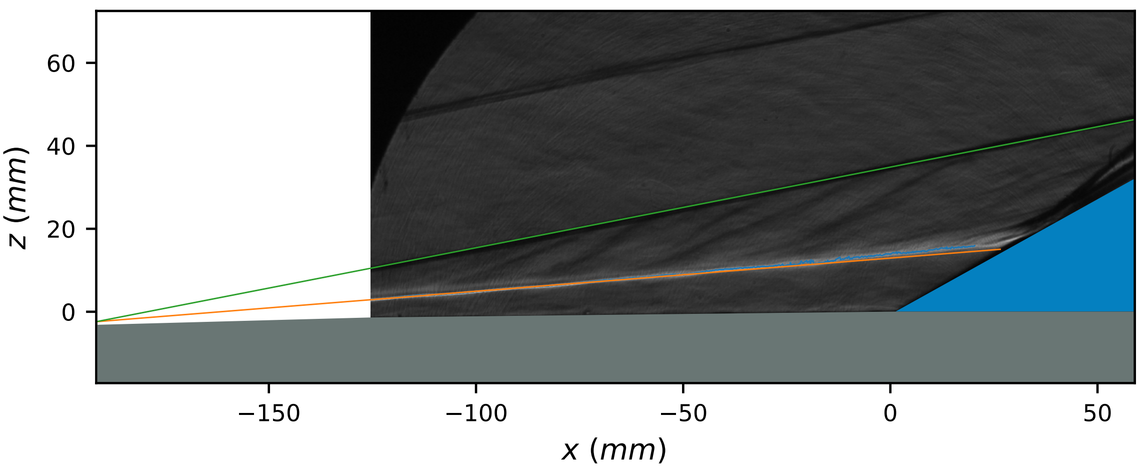

Figure 5.11: Extrapolated Schlieren image for the 30° ramp with $Re_L = 5.30 \cdot 10^6$.

As stated above, the extrapolation is validated by performing the extrapolation for the cases where the complete separation bubble is visible. This shows that a linear extrapolation until the intersection between the shear layer and shock wave is a good approximation for the separation point. For the higher ramps this validation is not possible because the separation points are upstream of the image. To get a feeling of the curvature of the shear layer upstream of the image, the observed shock wave angle is compared to the shock wave angle found by filling in the shear layer angle in the oblique shock relations stated in Section 2.1. If the shear layer angle estimated with the extrapolation is straight, then the shock wave angle calculated based on this shear layer angle should be close to the experimental shock wave angle.

The result is given in Figure 5.12 for the 15° ramp and in Figure 5.13 for the 30° ramp. Overall the difference between the two are lower than 1° and within the error margin. Therefore, choosing the intersection of the shear layer and shock wave as separation point is accurate enough for this analysis.

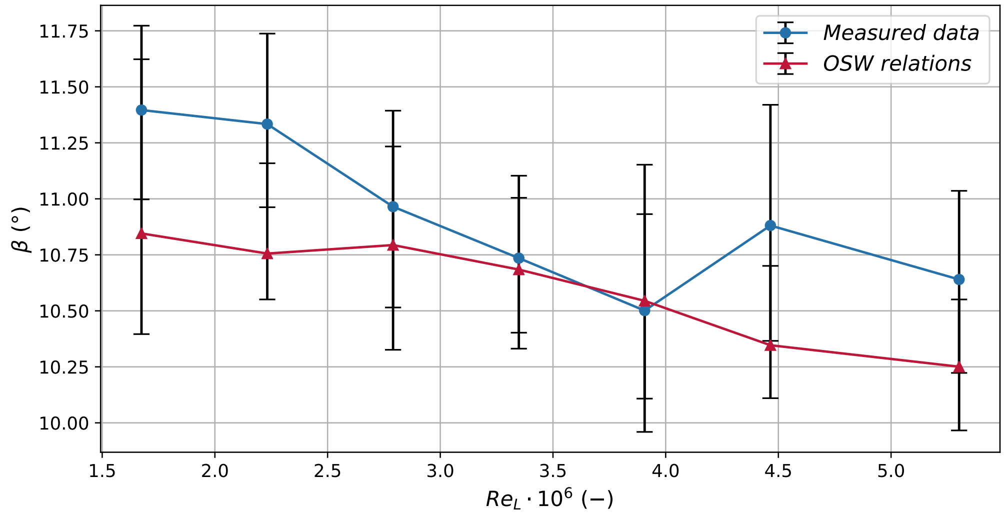

Figure 5.12: Comparison between measured and theoretical shock wave angles (β) for the 15° ramp as function of Reynolds number.

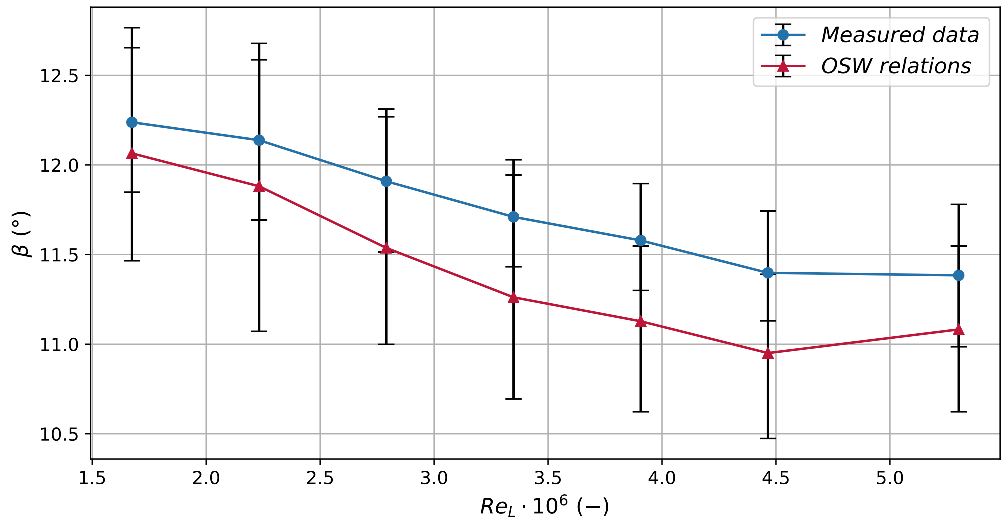

Figure 5.13: Comparison between measured and theoretical shock wave angles (β) for the 30° ramp as function of Reynolds number.

Both the effects of increasing the ramp angle and changing the Reynolds number on the shear layer length are investigated. Figure 5.14 shows the effect of the Reynolds number for the 15° and 30° ramp. The figure is normalized with the boundary-layer thickness at the interaction location (δ_0). The boundary-layer thickness is obtained using the reference temperature method stated in Section 2.2.1.

The figure shows that there is an increase in shear layer length for increasing Reynolds number. Furthermore, higher ramp angles increase the separation length further. In Chapter 2 it was found that this result is expected for $Re_\delta < 10^5$. The maximum boundary-layer thickness Reynolds number (Re_δ) found in the experiments equals $Re_\delta = 0.4 \cdot 10^5$. This means that an increase of shear layer length with Reynolds number is consistent with experiments reported in literature [5].

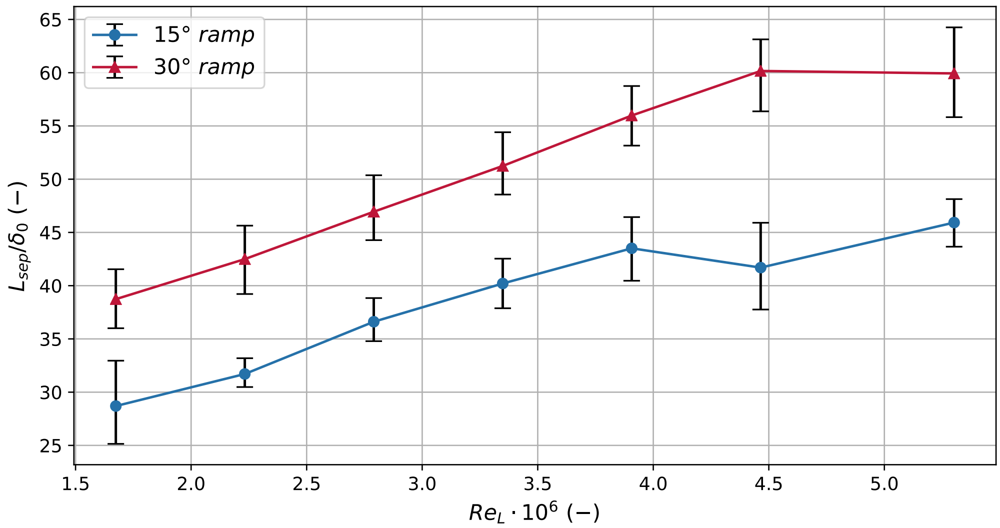

Figure 5.14: Shear layer length (L_{sep}/δ_0) for the 15° ramp and 30° ramp as function of Reynolds number.

Concerning the effect of the ramp angle, Figure 5.15 shows the shear layer length as function of ramp angle for a Reynolds number of $Re_L = 1.67 \cdot 10^6$ and $Re_L = 5.30 \cdot 10^6$. Increasing the ramp angle increases in both cases the shear layer length. Looking at Chapter 2, this confirms the free-interaction theory. The free-interaction theory states that the initial compression at the separation shock wave is constant and that the remainder of the required compression is done at reattachment. Increasing the ramp angle, increases the total required pressure jump, as a result the pressure jump at reattachment also has to increase. The shear layer has to overcome this additional reattachment pressure, the only way to do this is by increasing the maximum velocity on the dividing streamline as seen in Figure 2.9. To increase this momentum exchange between the outer flow and the streamline, a longer shear layer is required.

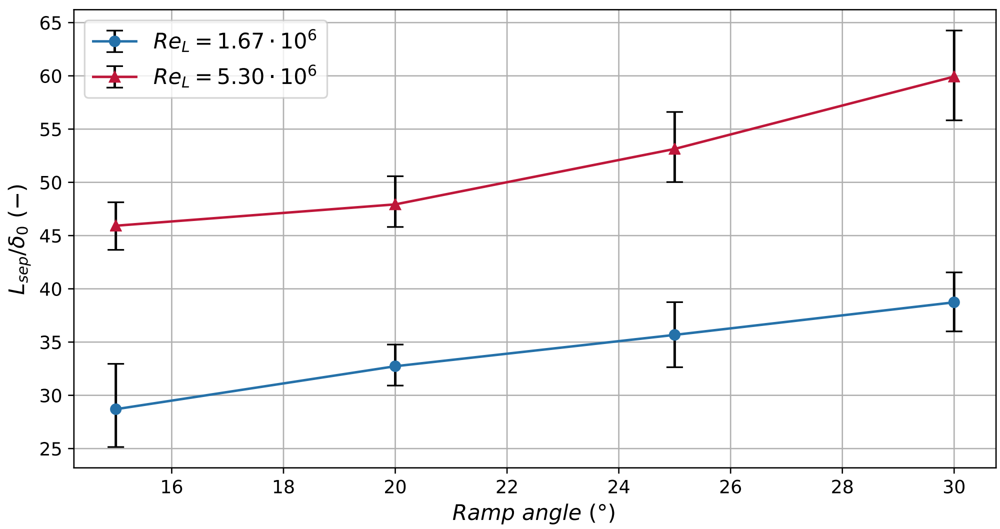

Figure 5.15: Shear layer length (L_{sep}/δ_0) as function of ramp angle at $Re_L = 1.67 \cdot 10^6$ and $Re_L = 5.30 \cdot 10^6$.

At last, the shear layer length correlations found in Section 2.5 are compared to the data found with the experiments. First this is done for Equation 2.27. The result is shown Figures 5.16 and 5.17 for two different ramp angles. In these figures the shear layer length is normalized with the boundary-layer displacement thickness at the interaction location (δ_0^*).

Figure 5.16 shows that the correlation agrees well with the experimental data. For the 20° ramp it underestimates the shear layer length. At 25°, the correlation starts to overestimate the shear layer length as seen in Appendix B.2. For 30° the overestimation is even larger.

A potential reason for failing to capture the effect of the ramp angle is the limited range for which Equation 2.27 is correlated, $1.4 \leq \frac{p_3}{p_1} \leq 1.61$, $1.4 \leq M_1 \leq 3.4$ and $10^5 \leq Re_{x_0} \leq 6 \cdot 10^5$[8]. Because the ramp angles and higher Mach numbers in these experiments cause significant higher pressure jumps, it can be expected that the equation is not correctly correlated for this range. This means that a re-calibration of the equation with higher Mach numbers and pressure jumps can result in a correct prediction of the shear layer length in the low hypersonic range.

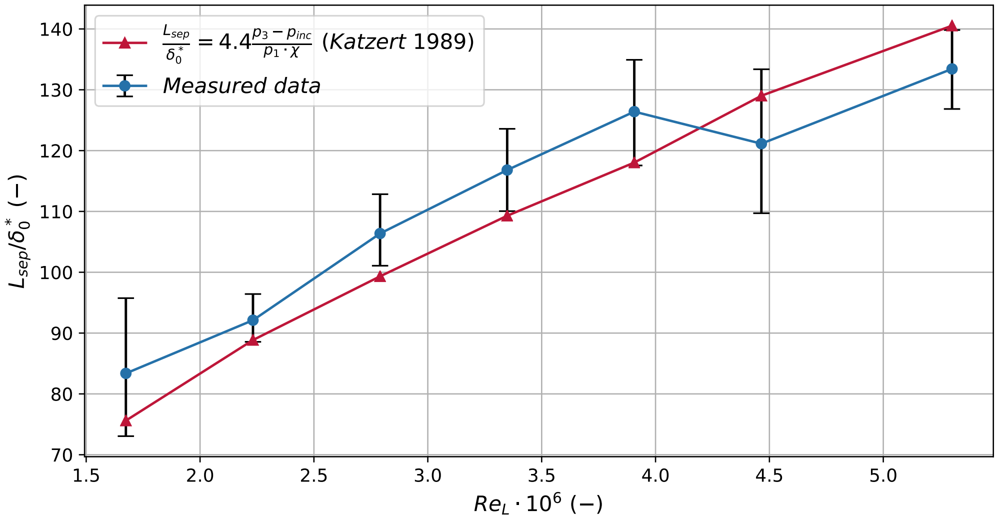

Figure 5.16: Shear layer length (L_{sep}/δ_0^*) and theoretical data from Equation 2.27 for the 15° ramp as function of Reynolds number.

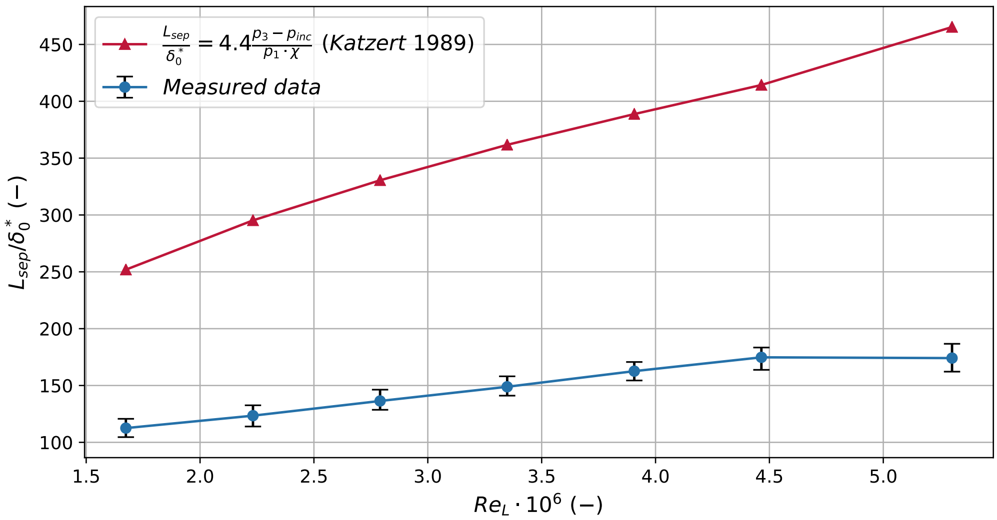

Figure 5.17: Shear layer length (L_{sep}/δ_0^*) and theoretical data from Equation 2.27 for the 30° ramp as function of Reynolds number.

The other equation that is compared to the experimental results is the equation from [9] stated in Equation 2.29. Looking at the result in Figure 5.18 and 5.19, it shows that the equation completely diverges from the data in all cases.

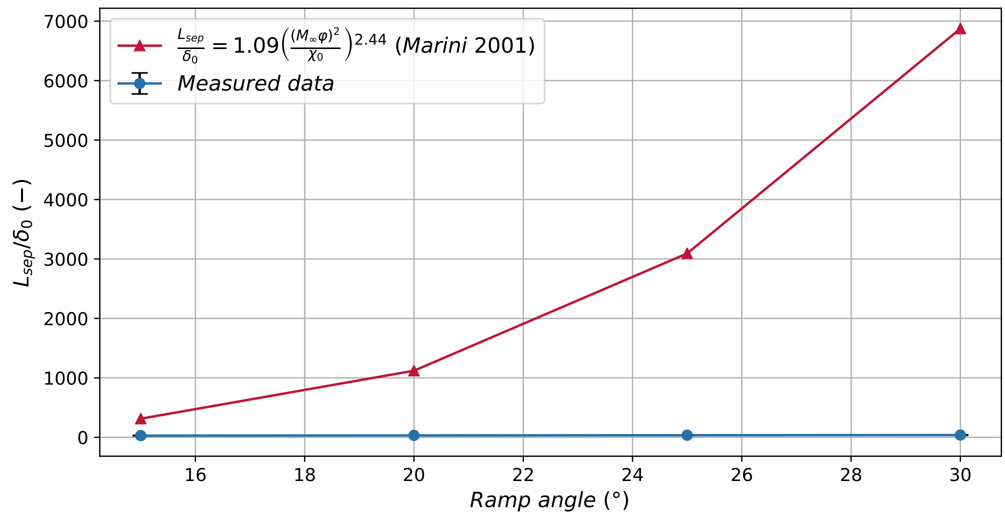

Figure 5.18: Shear layer length (L_{sep}/δ_0) and theoretical data from Equation 2.29 as function of ramp angle at $Re_L = 1.67 \cdot 10^6$.

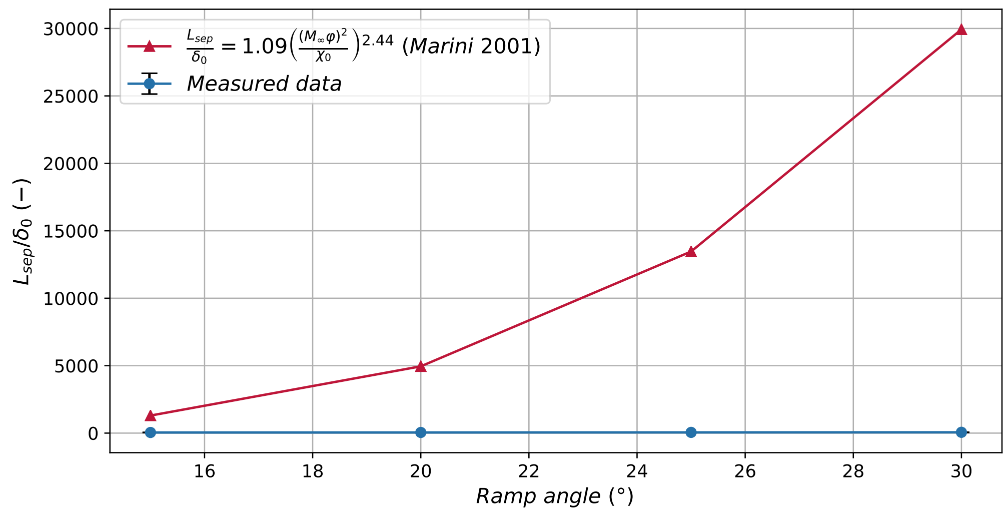

Figure 5.19: Shear layer length (L_{sep}/δ_0) and theoretical data from Equation 2.29 as function of ramp angle at $Re_L = 5.30 \cdot 10^6$.

In contrary to the previous correlation, this correlation is valid in the Mach number range of the experiments. However, extending Figure 2.15 with the experimental data, it shows that the experiments fall completely out of the applicable range of Equation 2.29. This is shown in Figure 5.20, where a representative selection of the newly obtained experimental results are added with triangles. Looking at the graph it shows that the experiments are far away from the correlation lines. Furthermore, because the equation scales with the power of 2.44, the deviation is strongly amplified.

The reason that these experiments are not in the range of the correlation is due to the high Reynolds number. Comparing the Reynolds number range of the experiments with the data found in [12] it shows that at around $Re_L = 1.3 \cdot 10^6$ transition is starting. This means that at the lowest Reynolds numbers, little transitional behavior is expected and at the highest Reynolds numbers strong transitional or turbulent behavior is found. The transitional behavior is very hard to capture with correlations that are outside the transitional Reynolds number region.

Because the transitional structures promote the momentum exchange between the outer flow and separation bubble, it will reduce the shear layer length. This is also found when looking at Figure 5.20, the shear layer length is lower than expected from the correlations.

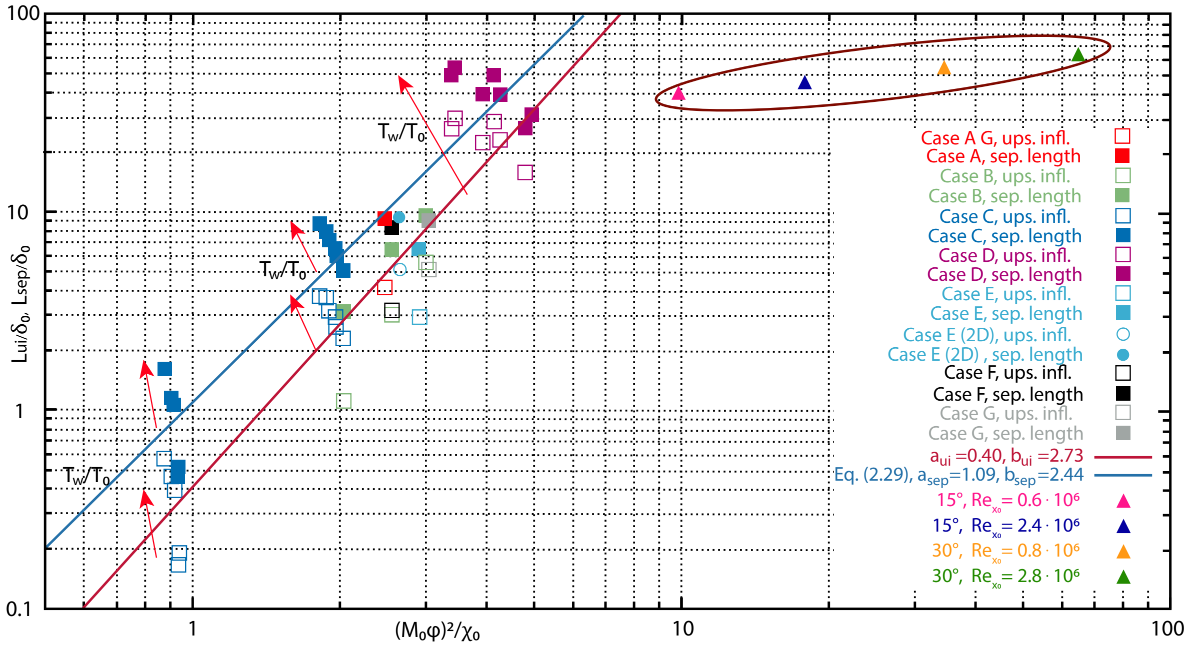

Figure 5.20: Upstream influence and separation length correlation [9] with current the experiments added.

5.2.2. Shear Layer Angle

The free-interaction theory mentioned above, states that the initial compression near the separation shock wave is independent of the flow after separation, which means that it is independent of the ramp angle. It is therefore expected that the shear layer angle is almost constant for different ramp angles. Because the Reynolds number has an effect on the skin friction coefficient at the interaction location (c_{f_0}), a dependency on the Reynolds number is expected.

Figure 5.21 shows the effect of the Reynolds number on the shear layer angle. Looking at the means of the different data points, there is a small downward trend visible of around 0.5 – 1.0°. However, the result is constant in the error margin. So no conclusive relation is found between the shear layer angle and Reynolds number.

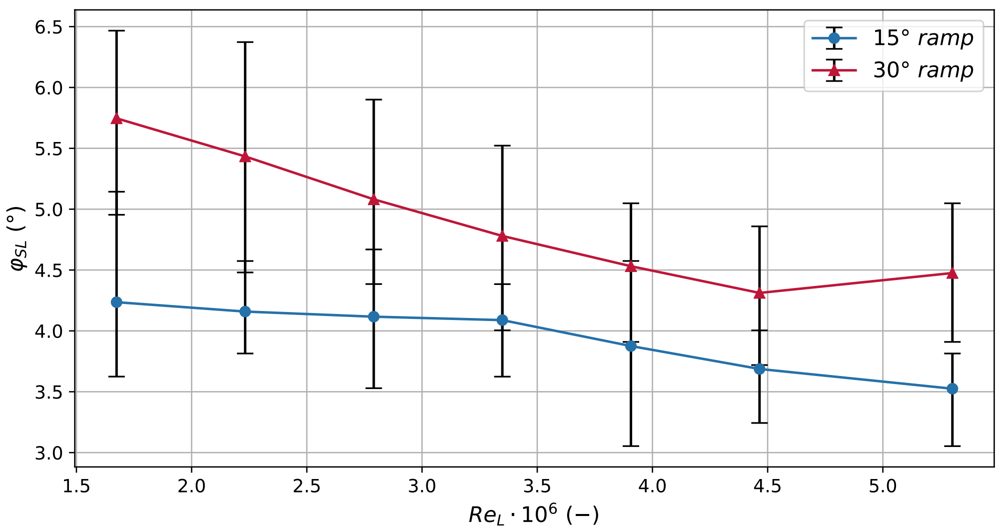

Figure 5.21: Shear layer angle (φ_{SL}) for the 15° ramp and 30° ramp as function of Reynolds number.

When evaluating the effect of increasing the ramp angle at two different Reynolds numbers, a slight increase in shear layer angle is found as is shown in Figure 5.22. A possible reason for this, is the increase in shear layer length for increasing ramp angle. As the ramp is fixed, this shifts the separation point forward. At this location a thinner boundary-layer is found, with a higher skin-friction coefficient. This can cause a reduction in shear layer angle, depending on the state of the boundary-layer.

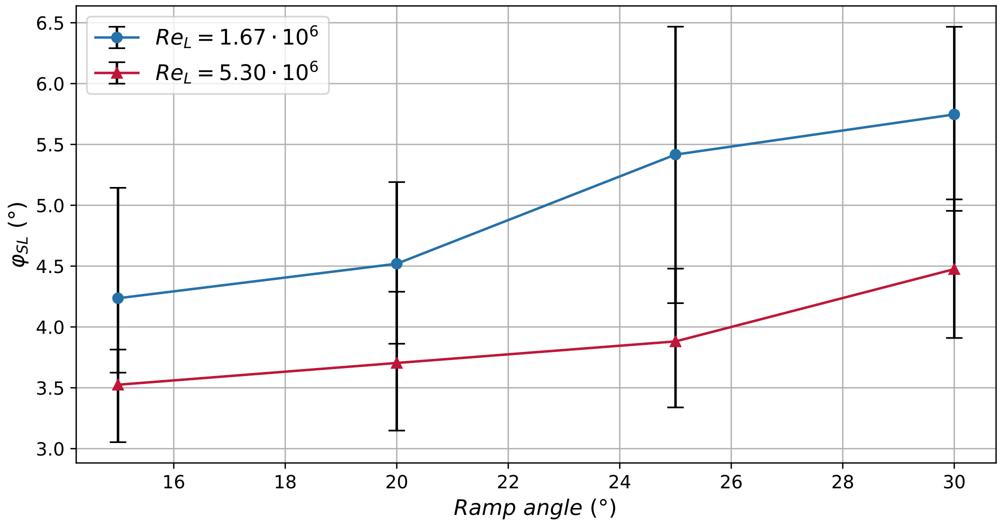

Figure 5.22: Shear layer angle (φ_{SL}) as function of ramp angle for $Re_L = 1.67 \cdot 10^6$ and $Re_L = 5.30 \cdot 10^6$.

5.3. Instability Waves

Looking at Figures 5.4-5.7 at the beginning of the chapter, clear compression waves between the shear layer and shock waves are observed for all ramp angles at a Reynolds number of $Re_L = 5.30 \cdot 10^6$. These compression waves are imposed by the undulations of the shear layer. These undulations cause local compressions and expansions in the flow. The compression is manifested as compression waves, while the expansion will be more gradual and therefore not visible.

The figures show that increasing the ramp angle, makes the compression waves stronger and therefore more visible. Comparing Figure 5.7 with Figure 5.9 shows the effect of the Reynolds number. For the low Reynolds number case, the compression waves and the undulations in the shear layer are not visible anymore. This means, that the shear layer starts transitioning in the Reynolds number range of the experiments.

From the angles of the compression waves it is possible to get an estimate of the velocity of the waves and therefore the shear layer velocity. This is only possible for the highest Reynolds case, because the waves are strong and straight enough for their angle to be measured reliably. Figure 5.23 shows an example of the angles for the 30° ramp. The cases for the 20° and 25° are shown in Appendix B.1.

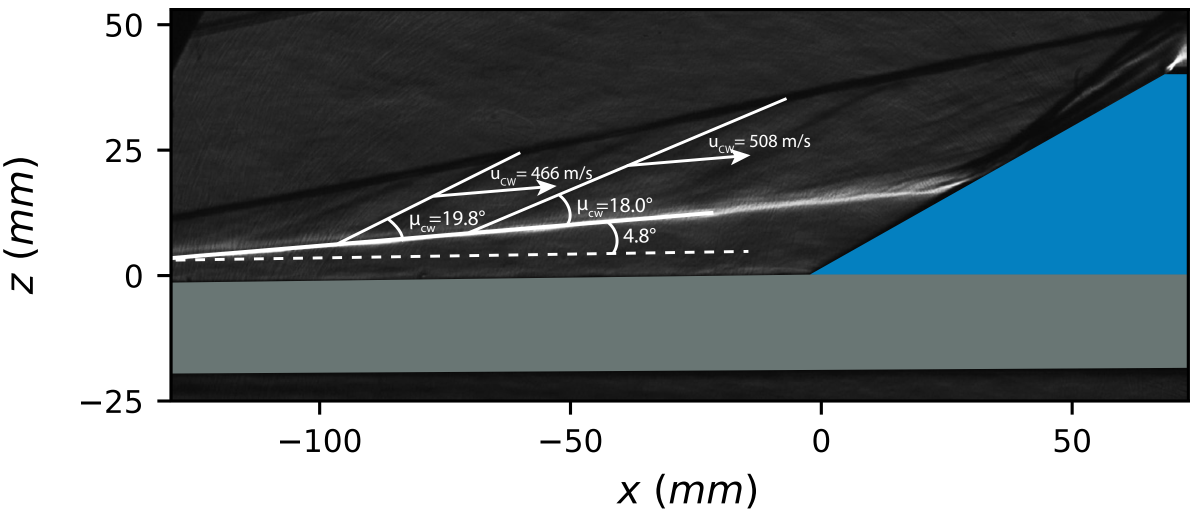

Figure 5.23: Compression wave angles of for the 30° ramp with $Re_L = 5.30 \cdot 10^6$.

Because the compression waves are assumed weak, they can be treated as Mach waves. The following equation can therefore be used to calculate the Mach number from the compression waves:

$$M_{cw} = \frac{1}{\sin \mu_{cw}} \tag{5.1}$$

The Mach number is then converted to the local velocity with the following equation:

$$u_{cw} = M_{cw}\sqrt{\gamma RT} \tag{5.2}$$

In this equation T is the temperature after the separation shock wave obtained with the oblique shock wave relations. The velocity is in the direction of the shear layer as shown in Figure 5.23. Values are found between 466−611 m/s, which is around 46−59% of the local flow velocity. What is also observed, is that the wave angles decrease towards the ramp. This shows that the shear layer is accelerating towards the ramp, this is expected as the shear layer has to obtain additional momentum to overcome the reattachment pressure jump.

A closer look into the shear layer is given in Figure 5.24. The figure shows two frames of a high speed Schlieren run zoomed in on the shear layer. The two frames clearly show a wavelike pattern in the shear layer. This shows that indeed the compression waves stem from disturbances in the shear layer, which might indicate that it undergoes transition.

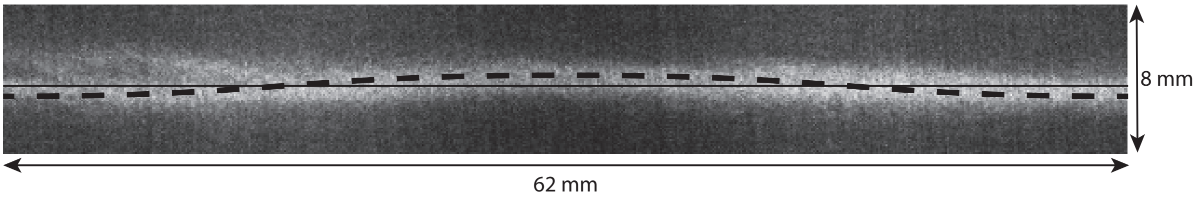

(a) Schlieren image at t.

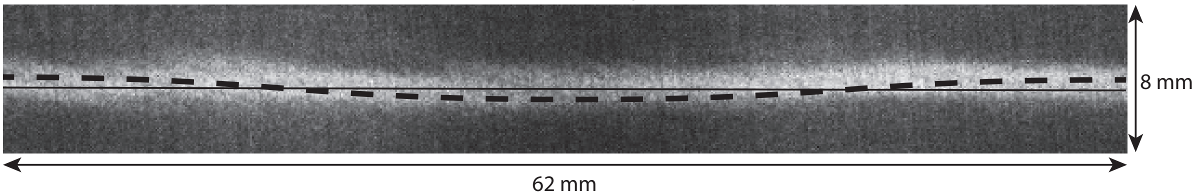

(b) Schlieren image at $t+\Delta t$, $\Delta t = 4.64 \cdot 10^{-5}$ s.

Figure 5.24: Schlieren image of the shear layer at a frame rate of 21.559 fps for the 30° ramp with $Re_L = 5.30 \cdot 10^6$.

Determining the wavelength of these waves in the whole experimental range is impossible, because the presence and visibility of the compression waves strongly depends on the Reynolds number. This makes it hard to quantify the wavelength for lower Reynolds numbers, because not all compression waves are visible. This would make the analysis very unreliable and therefore a more qualitative analysis is done.

In Figure 5.25, it is clearly visible that the distance between two compression waves is not constant. When traveling towards the ramp the distance grows, meaning that the wavelength is growing inside the shear layer. It is therefore not possible to find a constant wavelength. Looking at the frequency distribution in the shear layer might therefore be more interesting. This requires the velocity of the shear layer at every location which can be obtained with for example PIV. Doing a quick analysis based on the velocities obtained above, shows that the frequency of the waves is increasing from 20 kHz to 70 kHz towards the ramp, based on the following equation:

$$f = \frac{u_{cw}}{\lambda_{cw}} \tag{5.3}$$

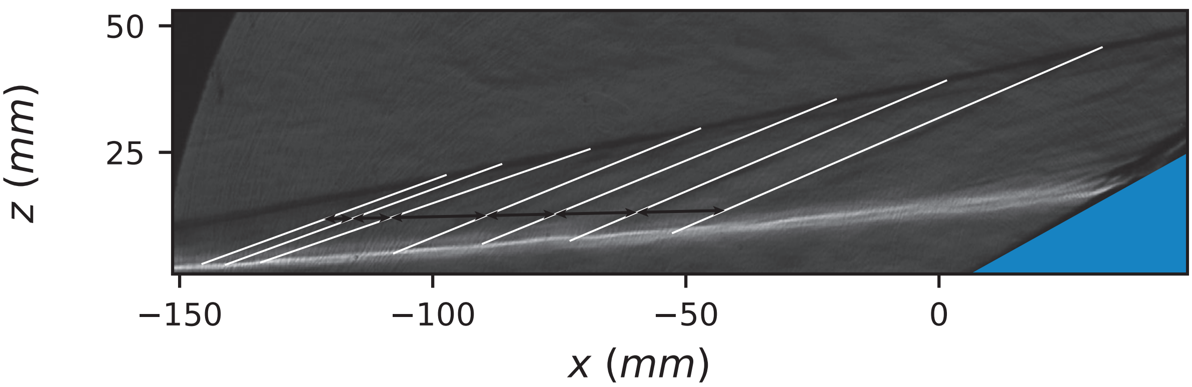

Figure 5.25: Compression wave angles of for the 30° ramp with $Re_L = 5.30 \cdot 10^6$.

Similarly, the growth rate is investigated using the standard deviation (STD) in time of the whole flow field. First, the effect of the Reynolds number on the STD field is investigated. Figures 5.27-5.29 show the STD fields for the 30° ramp at Reynolds number of respectively $1.67 \cdot 10^6$, $3.35 \cdot 10^6$ and $5.30 \cdot 10^6$. The STD limits of the figure are kept constant. The figures show that the STD values of the separation shock waves are reasonably constant, which means that the overall disturbances in the flow do not increase a lot with increasing Reynolds number. However, a considerable STD increase in the shear layer is found when increasing the Reynolds number. This effect is also slightly observed when increasing the compression ramp, but is considerably smaller. The STD fields for the other ramps are shown in Appendix B.3.

The cross sectional view of the STD field is used to determine the state of the boundary-layer. Figure 5.26 shows the expected cross sectional view of the STD for different boundary-layer states. Comparing the shear layers of Figures 5.27-5.29 shows that all shear layers have a higher STD on the edges compared to the middle. For the $Re_L = 1.67 \cdot 10^6$ this points at a laminar shear layer with very weak transitional structures in it. Furthermore, these structures are symmetrical. When increasing the Reynolds number these structure become larger and the STD grows. However, in the $Re_L = 5.30 \cdot 10^6$ case, the symmetry of the structures is not present at the beginning of the shear layer. At that location a very high STD is found at the bottom of the shear layer. This high STD value fades out into a symmetrical shear layer near the ramp. This can be due to the fact that the transitional structures form at the bottom of the shear layer and grow towards larger, more symmetrical structures when going towards the ramp.

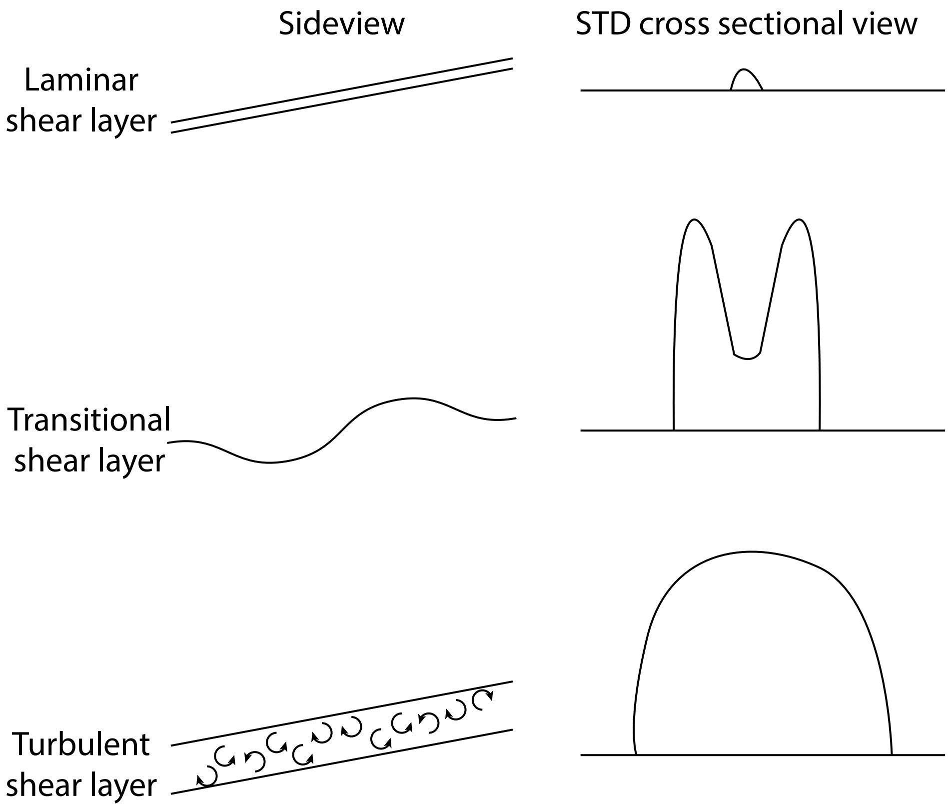

Figure 5.26: Sketch for the different STD cross sectional views.

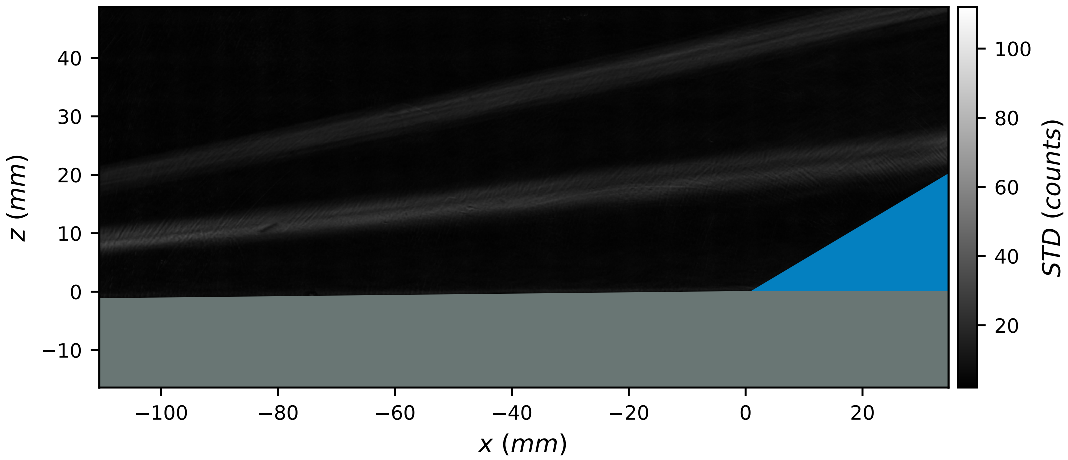

Figure 5.27: STD field for the 30° ramp with $Re_L = 1.67 \cdot 10^6$.

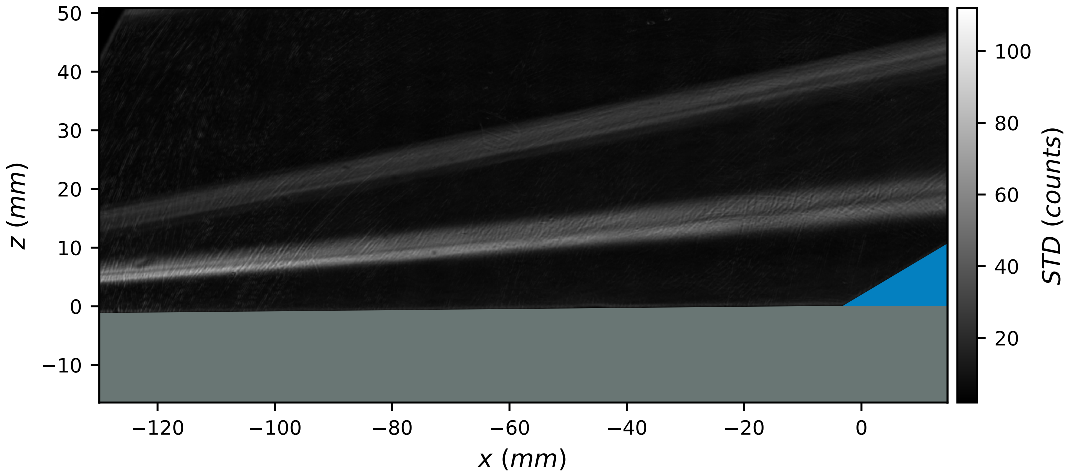

Figure 5.28: STD field for the 30° ramp with $Re_L = 3.35 \cdot 10^6$.

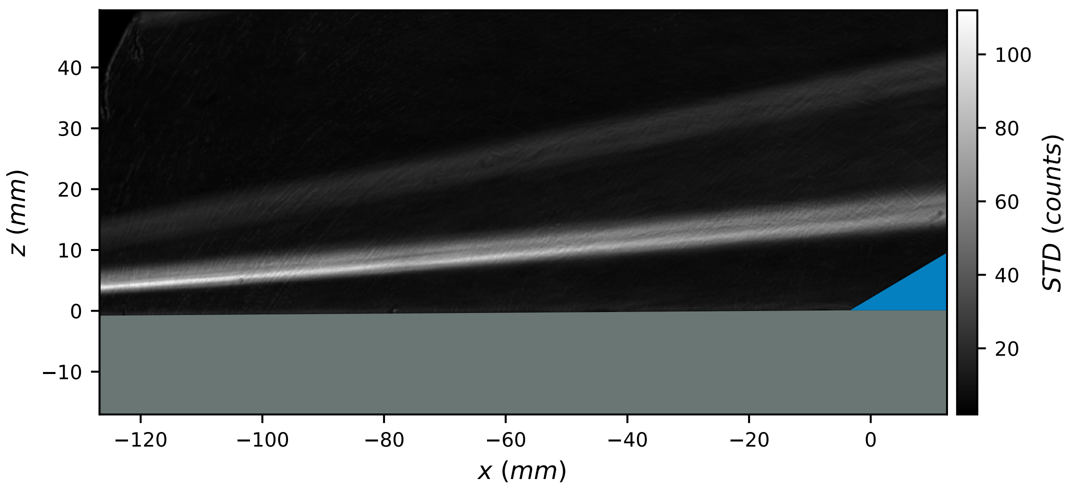

Figure 5.29: STD field for the 30° ramp with $Re_L = 5.30 \cdot 10^6$.

In order to take a closer look at the STD shape of the shear layer, a cross sectional profile is plotted at two different locations. The first line is at $x = -105\ mm$, the other line is at $x = -30\ mm$. For clarification, the lines and profiles are shown in Figures 5.30-5.32.

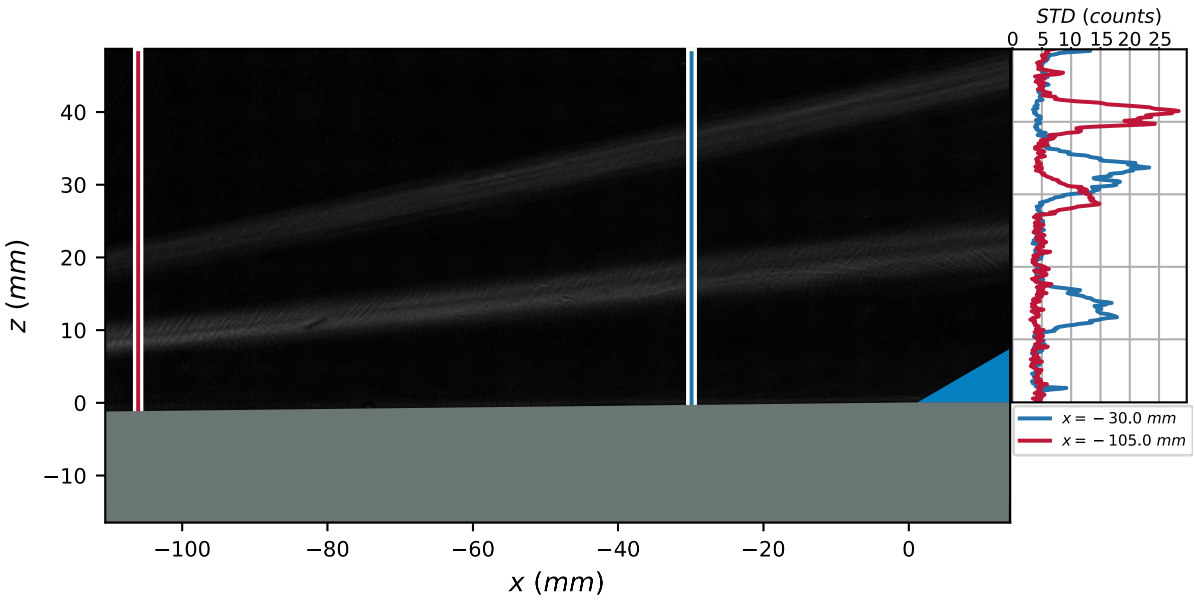

Figure 5.30: STD field for the 30° ramp with $Re_L = 1.67 \cdot 10^6$.

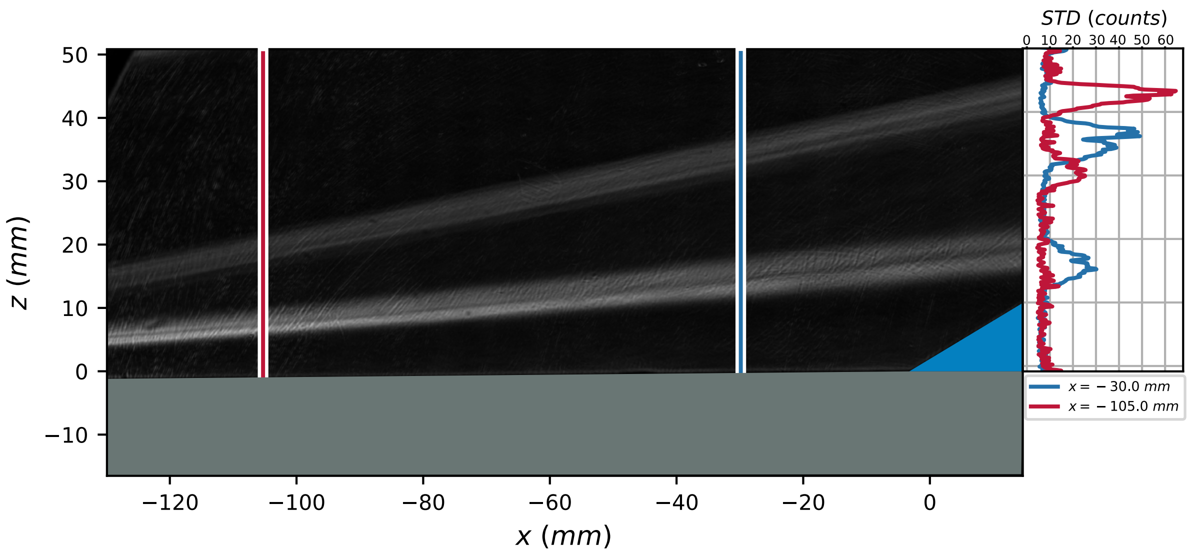

Figure 5.31: STD field for the 30° ramp with $Re_L = 3.35 \cdot 10^6$.

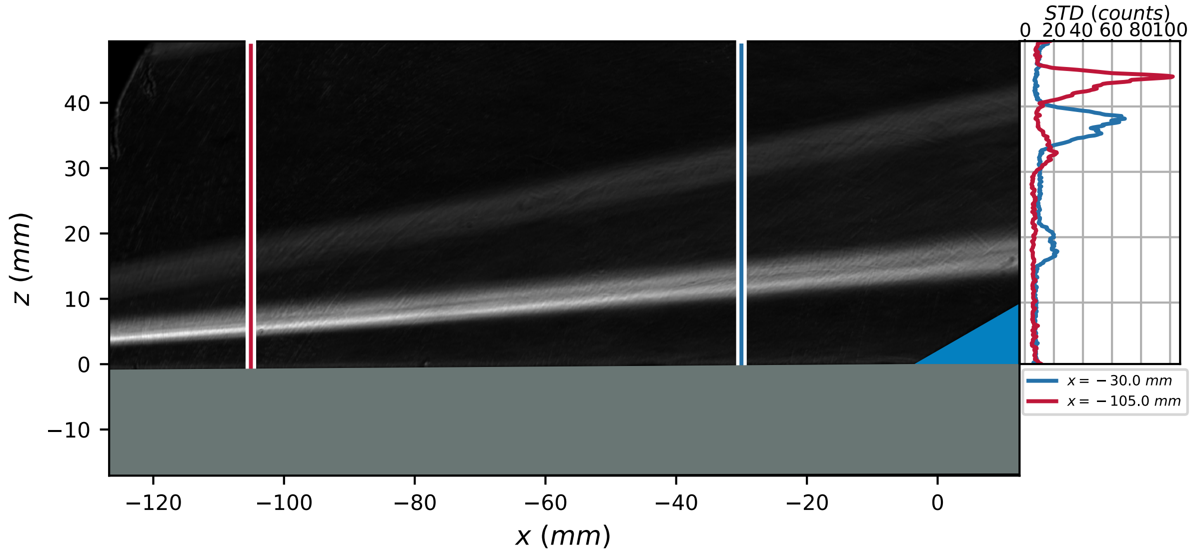

Figure 5.32: STD field for the 30° ramp with $Re_L = 5.30 \cdot 10^6$.

Figures 5.33-5.35 show the STD profiles rotated and zoomed in. The $Re_L = 1.67 \cdot 10^6$ case in Figure 5.33 shows that the maximum STD value at $x = -30$ mm is similar to the value of the shock wave. This means that the fluctuations in the shear layer are the same order than the fluctuations of the shock wave itself.

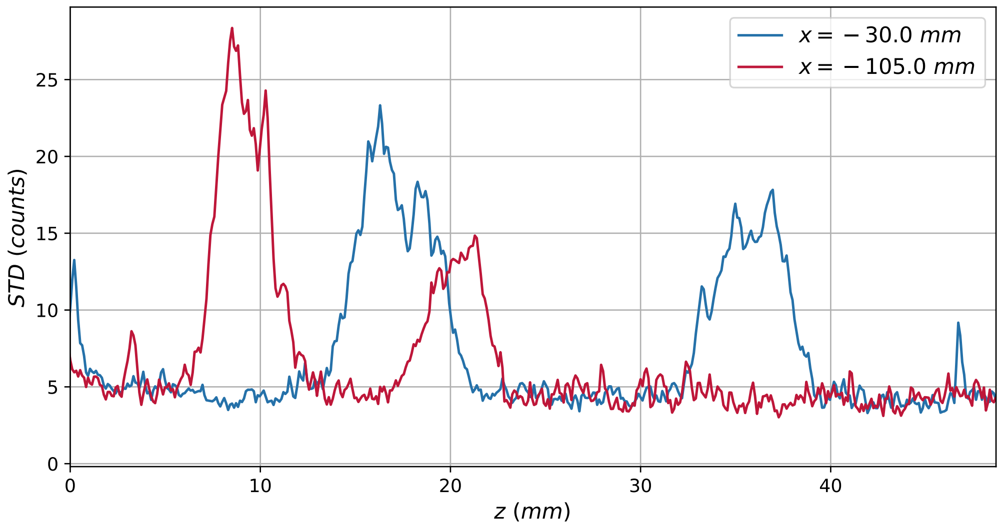

Figure 5.33: Slice of the STD field at the beginning of the shear layer and further downwards for the 30° ramp with $Re_L = 1.67 \cdot 10^6$.

Increasing the Reynolds number to the value in Figure 5.34 shows that the STD value is increasing compared to the shock wave. Also here it is visible that at $x = -105$ mm there is one high peak at the bottom of the shear layer ($z = 6.8$ mm) which lowers into two peaks at $x = -30$ mm ($z = 13.1$ and $z = 15.7$ mm).

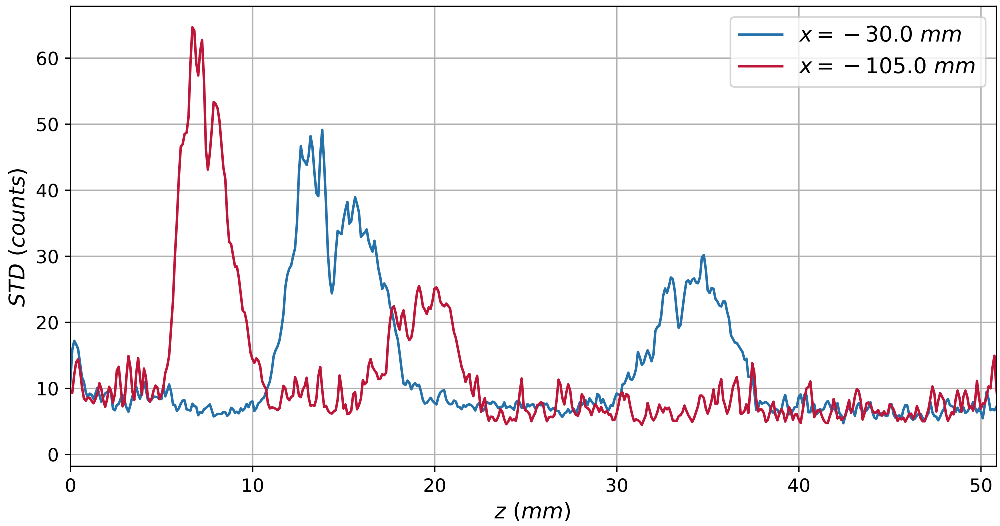

Figure 5.34: Slice of the STD field at the beginning of the shear layer and further downwards for the 30° ramp with $Re_L = 3.35 \cdot 10^6$.

In all cases it is observed that the width of the peak between $x = -105\ mm$ and $x = -30\ mm$ is strongly increased, meaning that the disturbances in the shear layer have become larger.

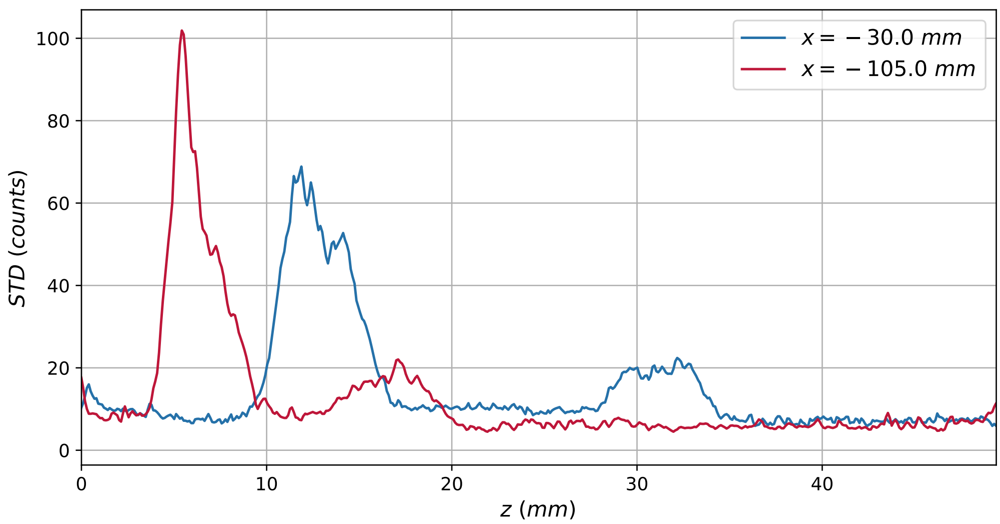

Figure 5.35: Slice of the STD field at the beginning of the shear layer and further downwards for the 30° ramp with $Re_L = 5.30 \cdot 10^6$.

The thickness of the peaks is measured with the method explained in Section 4.1.4 for every row of pixels. This gives the example in Figure 5.36.

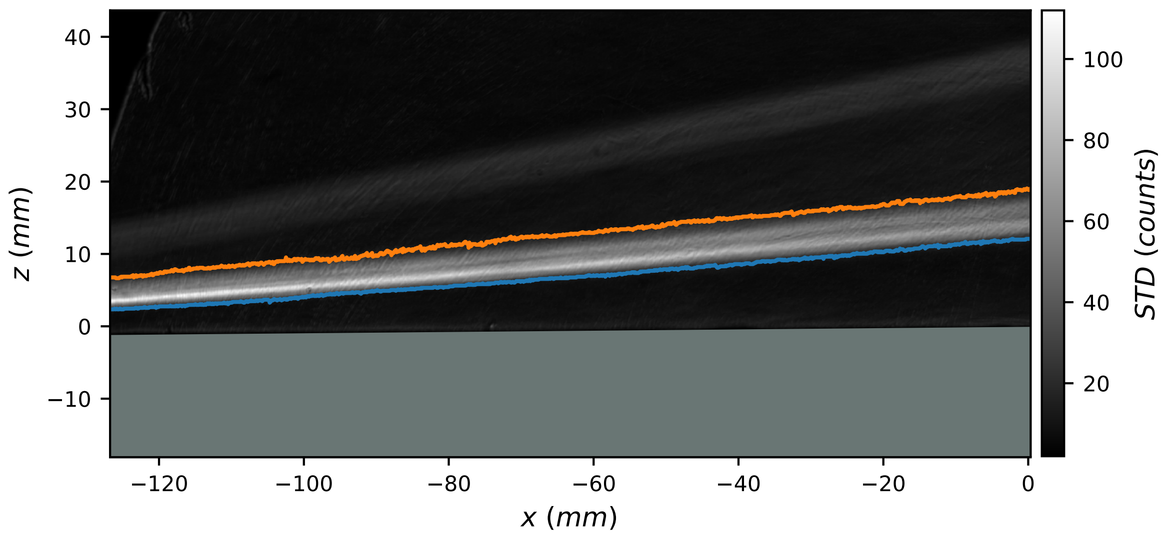

Figure 5.36: Example of a detected shear layer.

The width distribution of the region with increased fluctuations is plotted in Figure 5.37 for $Re_L = 5.30 \cdot 10^6$ and in Figure 5.38 for $Re_L = 4.46 \cdot 10^6$. The primary thing that is observed, is that both lines show an increasing thickness when moving in downstream direction. However, the $Re_L = 5.30 \cdot 10^6$ case starts to flatten near the ramp while for lower Reynolds numbers this behavior is not observed. A possible reason is, that the shear layer of the high Reynolds number is becoming turbulent which slows down the growth of the coherent transitional structures.

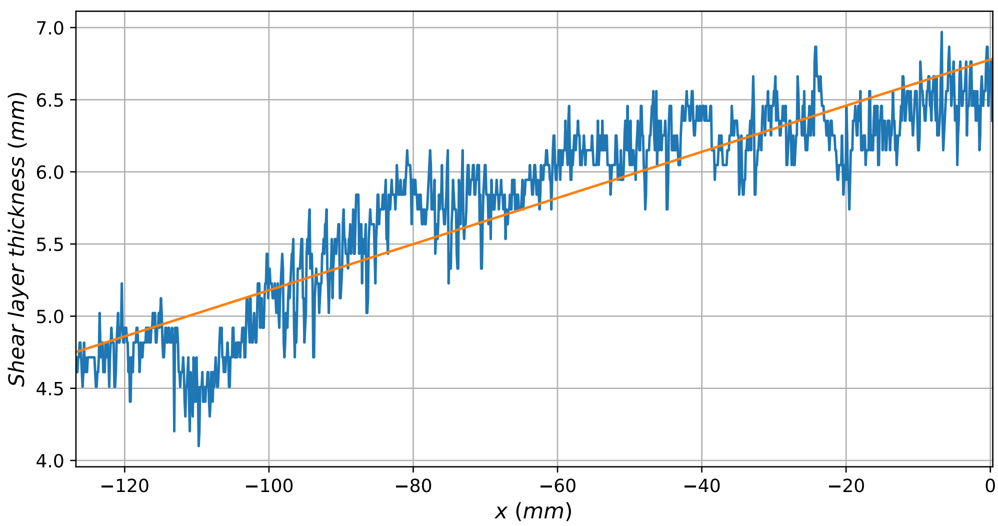

Figure 5.37: Shear layer thickness for the 30° ramp with $Re_L = 5.30 \cdot 10^6$.

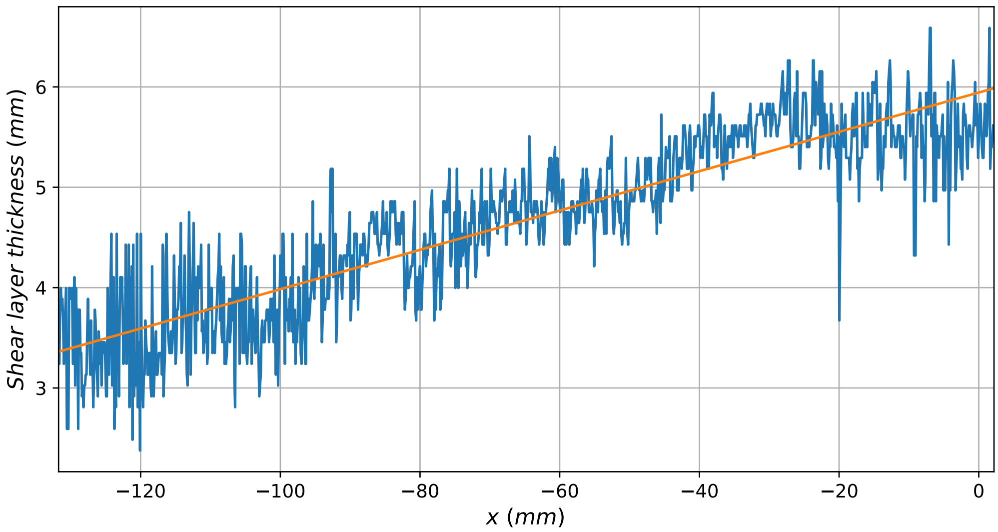

Figure 5.38: Shear layer thickness for the 30° ramp with $Re_L = 4.46 \cdot 10^6$.

The growth rate (σ) is then defined as the slope of the trendline (orange line) in Figures 5.37 and 5.38. This rough approximation gives the result in Figure 5.39. For both ramps an initial increase is found. For the 15° ramp the value is lower, probably because the shear layer is more laminar at the beginning. Due to the flattening of the growth rate near the end of the ramp for high Reynolds number, the average growth rate drops again when increasing the Reynolds number further.

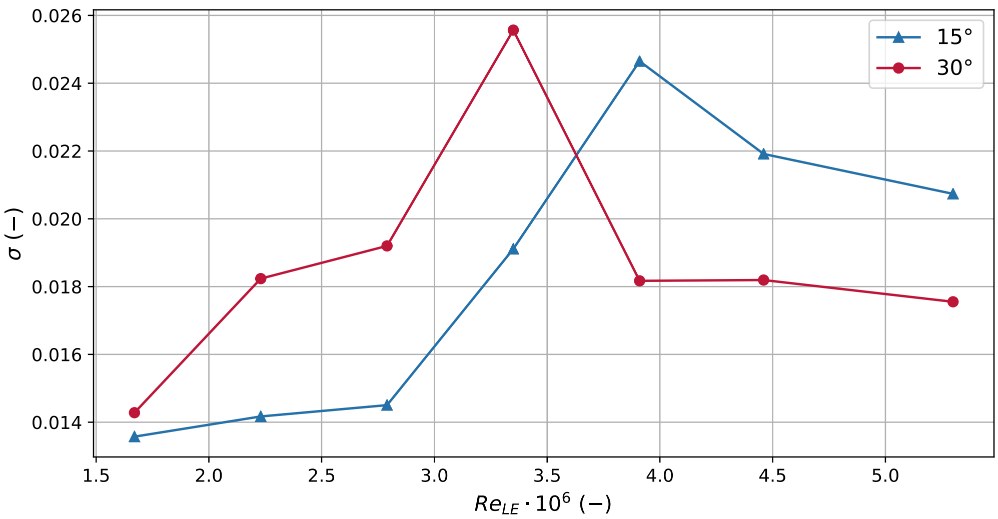

Figure 5.39: Growth rate (σ) for the 15° and 30° ramp as function of Reynolds number.

5.4. Uncertainties

This section explains the uncertainties that are present in the data. This is done for the errorbars presented in the data in Section 5.4.1. Furthermore, the conversion between pixel to millimeters is discussed in Section 5.4.2. At last, the uncertainty in the shear layer edge detection for the determination of the growth rate is discussed in Section 5.4.3.

5.4.1. Errorbars

As discussed in the beginning of the chapter, the errorbars in the figures are the minimum and maximum of the boxplot whiskers. Every frame of a run is a sample and multiple runs are combined. This means that in the errorbars both the repeatability of the wind tunnel and the repeatability of the flow are incorporated in the error margin. Furthermore, Figure 5.8 shows that the shock wave consists of two lines instead of one. The reason for this, is that Schlieren imaging projects the whole span on an image, meaning that 3D effects due to the finite span of the ramp are clearly visible. As a result an average is found over the span, which is also incorporated in the error bars shown in the figures.

5.4.2. Image Scaling

To convert the number of pixels to millimeters, a scaling factor has to be found in the image. Because the ramp is not always completely visible, it was opted to use the plate thickness at the ramp leading edge as reference. For every frame, the number of pixels of the plate is determined and divided by the theoretical value to get a scaling factor. This scaling factor is then averaged over one run.

This procedure introduces some uncertainties. One of the problems is, that a small reference length is used, meaning that a small detection error in pixels is exaggerated in millimeters. A detection error has two sources, one is that the plate is not correctly projected on the lens due to shadows. This makes the plate thicker on the image. The effect of this uncertainty is unknown. The second one, is that the plate is detected too late and the thickness in pixels will be too small. Looking at the data, it is found that the detection is off with a maximum of 6 pixels on a plate thickness of 180 pixels. This introduces an uncertainty of 3% in the scaling factor.

5.4.3. Shear Layer Edge Detection

In this section the uncertainty introduced by the detection method of the shear layer edge is discussed. Looking at Figure 5.38 it shows that around 20% of uncertainty is present looking at a x-location. However, the analysis uses the slope of the trendline, meaning that the uncertainty of the whole analysis is less than 20%. Because the trendline is found using least-squares it is not known how the slope is affected by the detection uncertainty.

6

QIRT Results

In this chapter the results obtained using Quantitative InfraRed Thermography (QIRT) are presented. First,a brief overview is given of the different features found in the QIRT images in Section 6.1. After that, a closer look is given to the peak Stanton numbers in Section 6.2. Next the spanwise streaks seen in Section 6.1 are discussed in Section 6.3. At last, a part is written about the uncertainties of the analysis in Section 6.4.

6.1. Compression Ramp Heat Flux Distribution

In Figure 6.1, an example is given of a heat flux field for the 30° ramp and a ramp leading edge Reynolds number of $Re_L = 5.30 \cdot 10^6$. In the image several flow features are distinguished. First of all, a line of high heat flux is visible in the middle of the ramp. From theory it is known that this location is very close to the shear layer reattachment point, also the largest heat fluxes are expected on this location. After the peak heat fluxes relaxation is seen.

Furthermore, in this region of high heat flux, spanwise streaks are observed. The streaks locally increase the heat flux to even higher values. These streaks are probably caused by the transitional structures inside the shear layer, also seen in Chapter 5.

The separation point of the shear layer is not observed, because the length of the shear layer is so large it falls upstream the field of view of the camera. The values in front of the ramp are therefore all in the separation bubble and are expected to be nearly constant because of the slow moving air.

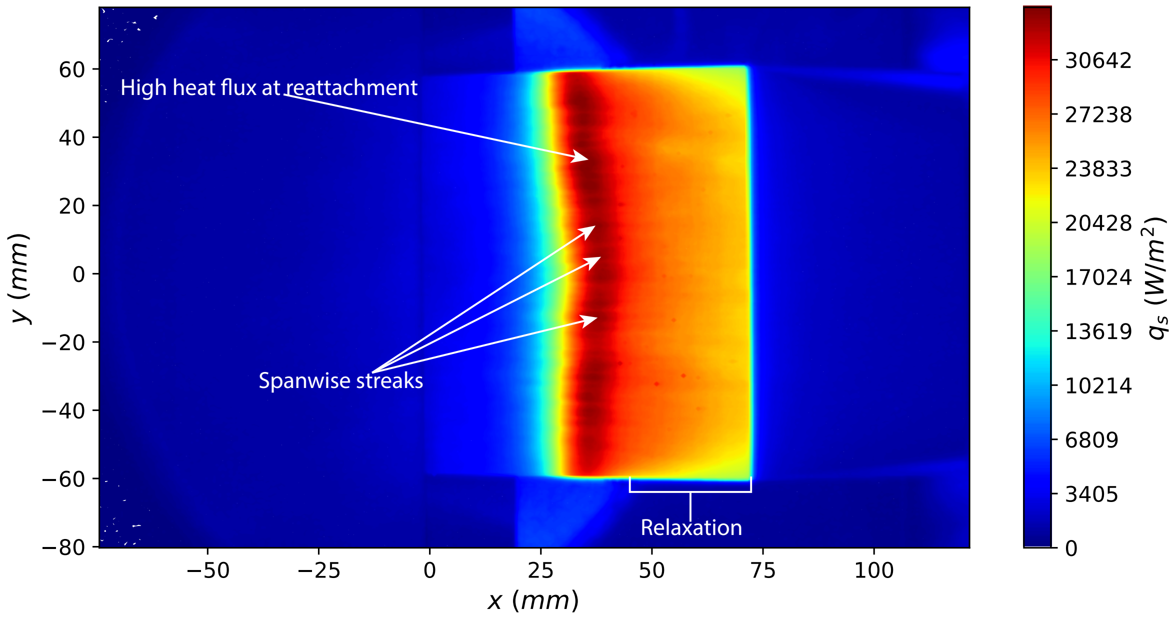

Figure 6.1: Example of a heat flux distribution for the 30° ramp and a leading edge Reynolds number of $Re_L = 5.30 \cdot 10^6$.

When the ramp is lowered to 15°, Figure 6.2 is obtained. The clear peak near reattachment is gone and is replaced by a constant, elevated heat flux after reattachment.

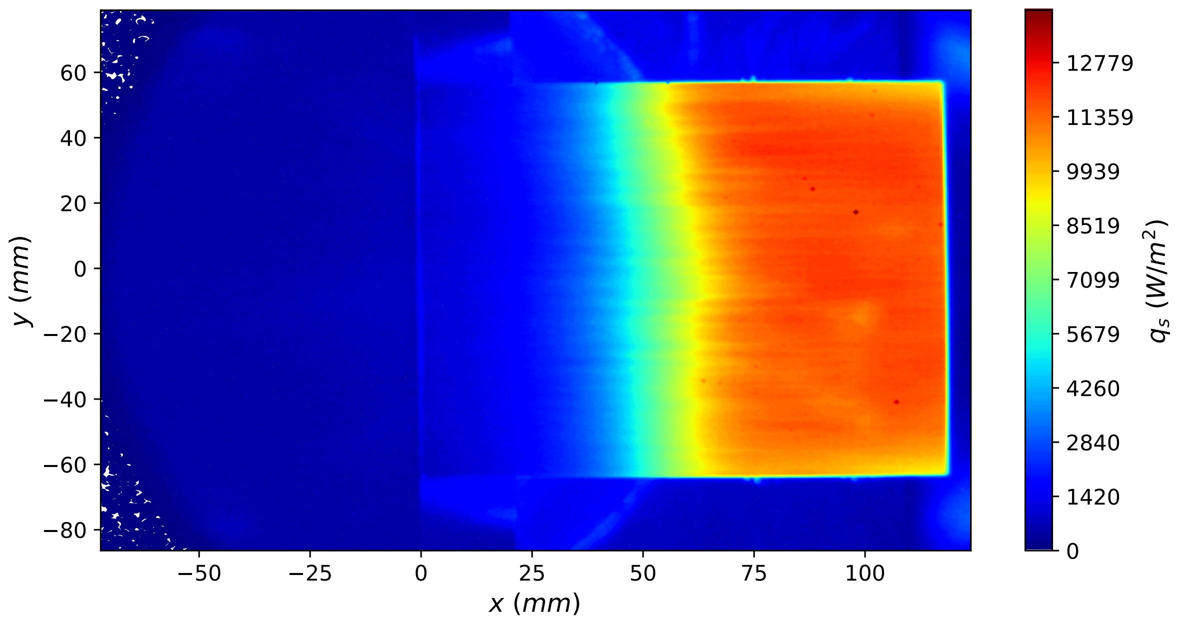

Figure 6.2: Heat flux distribution for the 15° ramp and a leading edge Reynolds number of $Re_L = 5.30 \cdot 10^6$.

The effect of the ramp angle is better seen when the heat flux over the center is plotted. The result is shown in Figure 6.3. In this case the Stanton number (c_h) is plotted instead of the heat flux. In the figure, the overshoot of the Stanton numbers and the relaxation afterwards are clearly observed for the higher ramp angles. As explained in Section 3.2, some ramps are flattened to reduce blocking of the wind tunnel. Unfortunately, the ramps are therefore too short to find the fully expanded values.

Comparing Figure 6.3 with Figure 2.14 shows very similar results with increasing heat flux peaks for an increasing ramp angle. Also, there is no peak for the 15° ramp in both figures. The streamwise profiles for other Reynolds numbers are shown in Appendix C.1 and show comparable results.

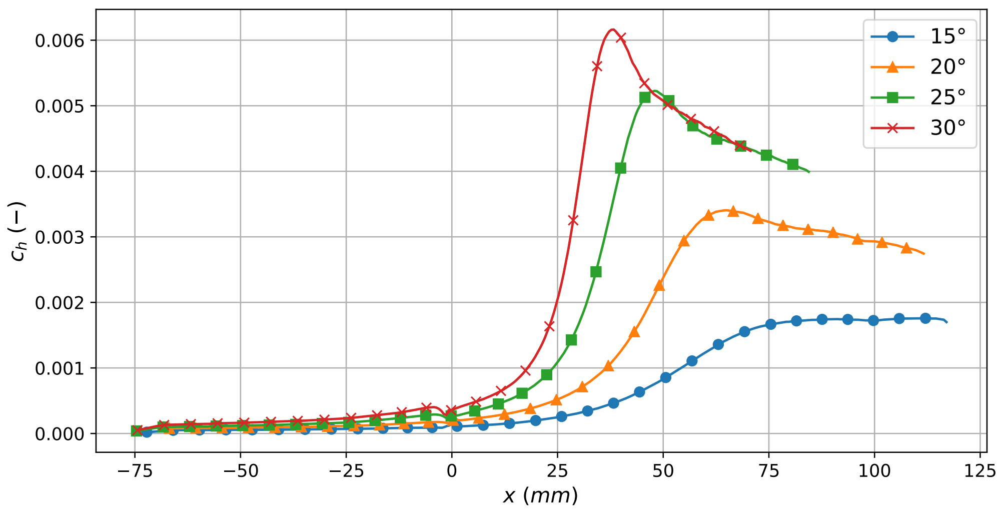

Figure 6.3: Streamwise Stanton numbers (c_h) as function of ramp angle at $Re_L = 5.30 \cdot 10^6$.

In Figure 6.4 the heat flux field is given for the same ramp as in Figure 6.1, but with a lower Reynolds number. In this figure the spanwise streaks in the reattachment region are more clear. Furthermore, the location of the reattachment has shifted aft, which is a result of the changed shear layer angle and shear layer length explained in Chapter 5. The effect of the Reynolds number on the magnitude of the peak heat flux is hard to see in this type of figure. A closer look at this is given in Section 6.2.

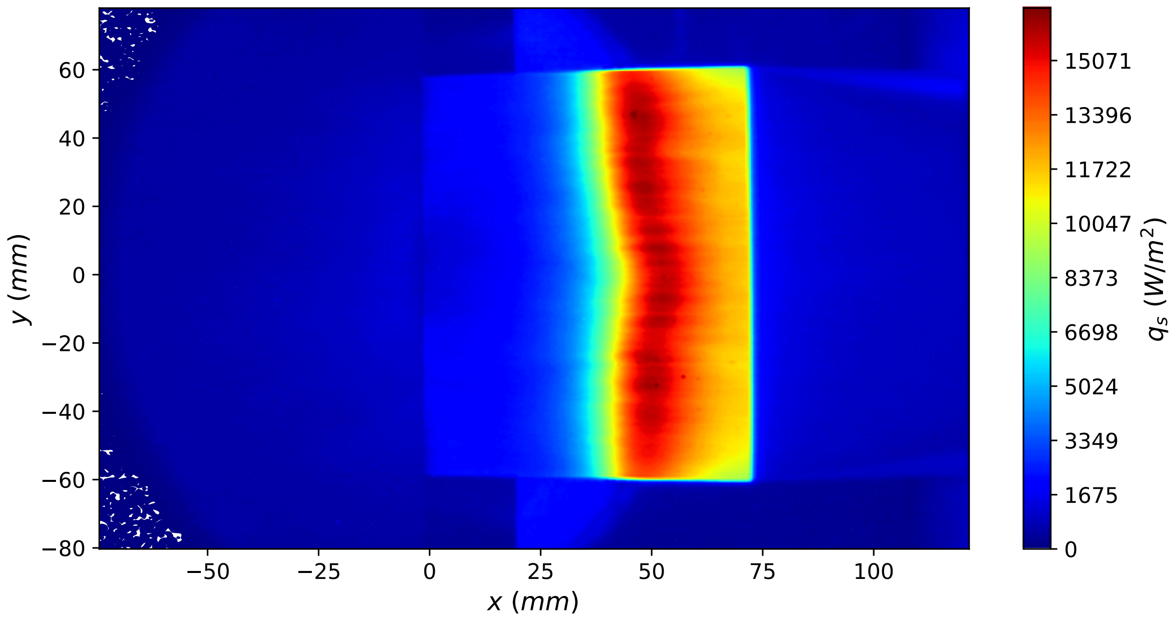

Figure 6.4: Heat flux distribution for the 30° ramp and a leading edge Reynolds number of $Re_L = 1.67 \cdot 10^6$.

6.2. Peak Heat Fluxes

This section focuses on the peak heat fluxes. In Chapter 2 it is explained that the peak heat fluxes can exceed the expected value with almost 36%. As a result, very high thermal loads are present at the peak heat flux location. This makes the reattachment location one of the hardest parts to design. A closer look at the behavior of the peak heat fluxes is given for different ramp angles and Reynolds numbers. Furthermore, the peak heating correlations from Section 2.5 are plotted against the experimental data to compare the results of the measurements and the correlations. The peak heat fluxes are obtained with the method explained in Section 4.3.5. The errorbars are the spreading of three wind tunnel runs at the same ramp and Reynolds number conditions.

Figure 6.5 shows the peak Stanton numbers for a leading edge Reynolds number of $Re_L = 1.67 \cdot 10^6$ and $Re_L = 5.30 \cdot 10^6$. Both lines show a near linear, trend in increasing peak Stanton number for an increasing ramp angle. In Appendix C.2 the same trend is also observed for other Reynolds numbers.

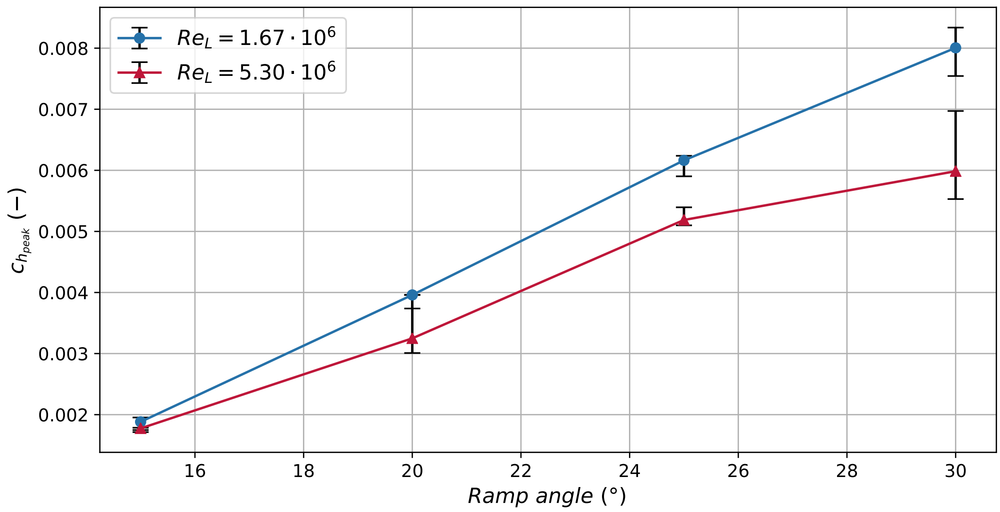

Figure 6.5: Peak Stanton numbers ($c_{h_{peak}}$) as function of ramp angle at $Re_L = 1.67 \cdot 10^6$ and $Re_L = 5.30 \cdot 10^6$.

The effect of the Reynolds number on the Stanton number for a given ramp angle is shown in Figures 6.6 and 6.9. For the 15° ramp the peak heat flux is decreasing with Reynolds numbers in between the range of $Re_L = 1.67 \cdot 10^6$ and $Re_L = 3.35 \cdot 10^6$, but in the error margin of the data. After $Re_L = 3.35 \cdot 10^6$, the peak heating is increasing again, before reaching a plateau at the highest Reynolds numbers. The reason for this, is that no overshoot is found in Figure 6.3, meaning that the peak Stanton number is close to the theoretical value of the heat flux behind an oblique shock wave.

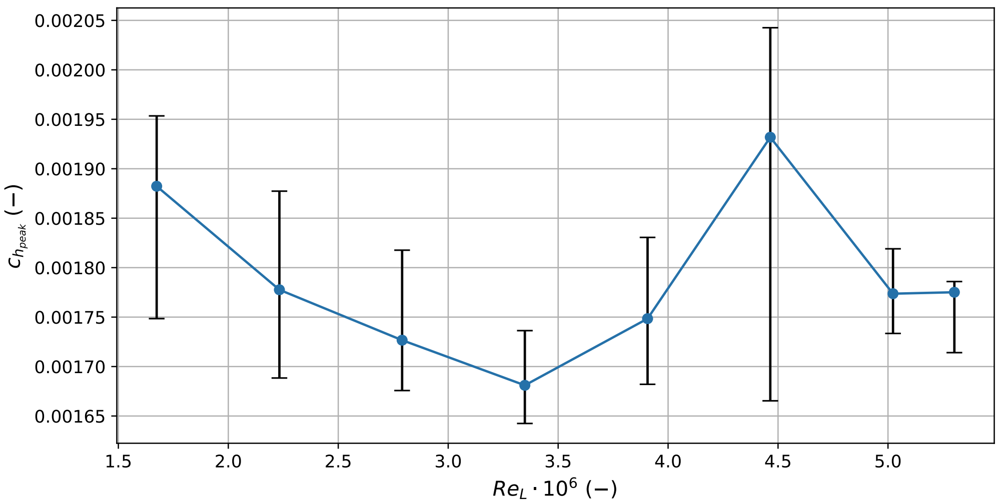

Figure 6.6: Peak Stanton numbers ($c_{h_{peak}}$) for the 15° ramp as function of Reynolds number.

For the higher ramp angle shown in Figure 6.7 and the other ramps in Figures 6.8 and 6.9, a reasonably constant trend is found between a Reynolds number of $Re_L = 1.67 \cdot 10^6$ and $Re_L = 3.91 \cdot 10^6$. But, when the Reynolds numbers get above $Re_L = 3.91 \cdot 10^6$ the peak heat flux is decreased.

As explained in Section 4.3.5, the peak heat fluxes are averaged over the second half of the run and ±25% of the span. This means, that the decrease of the heat flux at high Reynolds numbers cannot be attributed to the spanwise streaks. The effect of the spanwise streaks will be explained in Section 6.3. So these figures show whether the state of shear layer or shear layer thickness have an effect on the mean heat flux at reattachment. As said, the overall effect is small, but for high Reynolds numbers it gets lower. A potential reason for this, is that the shear layer is starting to get turbulent and therefore lowers the peak heat flux.

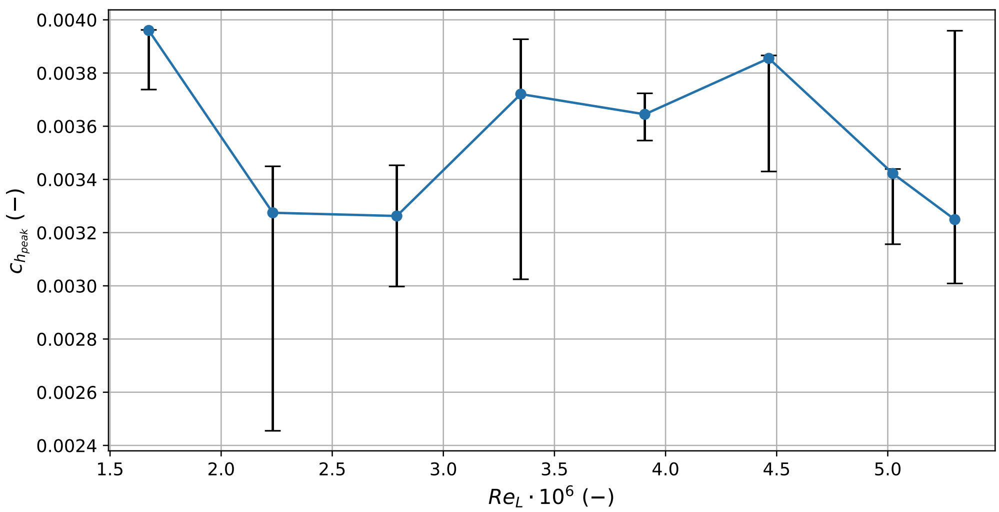

Figure 6.7: Peak Stanton numbers ($c_{h_{peak}}$) for the 20° ramp as function of Reynolds number.

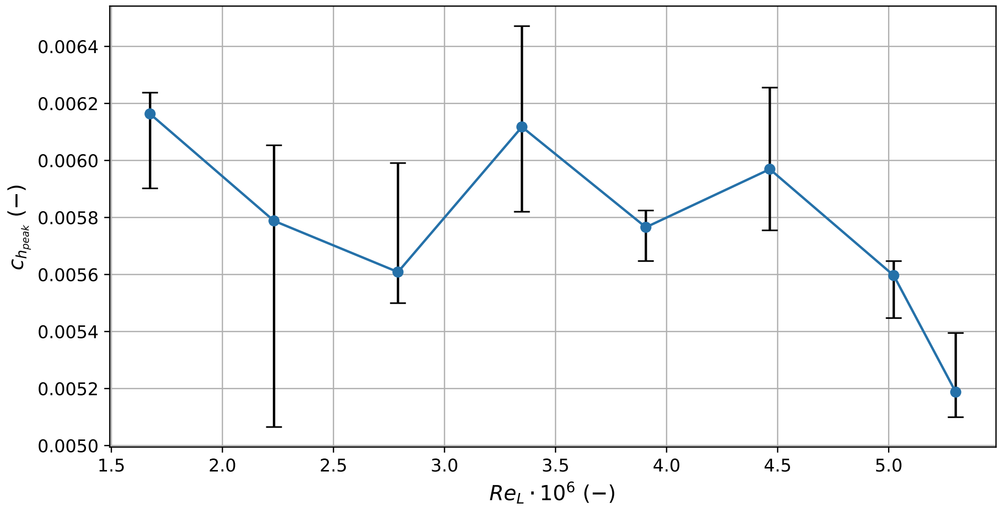

Figure 6.8: Peak Stanton numbers ($c_{h_{peak}}$) for the 25° ramp as function of Reynolds number.

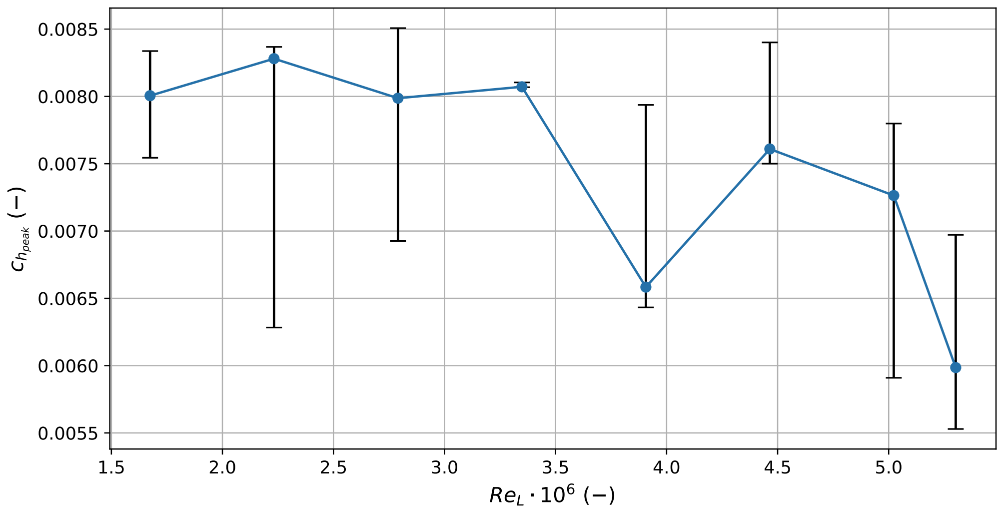

Figure 6.9: Peak Stanton numbers ($c_{h_{peak}}$) for the 30° ramp as function of Reynolds number.

In Section 2.5, correlations between the peak Stanton number and Stanton number at the interaction onset location (c_{h_0}) are given. In order to validate these equations, the Stanton number at the interaction onset location has to be known. This is done using the reference temperature method of Section 2.2.1 and the location of the interaction onset (x_0) is found using the shear layer data from the Schlieren measurements. These are then converted with Figure 6.10 and the following equations:

$$\alpha = 180° - \left(180° - \varphi\right) - \varphi_{SL} - 1° = \varphi - \varphi_{SL} - 1° \tag{6.1}$$

$$x_{sep} = \frac{\sin\alpha}{\sin 180° - \varphi} L_{sep} \tag{6.2}$$

$$x_0 = x_{LE} - x_{sep} \tag{6.3}$$

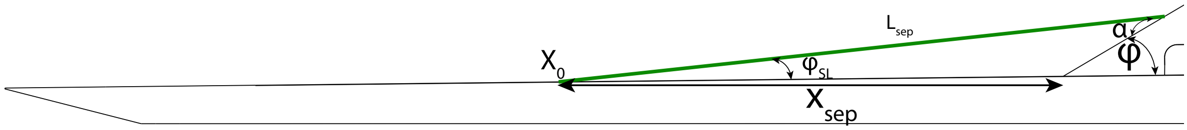

Figure 6.10: Schematic view of the x_0 calculation.

Figure 6.11 shows the correlations of Equations 2.30-2.32 together with the experimental data. It shows that both the turbulent and transitional correlation lie very close to each other. This is the result of the used correlation data to make this correlation. At this Reynolds number the transitional heat fluxes are close to the turbulent heat fluxes. However, the reason for the elevated value compared to the laminar correlation is different. The transitional heat fluxes come from coherent structures inside the laminar shear layer that elevate the heat flux and the turbulent heat fluxes from the turbulent shear layer.

The measured data lies above the correlations, which means that the transitional structures seen with the Schlieren imaging are stronger than the correlation predicts. Also the flow is not yet turbulent.

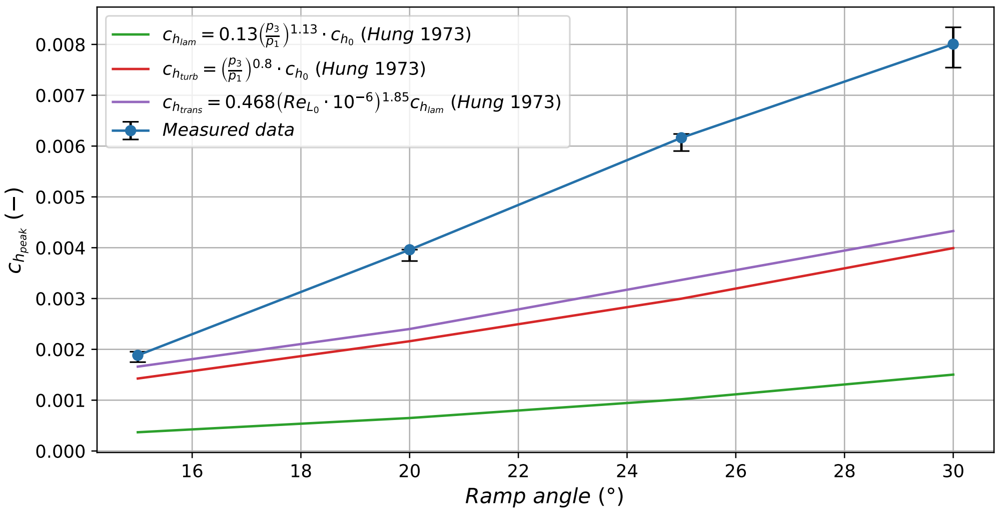

Figure 6.11: Peak Stanton numbers ($c_{h_{peak}}$) as function of ramp angle at $Re_L = 1.67 \cdot 10^6$.

At the Reynolds numbers of $Re_L = 2.23 \cdot 10^6$ and $Re_L = 2.79 \cdot 10^6$ as stated in Figures 6.12 and 6.12, the transitional correlation is very close to the measured data.

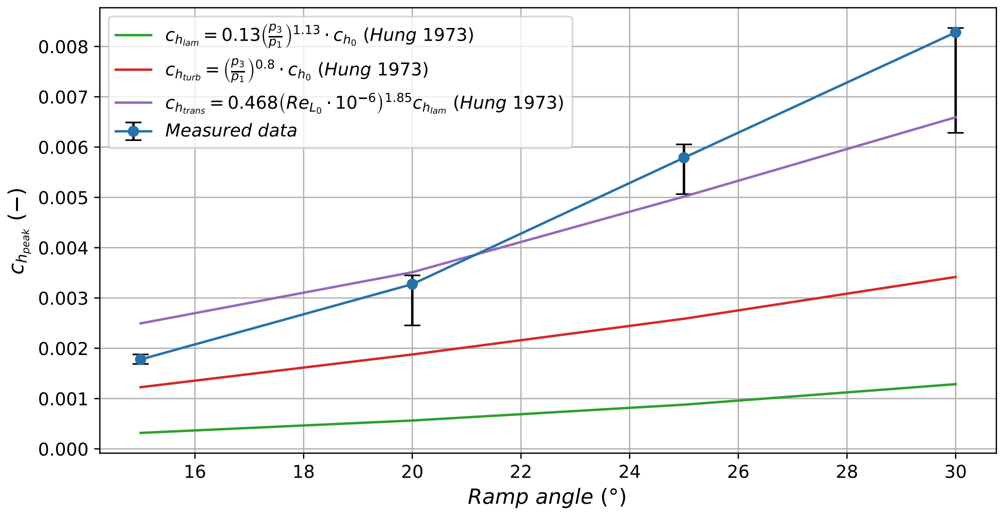

Figure 6.12: Peak Stanton numbers ($c_{h_{peak}}$) as function of ramp angle at $Re_L = 2.23 \cdot 10^6$.

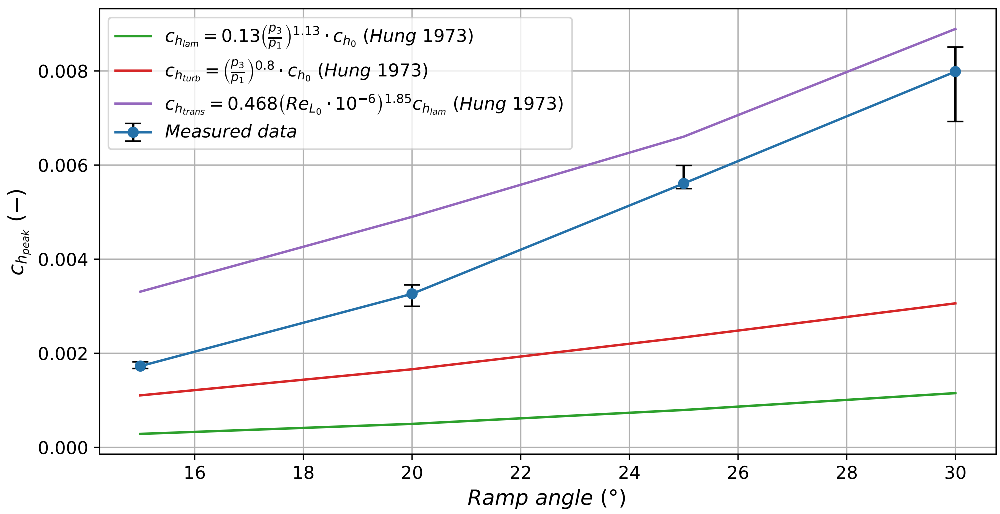

Figure 6.13: Peak Stanton numbers ($c_{h_{peak}}$) as function of ramp angle at $Re_L = 2.79 \cdot 10^6$.

Increasing the Reynolds number further to $Re_L = 2.79 \cdot 10^6$, results in the correlation for transition completely overestimating the peak Stanton numbers and lying closer to the turbulent correlation. This can be seen more clearly in Figure 6.15. At this Reynolds number, the shear layer is almost turbulent near reattachment as is seen in the Schlieren measurements. This result is in line with the correlations, the shear layer is not fully turbulent but is getting closer to it.

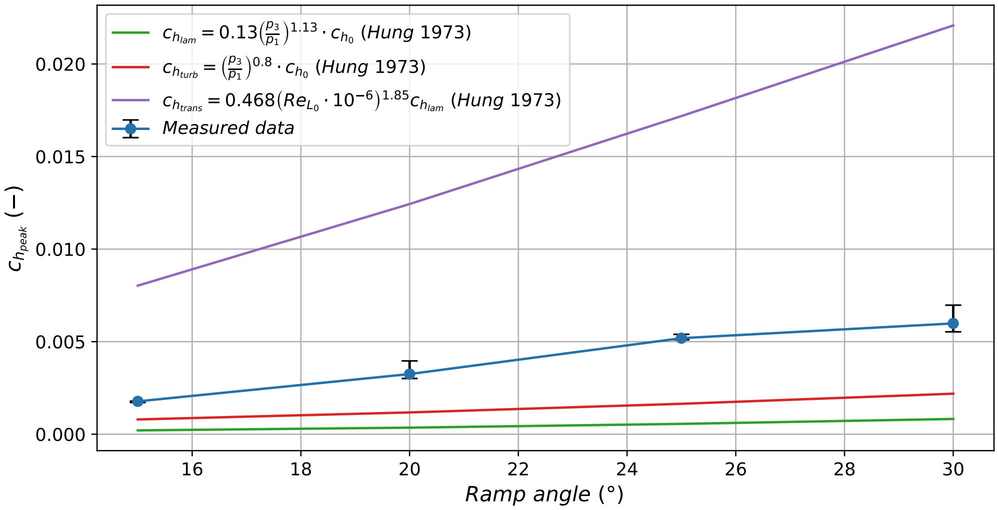

Figure 6.14: Peak Stanton numbers ($c_{h_{peak}}$) as function of ramp angle at $Re_L = 5.30 \cdot 10^6$.

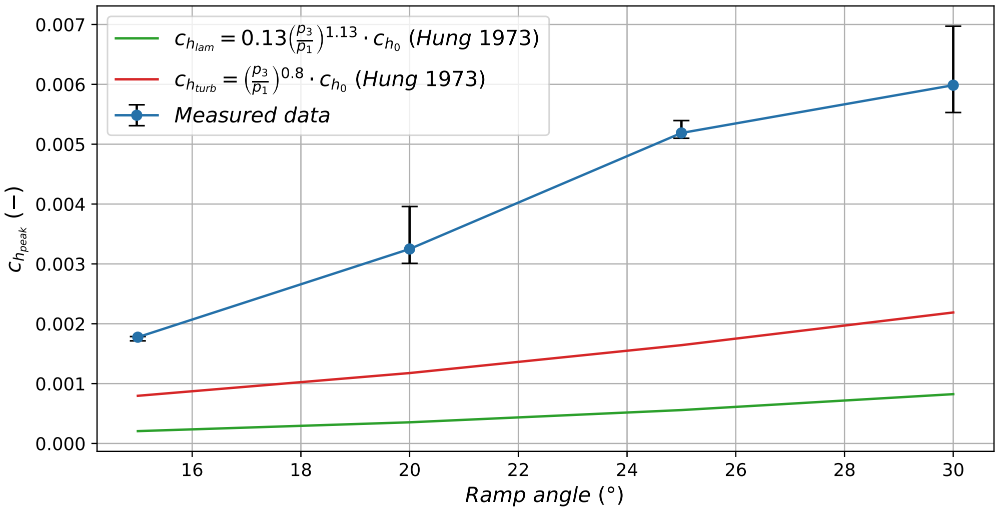

Figure 6.15: Peak Stanton numbers ($c_{h_{peak}}$) as function of ramp angle at $Re_L = 5.30 \cdot 10^6$.

6.3. Spanwise Waves

As seen in Figure 6.1, there are spanwise streaks present in the heat flux. It is known that these spanwise streaks can further increase the already high peak heat fluxes near the reattachment location. It is therefore very important to have proper knowledge on how transitional structures influence the heat flux.

For the analysis, the data is first corrected for the spanwise effects due to the geometry of the ramp, as explained in Section 4.3.5. Furthermore, the spanwise data just before and after the reattachment location is used to determine the spanwise wavelength. The errorbars present in the plot are then the minimum and maximum of boxplot whiskers.

Figure 6.16 shows the spanwise variation of the Stanton number near the peak heating region for the 15° ramp. In the figure it is clear that indeed spanwise waves are present. For the 30° ramp, the result in Figure 6.17 is found. Besides the waves with a small wavelength found for the 15° ramp, waves with a larger wavelength have formed.

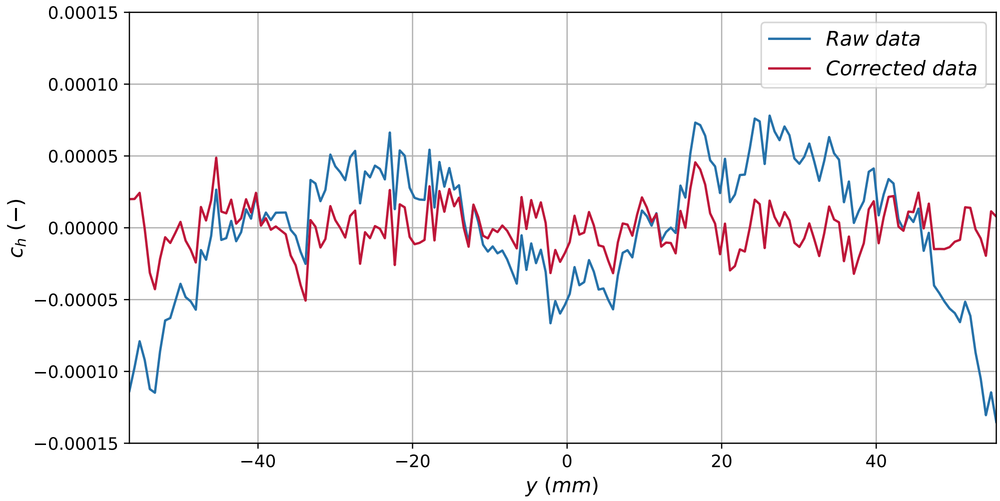

Figure 6.16: Spanwise Stanton numbers ($c_h - c_{h_{mean}}$) for the 15° ramp and $Re_L = 1.67 \cdot 10^6$.

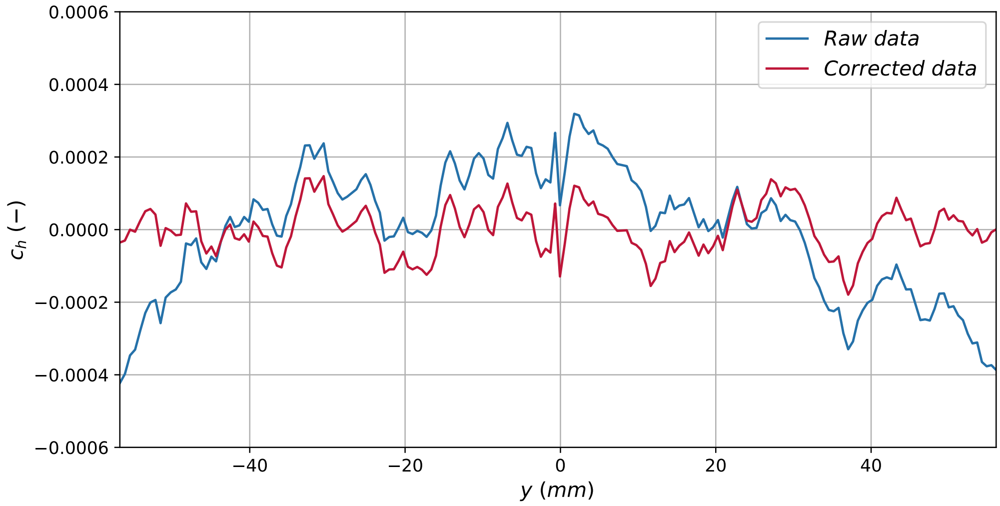

Figure 6.17: Spanwise Stanton numbers ($c_h - c_{h_{mean}}$) for the 30° ramp and $Re_L = 1.67 \cdot 10^6$.

When the Reynolds number is increased further to $Re_L = 5.30 \cdot 10^6$, the results in Figures 6.18 and 6.19 are found for respectively the 15° ramp and 30° ramp. Comparing it with the lower Reynolds number case, it shows that also for the 15° the wave with a large wavelength have formed. This shows that the amplitude of these waves is dependent on the Reynolds number.

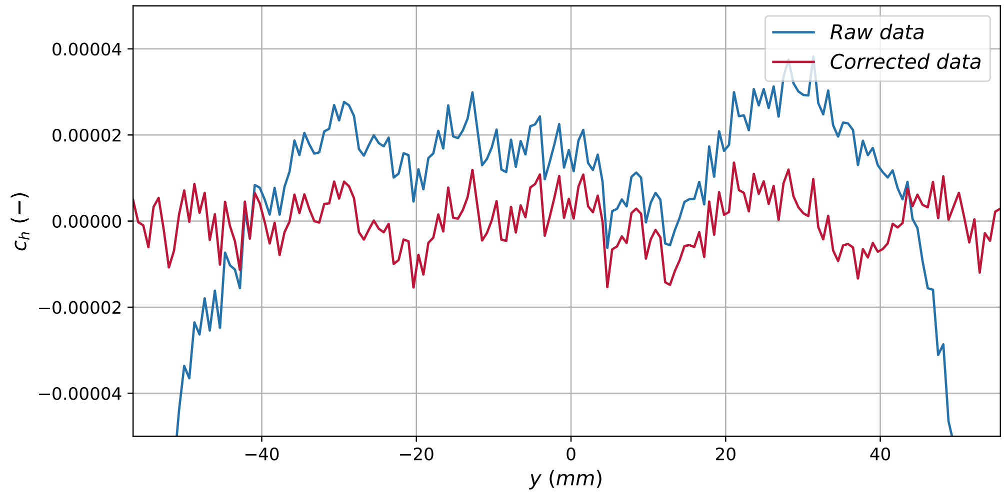

Figure 6.18: Spanwise Stanton numbers ($c_h - c_{h_{mean}}$) for the 15° ramp and $Re_L = 5.30 \cdot 10^6$.

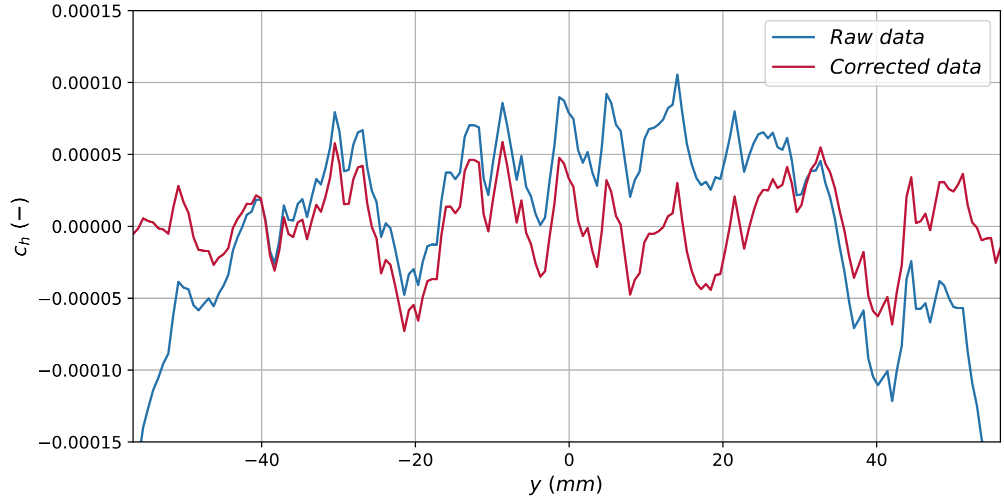

Figure 6.19: Spanwise Stanton numbers ($c_h - c_{h_{mean}}$) for the 30° ramp and $Re_L = 5.30 \cdot 10^6$.

To have a closer look at how many waves are present for both types of waves and how they are affected by the Reynolds number and ramp angle, a Fast Fourier Transform (FFT) is performed on the signal. This results in Figure 6.20, in this case only half of the domain is shown. In this figure, two peaks are observed between 3 and 5, which coincides with the large wavelength waves. The small wavelength waves are harder to find in the frequency spectrum because the energy content is less, therefore a relative peak has to be found. Looking in the figure this gives a peak at 15.

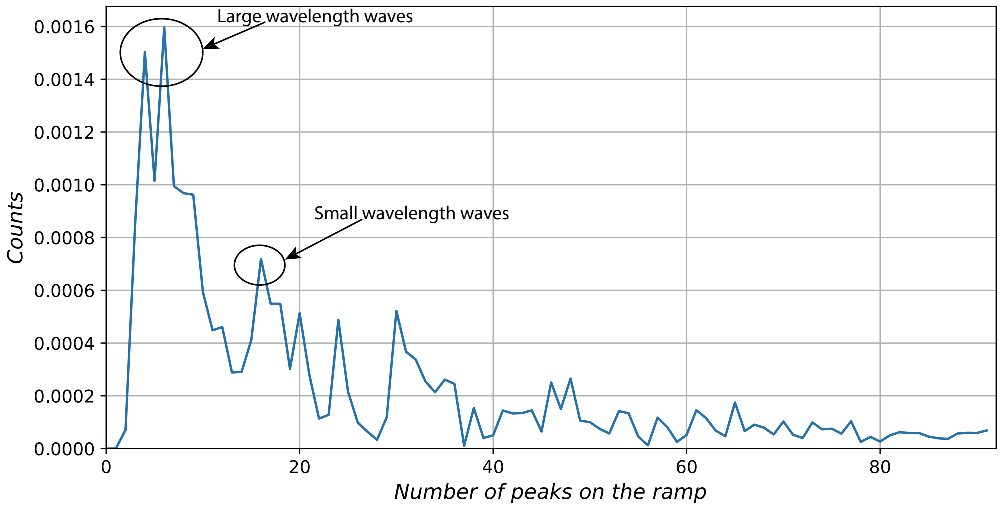

Figure 6.20: FFT of the spanwise Stanton number distribution for 30° ramp and $Re_L = 5.30 \cdot 10^6$.

The results for the large wavelength waves are shown in Figure 6.21 and 6.22. The wavelength is normalized using the method in Section 4.3.5. For the 15° ramp the non-dimensional wavelength for the lowest Reynolds number has such a large error that it cannot be used to draw conclusions from. For the Reynolds number range between $Re_L = 2.23 \cdot 10^6$ and $Re_L = 5.30 \cdot 10^6$ a decrease in wavelength is found. The reason for the spreading at the low Reynolds numbers is that the large wavelength waves are still very small as shown in Figure 6.16. When the magnitude grows, they are better grasped by the FFT.

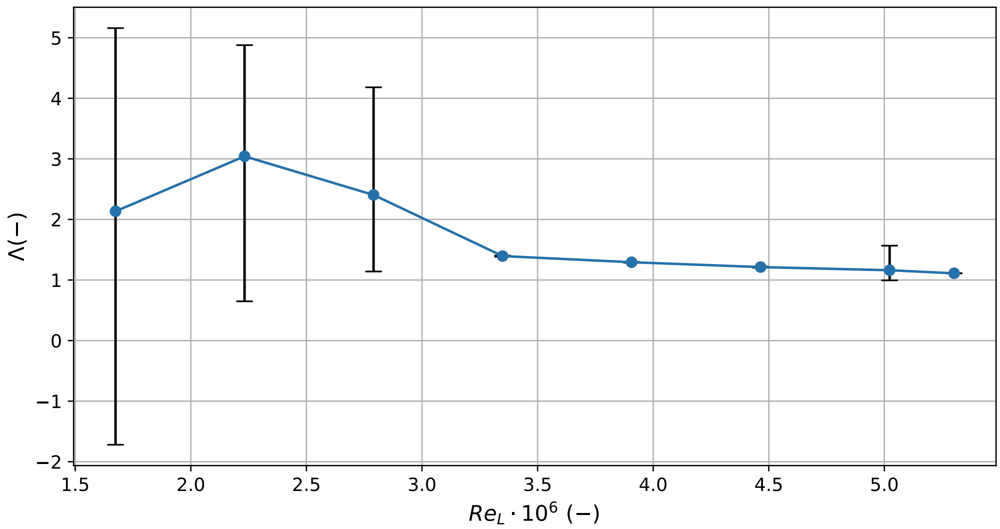

Figure 6.21: Non-dimensional wavelength (Λ) for the large wavelength waves for the 15° ramp as function of Reynolds number.

For the 30°, larger uncertainties are found compared to the 15° ramp, but a clear decrease in wavelength is found for increasing Reynolds number. In Appendix C.3 the other ramp angles are shown, also in this data the same trend is found.

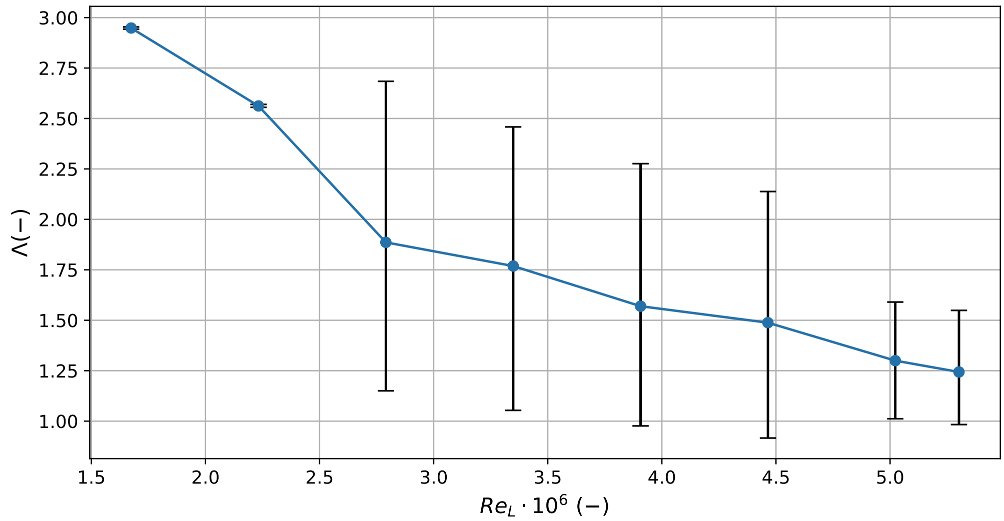

Figure 6.22: Non-dimensional wavelength (Λ) for the large wavelength waves for the 30° ramp as function of Reynolds number.

The dimensionless wavelength for small wavelength waves found on the ramp is shown in Figure 6.23 and 6.24 for the 15° and 30° ramp. Also for the small wavelength waves a decreasing trend for increasing Reynolds number is found when looking at the mean. But, also in this case there is a large spread found in the data.

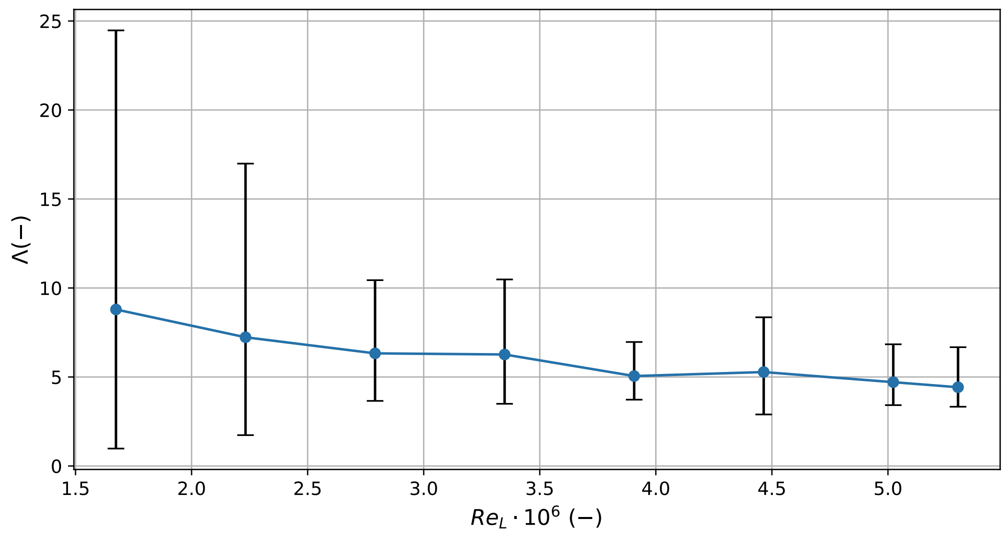

Figure 6.23: Non-dimensional wavelength (Λ) for the small wavelength waves for the 15° ramp as function of Reynolds number.

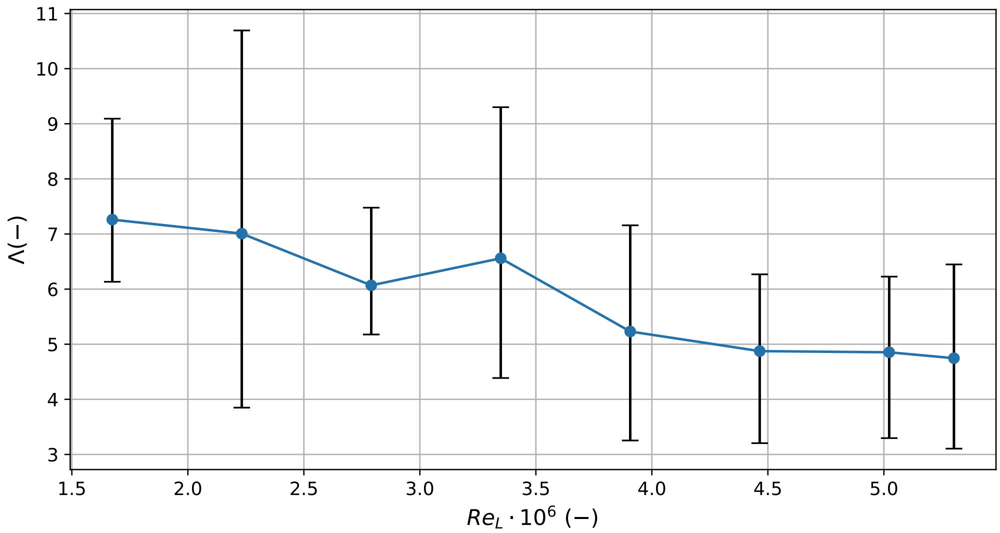

Figure 6.24: Non-dimensional wavelength (Λ) for the small wavelength waves for the 30° ramp as function of Reynolds number.

To conclude, a decreasing non-dimensional wavelength is found when increasing the Reynolds number for both types of waves. There is no relation found between the non-dimensional wavelength and ramp angle. Comparing the results with literature, shows that this is not completely in line with results in [23] and [24]. In those papers a slight reduction in dimensional wavelength with increasing ramp angle is found in this case of Görtler waves. A reason for this discrepenacy is, that the error margin of the method used in this report is considerable larger than the trend found in the literature. Another option is that the waves in the shear layer are not of the Görtler type.

Furthermore, [24] found an increasing dimensional wavelength for increasing Reynolds number. Converting these values to non-dimension wavelengths with the method explained in Section 4.3.5 shows that there is not a coherent relation found between the non-dimensional wavelength and Reynolds number. However, it should be noted that the Reynolds number range of [24] is lower than these experiments.

6.4. Uncertainties

This section briefly describes the uncertainties that are present in the data. This is done for the errorbars presented in the data in Section 6.4.1. The mapping of the data to physical coordinates is treated in Section 6.4.2. Furthermore, the noise of the camera is shortly discussed in Section 6.4.3.

6.4.1. Errorbars

In the data, errorbars are shown that describe the spreading of the data. In all the data, except the data for the spanwise waves, this spreading is based on the three runs that are performed per data point. So no statistical analysis is performed on the data, because there are only three data points. For the spanwise waves data a larger dataset is obtained, so the errorbars are different. In that case the errorbars represent the min, max whiskers of a boxplot, just as is done in Chapter 5.

6.4.2. Coordinate Mapping

For the mapping there are also some uncertainties present. These consist of two things, one is that a 1D interpolation is used. The second one is the hole determination. As stated in Chapter 4, the x- and y-coordinates are interpolated separately. This means that not the whole field is interpolated, but only two lines. As a result, drifting away from the interpolation lines means that an error is introduced. The interpolation lines are chosen near the reattachment region and on the centerline. As these locations are only used for the data presented in the plots, the error will be in the order of the truncation error of the interpolation scheme. Far away from the lines some drifting of a maximum of 5 px is observed, this creates an error of around 3 mm or 2.6% of the ramp width. As this offset is only present in the contour plots, which are used only for visual purposes, this is deemed to be acceptable.

Another error is introduced by detecting the holes of the plates in the heat flux images. The holes itself have a diameter of 5 px and are easily detected. The middle of the hole is then detected with a maximum accuracy of 0.5 px which introduces a maximum error of 0.3mm.

6.4.3. Camera Noise

The noise level of the camera is shown in Figure 6.25 on the same location as the reattachment location during a run. The noise level on the Stanton number is around ±0.000005. The smallest Stanton number used in the data, is that of the small spanwise waves which have a magnitude of 0.00005. This means that the signal to noise level is around 10.

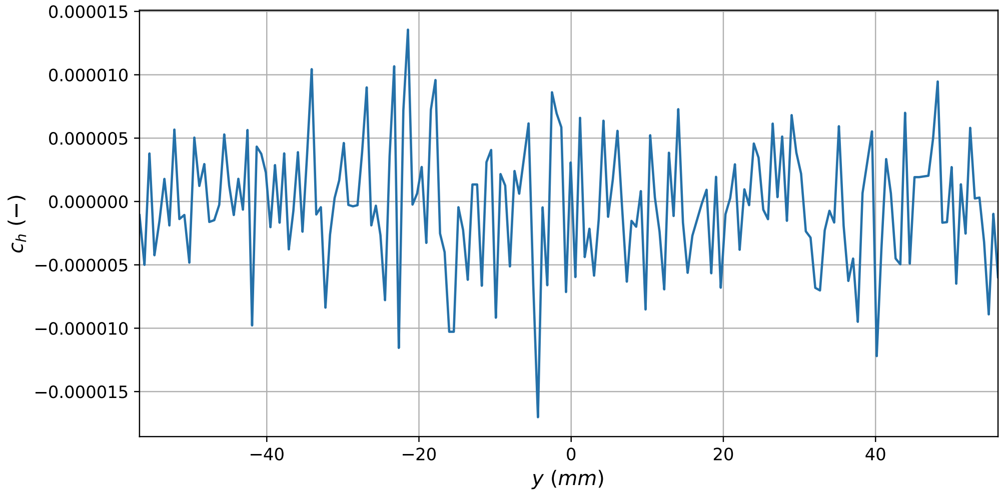

Figure 6.25: Noise level of the camera.

7

BOS Results

In this chapter the results of the BOS measurement campaign are presented. As the results were not as expected, this chapter is build up in a different way than the previous sections. First the motion of model is explained in Section 7.1. Then the choice of the camera settings and how they influence the results are discussed in Section 7.2. After that, shock generators are treated in Section 7.3. At last, a discussion is given about the correlation method in Section 7.4.

7.1. Model Motion

In Figure 7.1, the displacement of a point on the flat plate is given as function of time. What is noticed, is that a large sinusoidal shape is found. This motion is attributed to the movement of the model during the run. One of the reasons for this, is the shape of the displacement. The sinusoidal shape is characteristic for solid body movement (spring). Furthermore, the motion is hardly affected by the focal point at a constant speckle size. This also confirms that the motion is due to the movement of the model. If the motion was caused by a density change, a difference lens should have had an effect, as is seen in Equation 4.3.

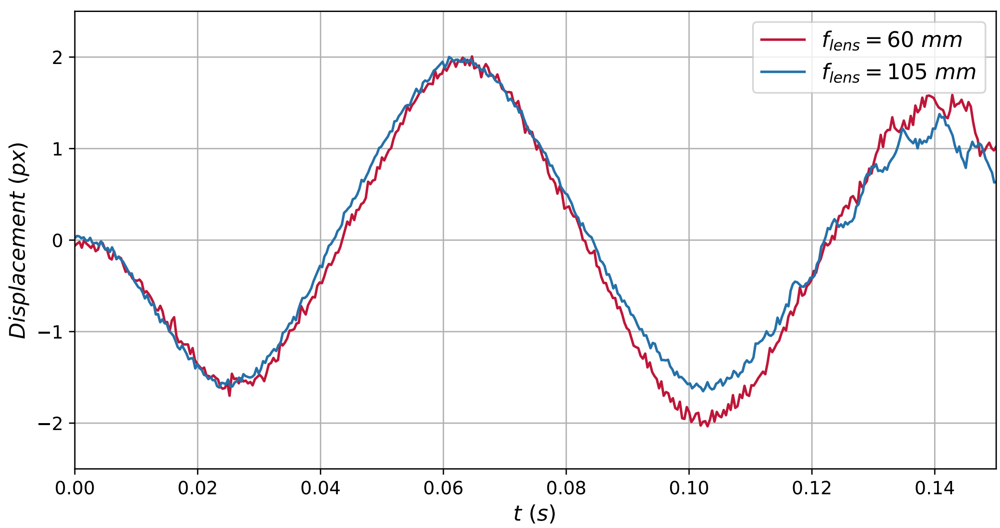

Figure 7.1: Displacement in x-direction as function of time for different lenses at an exposure time of 4 μs.

The movement of the model is corrected by interpolating the displacement field with a linear polynomial and subtracting it from the displacement field. The low polynomial order is chosen to make sure that the polynomial is not able to capture the density changes in the flow. An example of the low order polynomial in time is given in Figure 7.2.

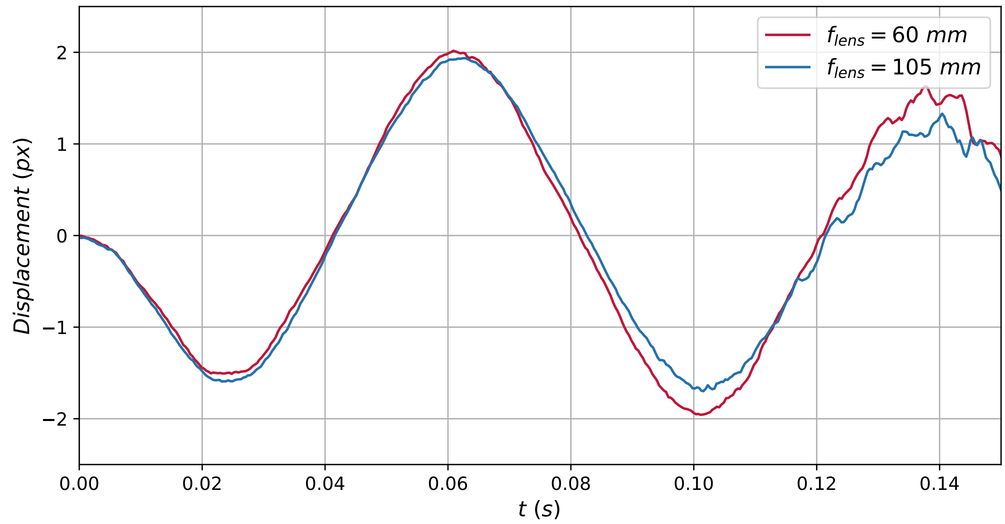

Figure 7.2: Linearly interpolated displacements for different lenses at an exposure time of 4 μs.

7.2. BOS Camera Settings

From Equation 4.3, it is known that the displacement due to a density change depends on the focal point (f). As also Z_A is influenced by f, it is hard to directly quantify the effect of changing the lens. Different lenses are tried to see the effect on the displacements. During the experiments, lenses with a 60 and 105 mm focal length are used. The displacements found using different lenses are given in Figure 7.3.

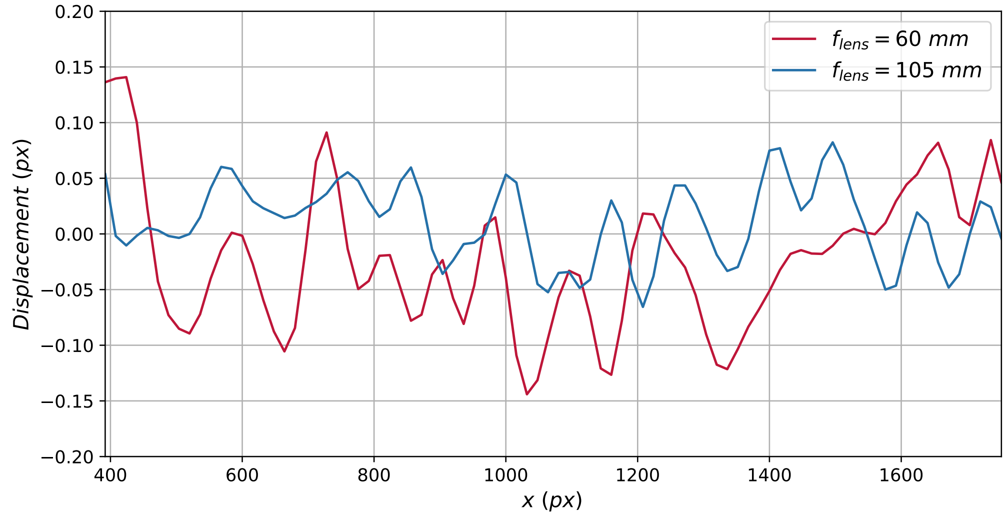

Figure 7.3: Displacements in x-direction corrected for the model motion at an exposure time of 4 μs.

What is observed, is that the displacements are below 0.15 px. This is lower than the accuracy level of the correlation, which is around 0.2 px. Also, there are no coherent structures present, these were expected from the conventional Schlieren results. The found displacements are therefore probably noise from the correlation method. Looking at the difference between the two lenses, it is observed that the noise for the 105 mm lens is slightly lower. A possible reason for that, is the fact that for a higher focal number, the camera has to move further from the model. This makes it possible to slightly increase the light in the test section.

BOS is largely affected by the amount of light that is shining on the speckles. For the correlation a large difference between intensities is beneficial as will be explained in Section 7.4. A way to increase the amount of light on the sensor is by increasing the exposure time. Therefore, a high exposure time is preferred when looking only at the BOS set-up. However, the high Mach number makes it impossible to increase the exposure time a lot. For the conventional Schlieren, the majority of the experiments are performed at an exposure time of 2 μs. The distance traveled of a wave in the shear layer is approximately:

$$d = V_{shear} t_{exposure} \tag{7.1}$$

In this equation, V_{shear} is the velocity of the shear layer, which is taken from Section 5.3 and is approximately $V_{shear} = 500\ m/s$. An exposure time of 2, 4 and 10 μs gives then a traveled distance of respectively 1, 2 and 10 mm. This means that increasing the exposure time will blur or average the shear layer. The exposure time is therefore limited to 4 μs. Figure 7.4 then shows the effect of the exposure time on the displacement for the 60 mm lens. It is indeed observed that increasing the exposure time slightly lowers the noise of the correlation method. This also points at the direction that there is not enough light present to do a proper correlation.

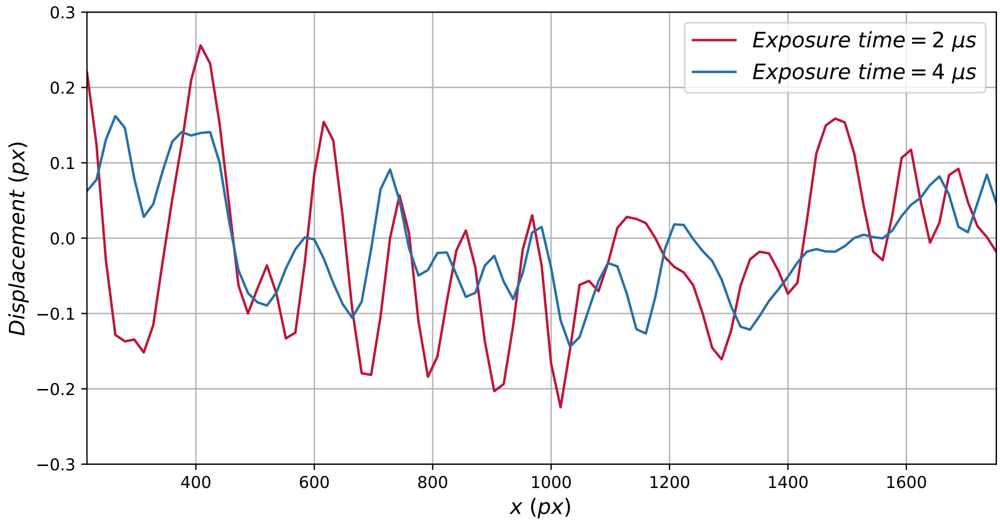

Figure 7.4: Displacements in x-direction corrected for the model motion using a lens with $f_{lens} = 60\ mm$.

7.3. Shock Generators

To determine why no density changes are observed, shock generators are used. The shock generators cause shock waves in the flow, which are strong density fluctuations. By doing this, it is possible to rule out that the density changes in the shear layer are too small to capture. So if nothing is found, then the correlation method is not accurate enough to correlate. If shock waves are found, then the density fluctuations in the shear layer are not strong enough to capture with the current method. In reality, the two depend on each other since for stronger density changes the correlation is easier to perform.

Two separate shock generators are used, one is a cylinder placed on the flat plate with a height larger than the boundary-layer thickness. The other one is the actual ramp, which is used to create the shear layer in the experiments. However, now the camera is focused on the reattachment region of the shear layer. On this location a strong reattachment shock wave is expected.

Figure 7.5 shows the shock generator and how the bow shock wave is going to form around it. On the red line the displacements in both x-direction and y-direction are calculated. On the red line two large peaks in displacement are expected at the location of the shock wave, with no displacement in the middle. In Figure 7.6 the results are given. What is observed, is that no displacement above the accuracy limit is present in both the x- and y-direction.

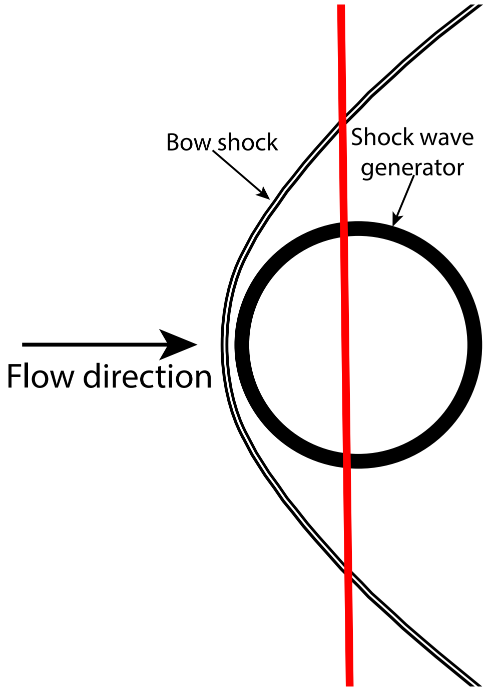

Figure 7.5: Schematic view of the shock wave generator and the displacement plane shown in Figure 7.6.

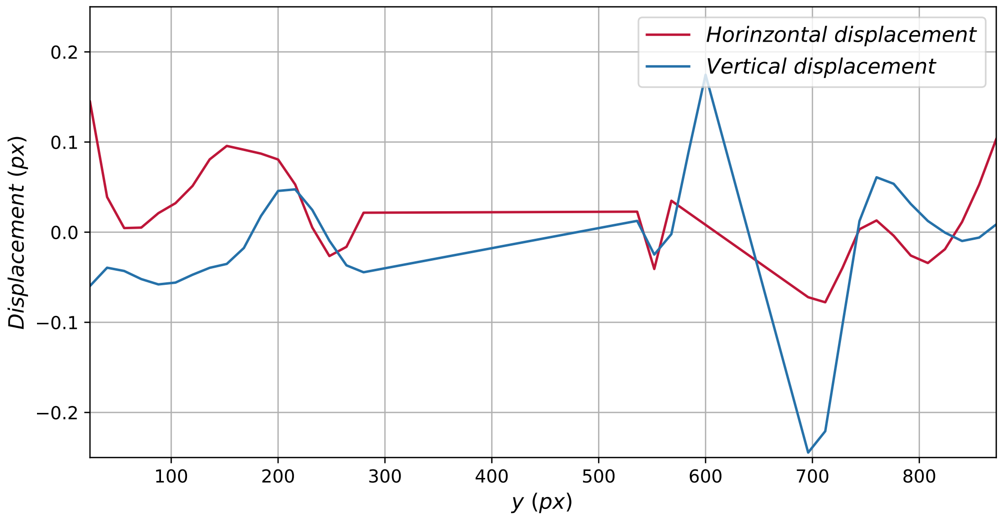

Figure 7.6: Displacements in x-direction and y-direction corrected for the model motion using a lens with f_{lens} = 105 mm.

To check whether the reattachment shock wave on the ramp is present, the displacements in x-direction is plotted on a vertical line over the ramp. A peak in displacements is expected near the reattachment region. Figure 7.7 shows the result. Also in this figure only noise levels are obtained.

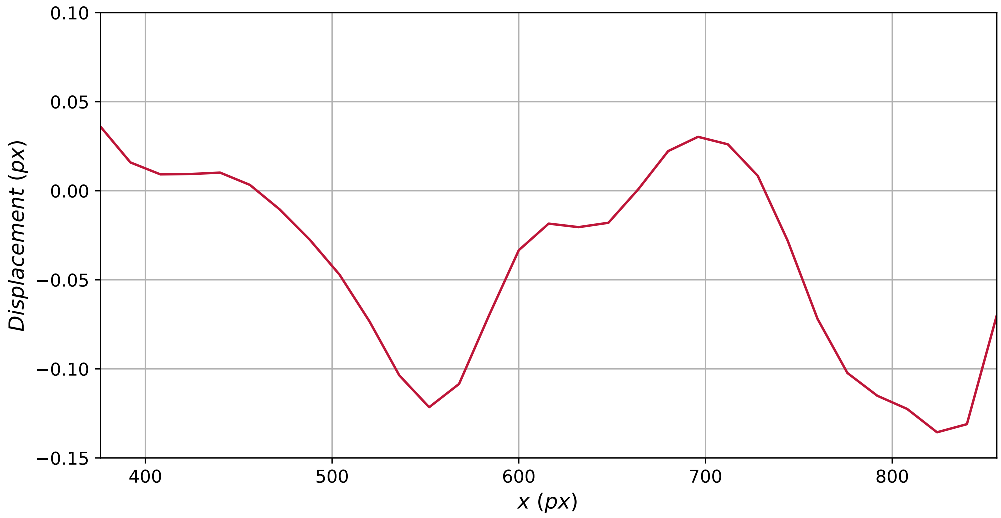

Figure 7.7: Displacements in x-direction on the ramp corrected for the model motion using a lens with $f_{lens} = 105\ mm$.

As both of the results do not show any sign of density changes, it is probably the correlation that has trouble dealing with the experiment conditions. In the next section a detailed discussion is presented on the correlation method and what might be the problem with it.

7.4. Correlation Method

Figure 7.8 gives the Root Mean Square (RMS) uncertainty for different pixel displacements. The different lines represent the difference in intensities between the particles (speckles) and background in bits. Because BOS uses PIV software for correlating the two images, this graph is also valid for BOS. In that case the particle image shift equals the speckle shift.

For intensity differences higher than 6 $bits$ ($2^6 = 64\ counts$) the RMS-uncertainty is not improving further. However, for lower differences the RMS-uncertainty increases rapidly. Especially for small speckle shifts, the performance deteriorates fast for low intensity differences.

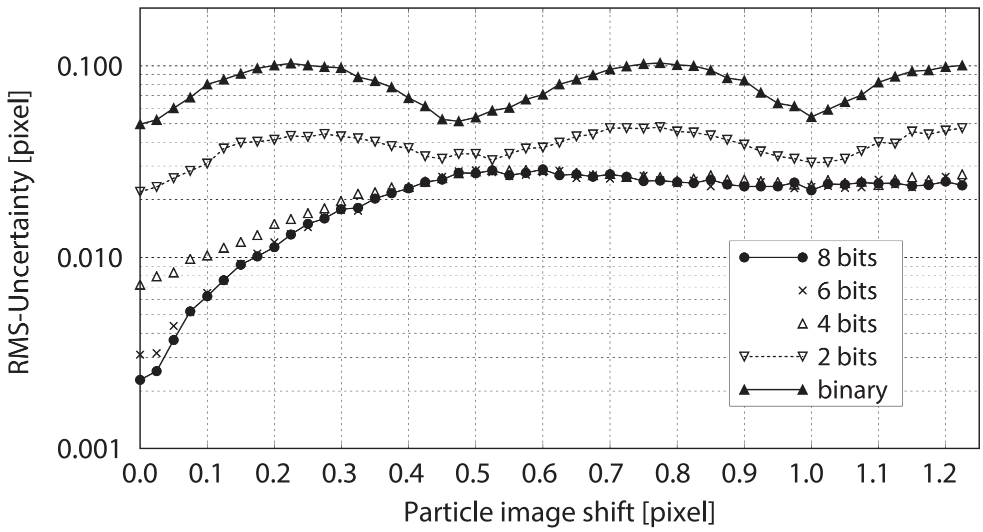

Figure 7.8: RMS - uncertainty as function of pixel displacement for PIV [25].

Table 7.1 shows the properties of the different experiments. Looking at the maximum intensity difference (ΔI), it is observed that for an exposure time of 4 μs and a speckle size of approximately $4-5$ an absolute maximum of 38 $counts$ is reached, which roughly equals 5 $bits$. In this case the order of the RMS-uncertainty equals the order of the speckle image shift. For the desired exposure time of 2 μs, the result is even worse because the signal consists of even less bits. Especially because these numbers are a maximum. Overall the intensity difference is considerably lower.

Furthermore, for the small speckle size, the shape of the speckle is lost which also contributes to a bad correlation. For the large speckle size this problem is solved, also the intensity difference is slightly increased but still lower than the desired 6 $bits$.

Table 7.1: Characteristics of the different BOS experiments.

Experiment	f_{lens} (mm)	Exposure time (μs)	Maximum ΔI $(counts)$	Speckle size (px)
1	60	2	26	4-5
2	60	4	33	4-5
3	60	10	47	4-5
4	105	2	30	4-5
5	105	4	38	4-5
6	105	10	58	4-5
7	180	4	41	10
8	105	2	35	10
9	105	4	47	10

For larger speckle shifts, an intensity difference of 4 $bits$ is sufficient to get the lowest RMS-uncertainty. Which in that case is considerably lower than the speckle image shift itself. This is the reason why the model motion is properly captured and the displacements due to density differences are not.

Figure 7.9 shows the noise on the windoff signal compared to the displacements found by the correlation in time. What is seen is that the order of the signal is the same as the order of the noise, meaning that a signal to noise ratio of 1 is found.

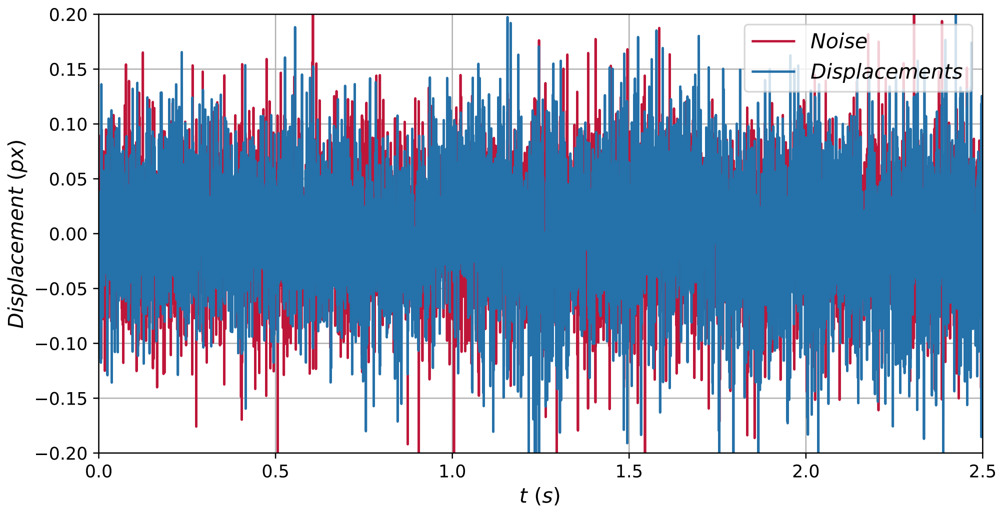

Figure 7.9: Displacements in x-direction corrected for the model motion and noise at an exposure time of 2 μs and f_{lens} = 105 mm.

Increasing the exposure time to 4 μs gives the figure stated in Figure 7.10. The noise level is approximately halved compared to Figure 7.9. This shows that the noise level can be lowered by adding more light. Together with Figure 7.8 and Table 7.1, it shows that not enough light was present in the test section to get proper results.

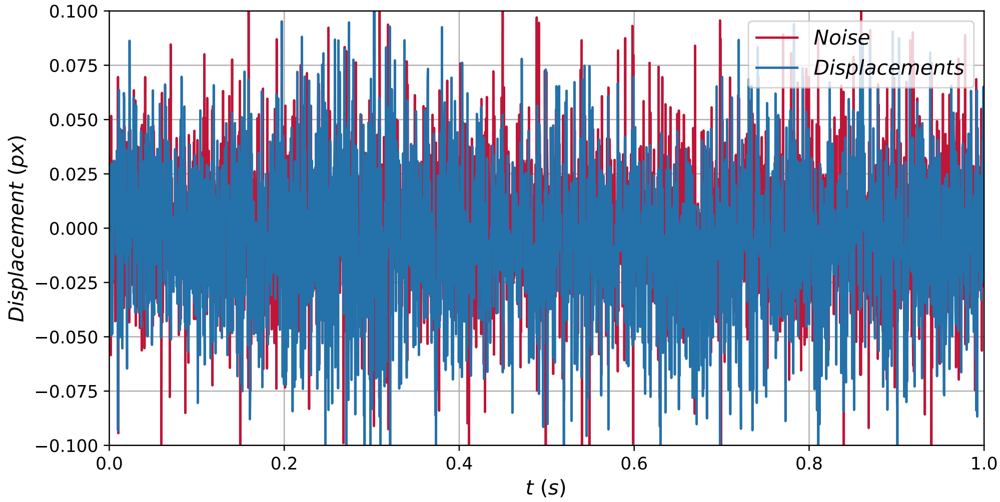

Figure 7.10: Displacements in x-direction corrected for the model motion and noise at an exposure time of 4 μs and $f_{lens} = 105\ mm$.

Looking at Figure 7.8, it is required to have at least a 6 $bits$ signal. This means that 64 $counts$ have to be present between the two images. This means that for an exposure time of 2, the intensity difference should at least double. It is hard to quantify the extra amount of light necessary, but it should be more than double in the way the lamps are positioned now.

8 Conclusion

In this thesis the strong shock wave boundary-layer interactions on a compression ramp in a hypersonic flow is investigated. To successfully do this, test models are developed with varying ramp angle. Furthermore, the existed flat plate model is adapted such that it can house different models including the compression ramps.

Also, a Schlieren set-up is made and the infrared camera was successfully calibrated to make a quantitative analysis possible. Next to that, calibration plates are designed which can map the measurements to physical coordinate systems.

The Schlieren measurements were performed to visualize the flow topology in front of the compression ramp. It shows that for all ramps the flow is separated and a strong shear layer is present. Also, very clearly compression waves stemming from instability waves in the shear layer are observed.

Using the Schlieren data the effect of ramp angle and Reynolds number are tested on the shear layer length. It showed that there is a clear increase in shear layer length for increasing both the ramp angle and Reynolds number. When comparing the data to theoretical equations, it shows that it is very hard to have correct predictions in this Reynolds number and Mach range. A possible reason for this, is the transitional state of the shear layer.

For the investigation of the shear layer instability waves, a Standard Deviation (STD) field is computed. This showed that the instability waves are growing in the shear layer and that the shape is probably not constant throughout the shear layer.

The QIRT data gives a good quantification of the heat fluxes present on the ramp. It shows clearly the dependency of the heat flux overshoot on compression ramp angle. For small angles the overshoot is not observed, while for high compression ramp angles a severe overshoot is found.

Also, the peak heat fluxes are hard to predict with existing correlations due to the transitional behavior of the shear layer in the Reynolds number range of the experiments.

Next to that, additional evidence is found of the presence of transitional waves in the shear layer in the form of spanwise streaks. The magnitude change due to these streaks could not be found, but an investigation on the non-dimensional wavelength is done. This showed that two types of waves are present, large ones and smaller waves on top of the large waves. Both waves show a decrease in non-dimensional wavelength for an increase in Reynolds number.

At last, it turned out that the BOS set-up was not accurate enough to see density fluctuations. An investigation was performed on the potential cause and it turned out, that probably there was not enough light in the test section. This resulted in a cross correlation that gave a signal to noise ratio of one.

Overall, the experiments clearly showed the different attributes present in a strong shock wave boundary-layer interaction. Additional features were found which can be linked to large instability waves in the shear layer. This opens up a lot of possibilities to deeper investigate the transitional behavior of the shear layer and the effect it has on the overall flow topology. Also, work can be put into making BOS a successful non-intrusive measurement method in hypersonic flows.

9
Recommendations

In this chapter some recommendations for future research are given. These are split into three sections which each treat a different experimental method used for this report.

9.1. Schlieren Imaging

During the Schlieren experiments a lot of global data is gathered of the flow field and instability waves in the shear layer. For future research it would be nice to have a closer look into the shear layer and to see what type of instabilities are found.

During these experiments this was already tried using a burst light, however, this led to an overexposed shear layer so no unsteady details could be seen. More time can be put into avoiding this overexposure which makes it possible to see the unsteady nature of the waves more clearly.

Furthermore, in this report a lot of emphasis is put in the reattachment region. Because of this, the separation point and the formation of the disturbances, fell outside the image. Future experiments can focus on the separation point by moving the ramp aft, such that the start of the shear layer can be investigated.

At last, a velocity profile of the shear layer can help in identifying the type of instability present in it. This can be done by doing (Tomo-)PIV measurements. For example, it might be possible to see the pumping motion of the Görtler instabilties present in the shear layer.

9.2. QIRT

During the processing of the QIRT data, two concerns were found that could be improved in future experiments. The first one consists of the distance between the camera and the model. During the analysis of the spanwise waves it was found that a lot of aliasing was present in the small peaks. This made it impossible to find the effect on the magnitude of the Stanton number. For future experiments the camera should be placed closer to the model such that a higher spatial resolution can be obtained.

The second concern is that more holes should be made into the mapping plates. In these experiments there were not enough holes present to do an accurate 2D interpolation. This was fixed by doing two 1D interpolation near the region of interest which introduces an error when moving away from the interpolation location. Especially when the interpolation area is going to be in the whole shock wave boundary-layer interaction region, a 2D interpolation method is required.

9.3. BOS

As explained in the report, the BOS method used was not accurate enough to obtain any data. This was attributed to the lack of light in the section, as a result the cross correlation could be performed properly.

For future experiments more emphasis should be put on getting more light in the test section. This can be done by for example placing LED strips in a ring around the wind tunnel window inside the test section. Besides that, it is nicer to start with a configuration that creates density differences so large that they are found with the cross correlation software. From that baseline point, the density differences can be lowered to the point where they are not visible anymore. This defines the boundaries of the method better and makes it easier to solve any difficulties when looking at small density fluctuations.

Bibliography

[1] G.J. Brauckmann, J.W. Paulson Jr., and K.J. Weilmuenster. Experimental and Computational Analysis of Shuttle Orbiter Hypersonic Trim Anomaly. *Journal of Spacecraft and Rockets*, 32(5):758–764, 1995.

[2] Nasa space shuttle image gallery. `https://www.nasa.gov/sites/default/files/images/323502main_2009-2377_full.jpg`. Accessed: 29 October 2019.

[3] John D. Anderson Jr. *Hypersonic and High Temperature Gas Dynamics*. American Institute of Aeronautics and Astronautics, Inc., Reston, Virginia, second edition, 2006.

[4] Dr.ir. B.W. van Oudheusden. Ae4120 viscous flows 3: Laminar boundary-layer. Presentation, slide 19, 2016.

[5] H. Babinsky and J.K Harvey. *Shock Wave - Boundary-Layer Interactions*. Cambridge University Press, New York, first edition, 2011.

[6] D. Arnal and J.M. Délery. Laminar-turbulent transition and shock wave/boundary layer interaction. In *Critical Technologies for Hypersonic Vehicle Development*, chapter 4, pages 4–1 – 4–46. RTO/NATO, Neuilly-sur-Seine Cedex, first edition, 2005.

[7] M.S. Holden. Boundary-layer displacement and leading-edge bluntness effects on attached and separated laminar boundary layers in a compression corner. Part II: Experimental study. *AIAA Journal*, 9(1):84–93, 1971.

[8] E. Katzert. On the lengthscales of laminar shock/boundary-layer interaction. *Journal of Fluid Mechanics*, 206:477–496, 1989.

[9] M. Marini. Analysis of hypersonic compression ramp laminar flows under sharp leading edge conditions. *Aerospace Science and Technology*, 5(4):257–271, 2001.

[10] F.T. Hung and D.O. Barnett. Shockwave - Boundary Layer Interference Heating Analysis. *AIAA Paper*, 73-237, 1973.

[11] M.S. Holden. Experimental Studies of Shock Wave - Boundary-Layer Interaction. In *Two-Dimensional Shock Wave - Boundary Layer Interactions in High Speed Flows*, pages 41–110, Neuilly-sur-Seine, France, 1975. AGARD.

[12] G.A. Simeonides. Hypersonic Shock Wave Boundary Layer Interactions over Simplified Deflected Control Surface Configurations. Technical Report AGARD 792, AGARD, Neuilly-sur-Seine, 1993.

[13] F.F.J. Schrijer and W.J. Bannink. Description and Flow Assessment of the Delft Hypersonic Ludwieg Tube. *Journal of Spacecraft and Rockets*, 47(1):125–133, 2010.

[14] F.F.J. Schrijer. *Experimental investigation of re-entry aerodynamic phenomena*. PhD thesis, Delft University of Technology, Delft, 2010.

[15] Q. Ye, F.F.J. Schrijer, and F. Scarano. Tomographic PIV Measurement of Hypersonic Boundary Layer Transition Past a Micro-ramp. *47th AIAA Fluid Dynamics Conference*, (June):1–11, 2017.

[16] D. Ekelschot. Investigation of Görtler vortices in hypersonic flow using Quantitative Infrared Thermography (QIRT) and Tomographic Particle Image Velocimetry (Tomo-PIV). Master's thesis, TU Delft, 2012.

[17] M. Raffel. Background-oriented schlieren (BOS) techniques. *Exp Fluids*, 56(60), 2015.

[18] F. Scarano. Experimental aerodynamics. Technical Report February, TU Delft, Delft, 2013.

[19] F.F.J. Schrijer. *Transient heat transfer measurements in a short duration hypersonic facility on a blunted cone-flare using QIRT*. PhD thesis, TU Delft, 2003.

[20] F.F.J. Schrijer. Investigation of Görtler vortices in a hypersonic double compression ramp flow by means of infrared thermography. *Quantitative InfraRed Thermography Journal*, 7(2):201–215, 2010.

[21] R. Mayer. Orientation on quantitative ir-thermography in wall-shear stress measurements. Technical report, Delft University of Technology, Faculty of Aerospace Engineering, Delft, 1996.

[22] M.J. Flanagan. Aerodynamic heating in the vicinity of hypersonic, axisymmetric, shockwave-boundary layer interactions. *AIAA-paper*, 93-2766, 1993.

[23] S. Cao, I. Klioutchnikov, and H. Olivier. Görtler Vortices in Hypersonic Flow on Compression Ramps. *AIAA Journal*, pages 1–11, 2019.

[24] A. Roghelia, P. Chuvakhov, H. Olivier, and I. Egorov. Experimental investigation of Görtler vortices in hypersonic ramp flows behind sharp and blunt leading edges. Technical Report June, AIAA, 2017.

[25] M. Raffel, C. Willert, S. Wereley, and J. Kompenhans. *Particle Image Velocimetry: A Practical Guide*. Springer-Verlag, Berlin Heidelberg, second edition, 2007.

A

Compression Ramp Models

In this appendix the remainder of the compression ramps used during the experiments are presented.

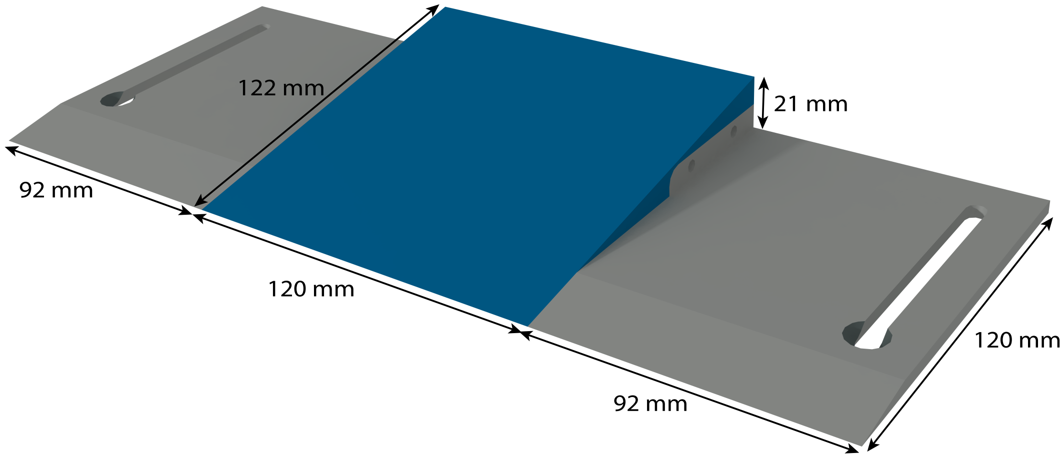

Figure A.1: Isometric view of the 10° compression ramp.

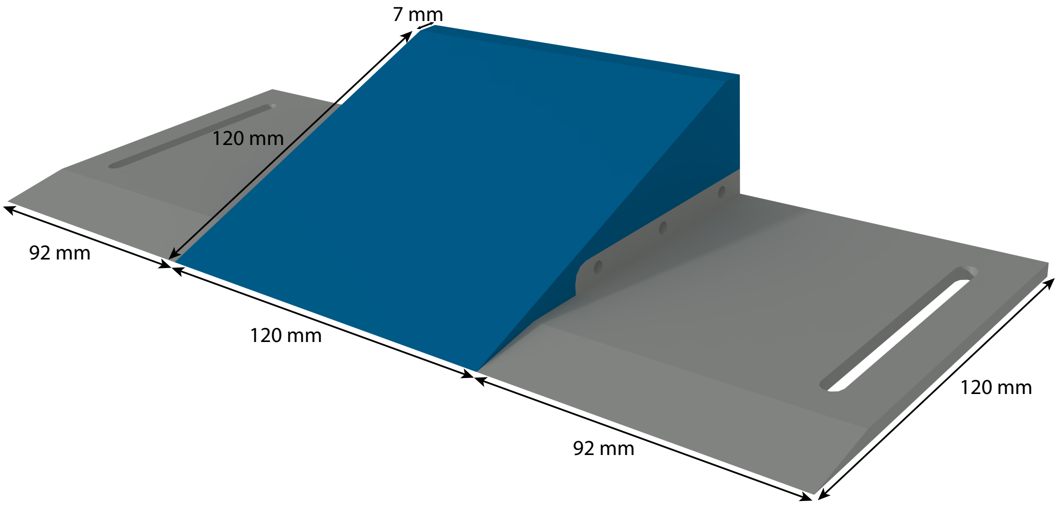

Figure A.2: Isometric view of the 20° compression ramp.

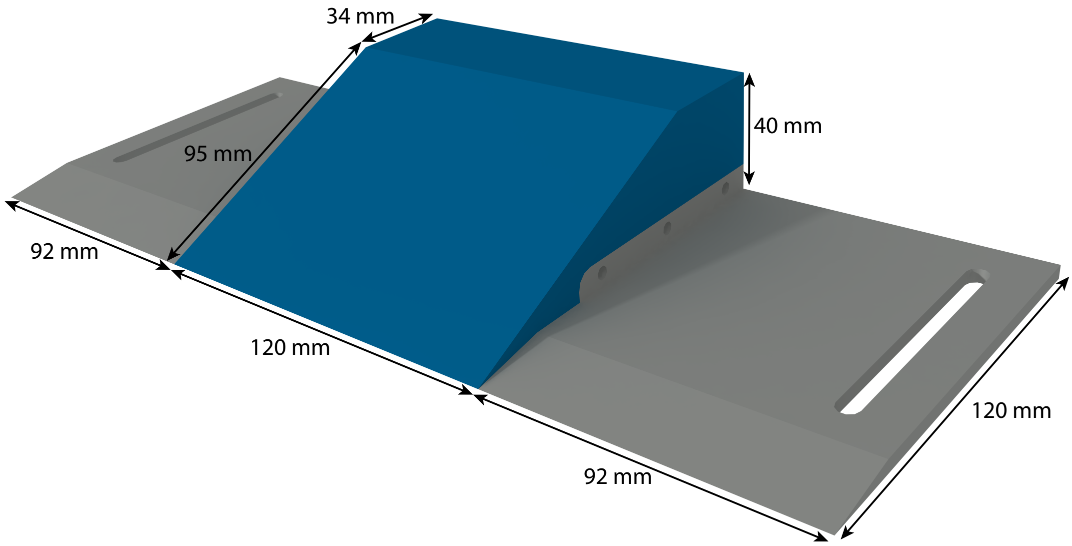

Figure A.3: Isometric view of the 25° compression ramp.

B

Additional Schlieren Data

B.1. Compression Wave Angles

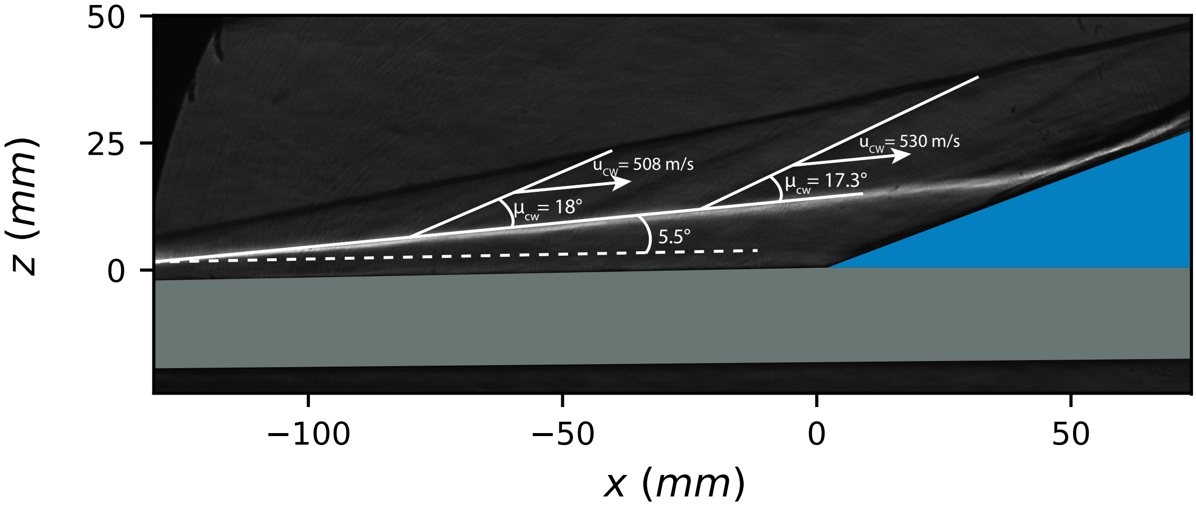

Figure B.1: Compression wave angles of for the 20° ramp with $Re_L = 5.30 \cdot 10^6$.

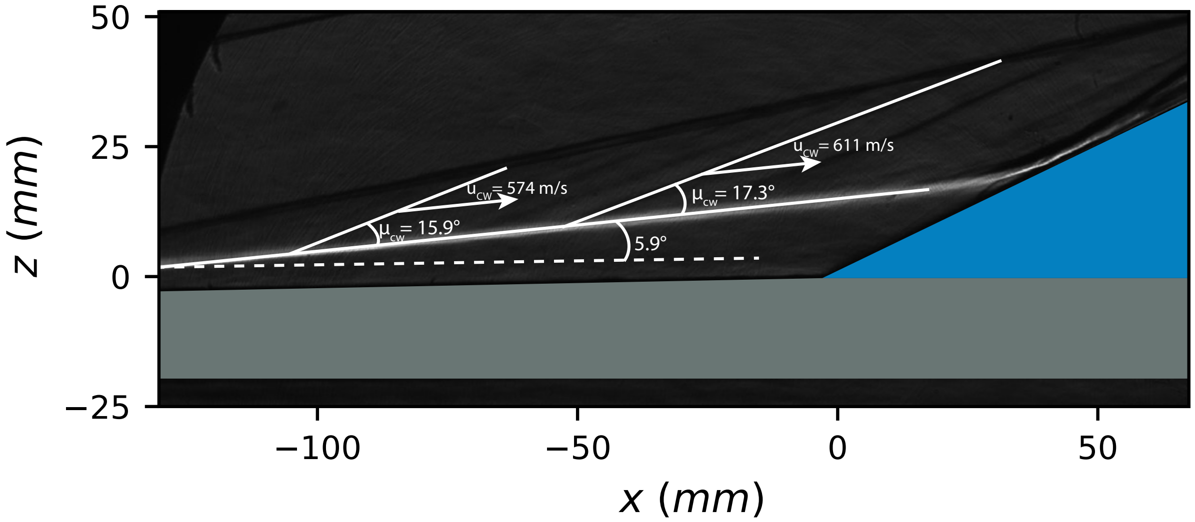

Figure B.2: Compression wave angles of for the 25° ramp with $Re_L = 5.30 \cdot 10^6$.

B.2. Correlations

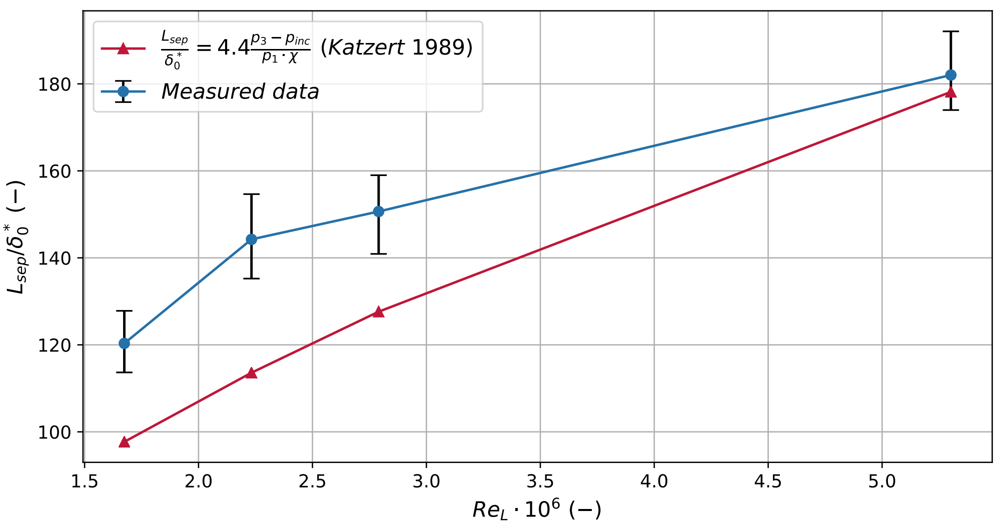

Figure B.3: Shear layer length (L_{sep}/δ_0^*) for the 20° angle and theoretical data from Equation 2.27.

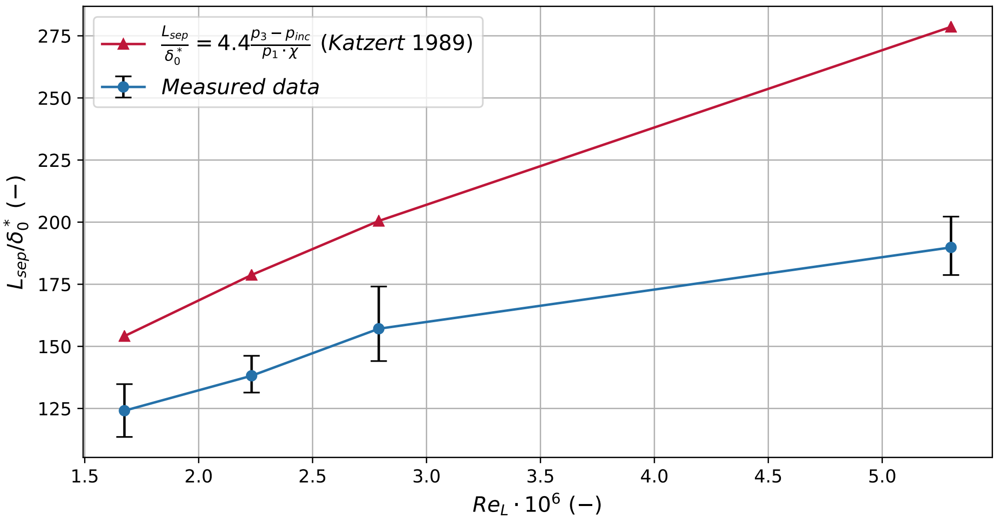

Figure B.4: Shear layer length (L_{sep}/δ_0^*) for the 25° angle and theoretical data from Equation 2.27.

B.3. STD Fields

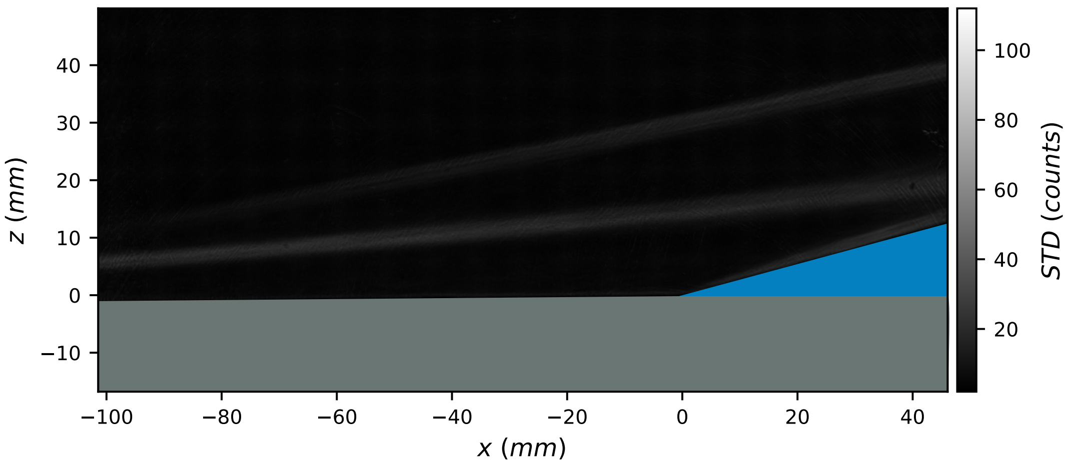

Figure B.5: STD field for the 15° ramp with $Re_L = 1.67 \cdot 10^6$.

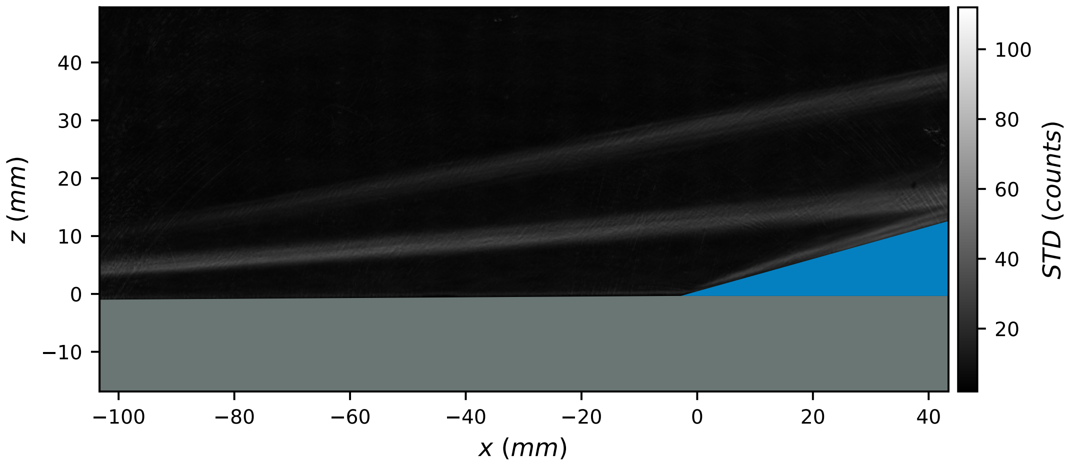

Figure B.6: STD field for the 15° ramp with $Re_L = 2.79 \cdot 10^6$.

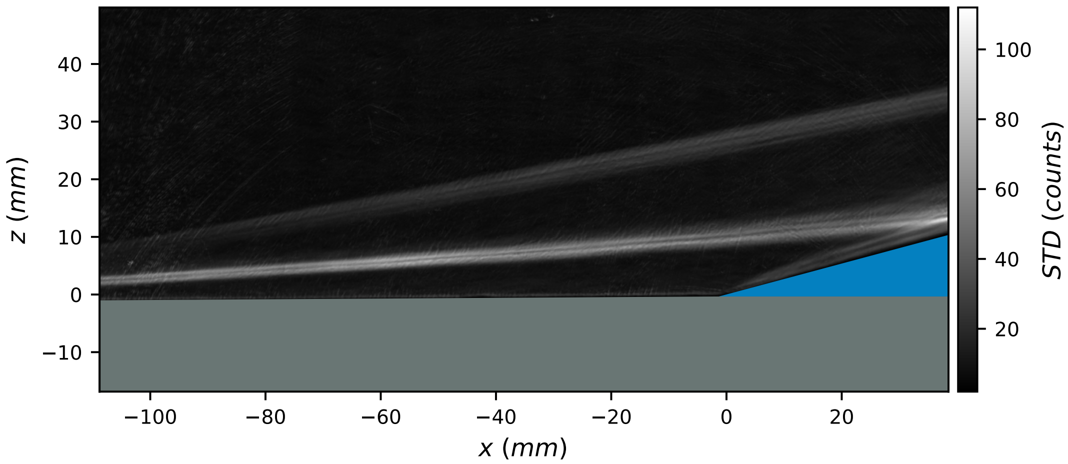

Figure B.7: STD field for the 15° ramp with $Re_L = 5.30 \cdot 10^6$.

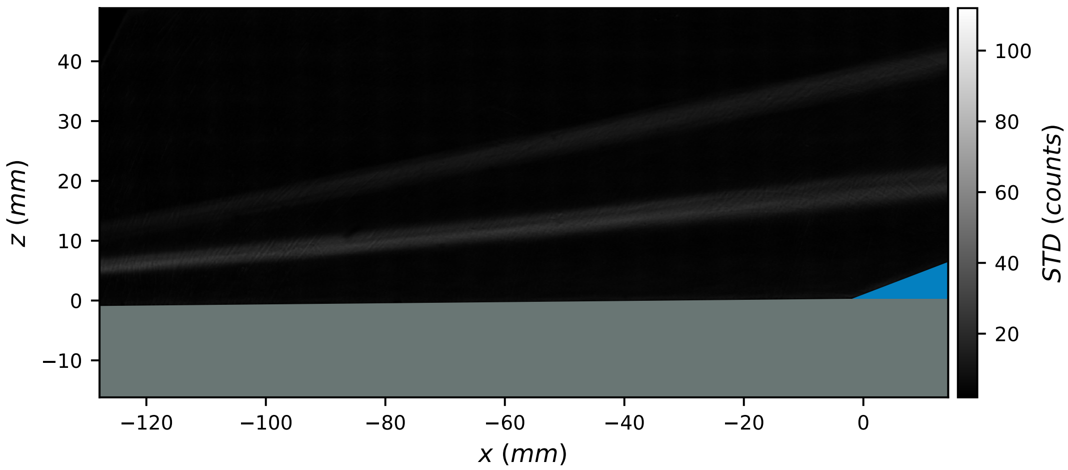

Figure B.8: STD field for the 20° ramp with $Re_L = 1.67 \cdot 10^6$.

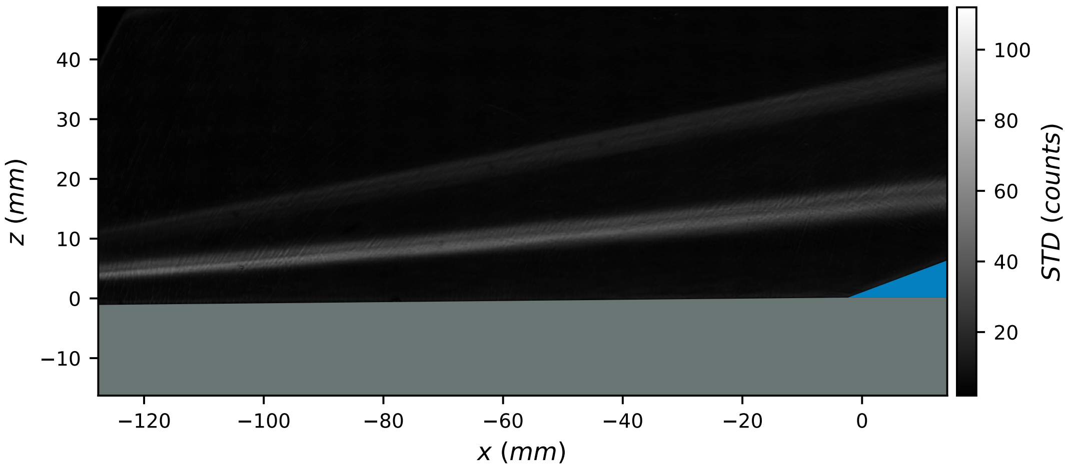

Figure B.9: STD field for the 20° ramp with $Re_L = 2.79 \cdot 10^6$.

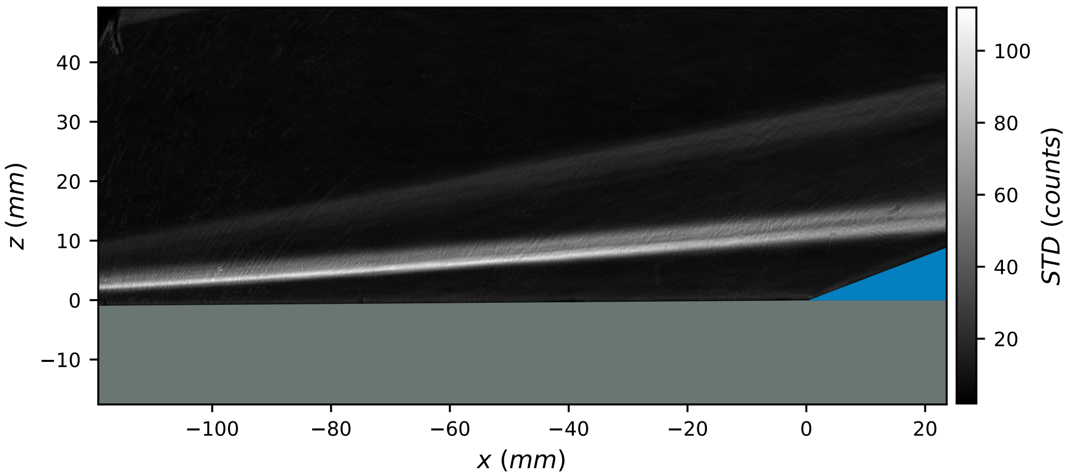

Figure B.10: STD field for the 20° ramp with $Re_L = 5.30 \cdot 10^6$.

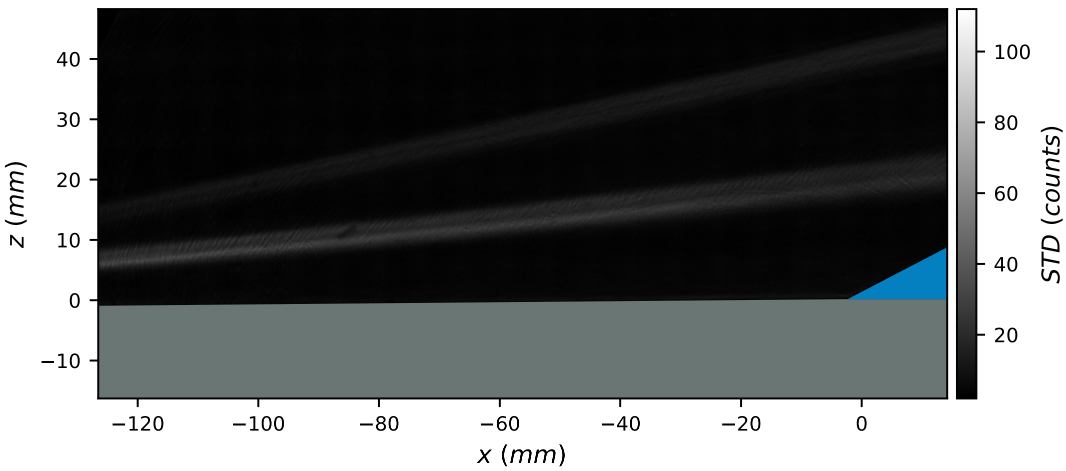

Figure B.11: STD field for the 25° ramp with $Re_L = 1.67 \cdot 10^6$.

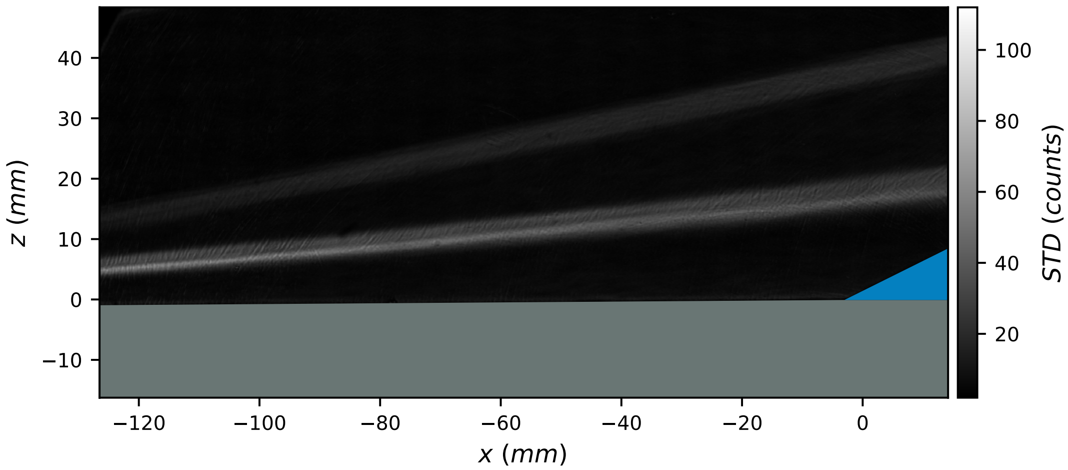

Figure B.12: STD field for the 25° ramp with $Re_L = 2.79 \cdot 10^6$.

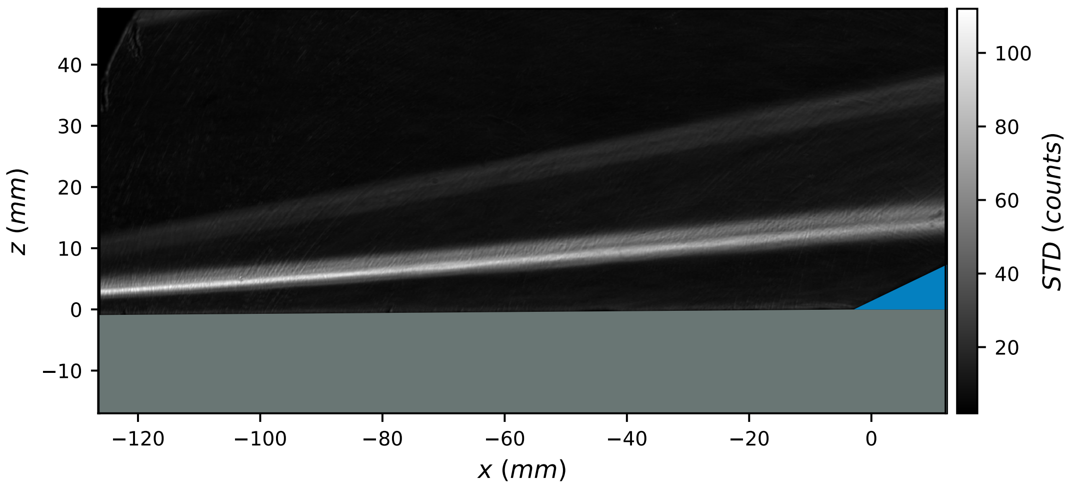

Figure B.13: STD field for the 25° ramp with $Re_L = 5.30 \cdot 10^6$.

C

Additional QIRT Data

C.1. Streamwise Stanton Number

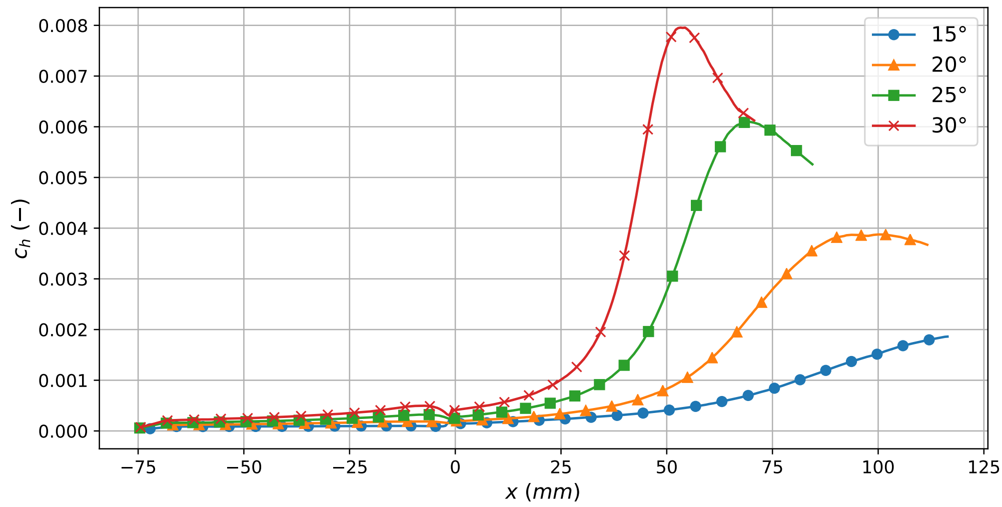

Figure C.1: Streamwise Stanton numbers (c_h) for different ramp angles at $Re_L = 1.67 \cdot 10^6$

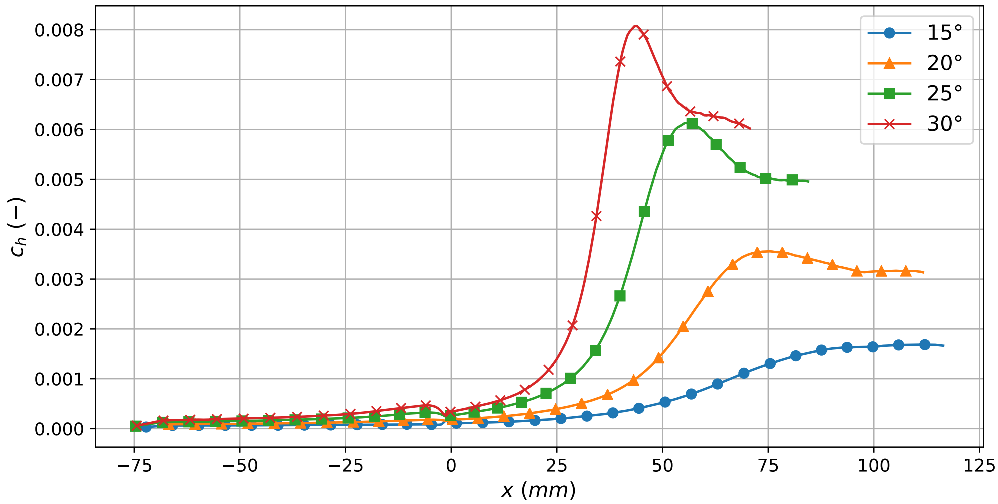

Figure C.2: Streamwise Stanton numbers (c_h) for different ramp angles at $Re_L = 3.35 \cdot 10^6$

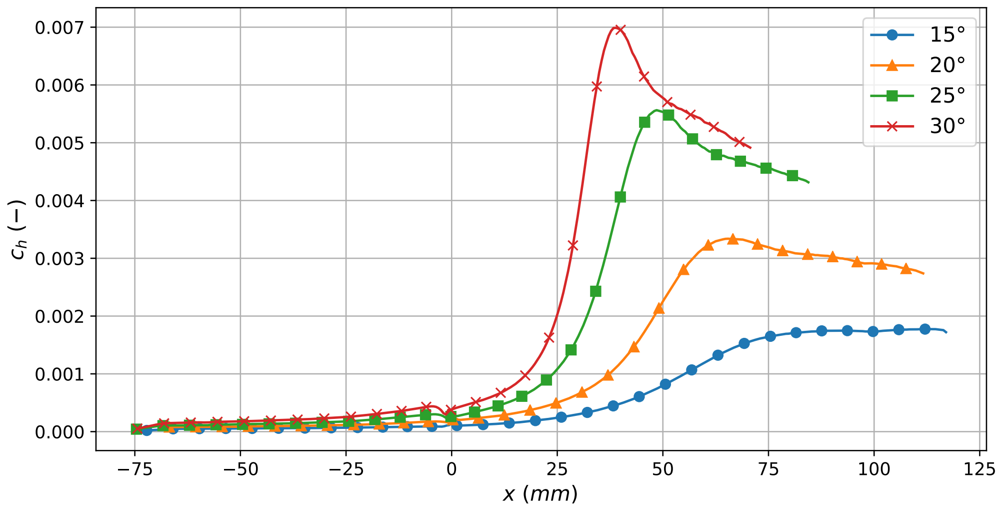

Figure C.3: Streamwise Stanton numbers (c_h) for different ramp angles at $Re_L = 5.02 \cdot 10^6$

C.2. Peak Stanton Numbers

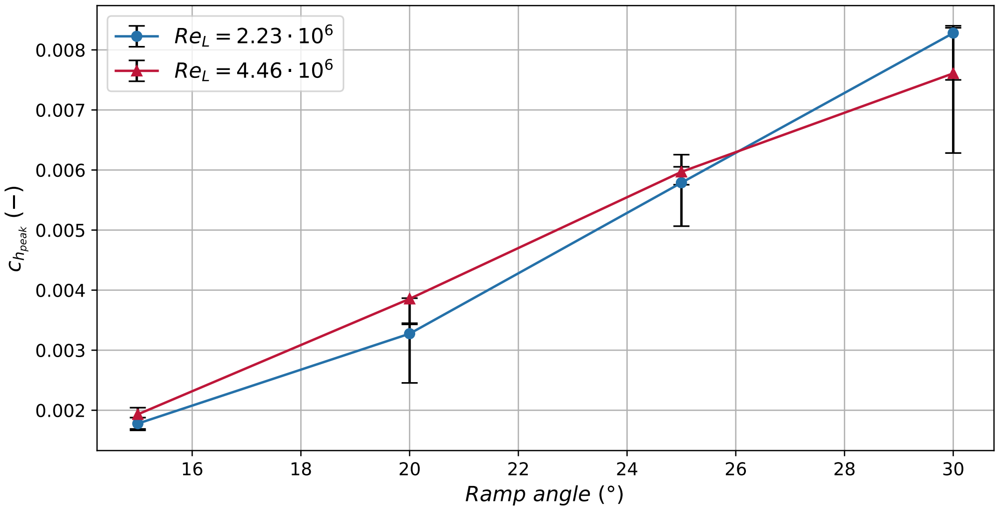

Figure C.4: Peak Stanton numbers ($c_{h_{peak}}$) for different ramp angles at $Re_L = 2.23 \cdot 10^6$ and $Re_L = 4.46 \cdot 10^6$.

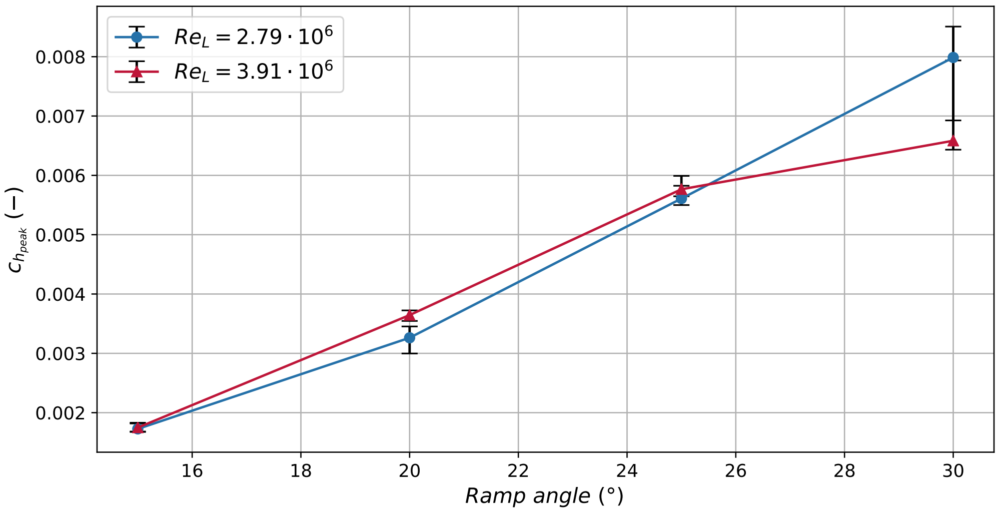

Figure C.5: Peak Stanton numbers ($c_{h_{peak}}$) for different ramp angles at $Re_L = 2.79 \cdot 10^6$ and $Re_L = 3.91 \cdot 10^6$.

C.3. Wavelengths

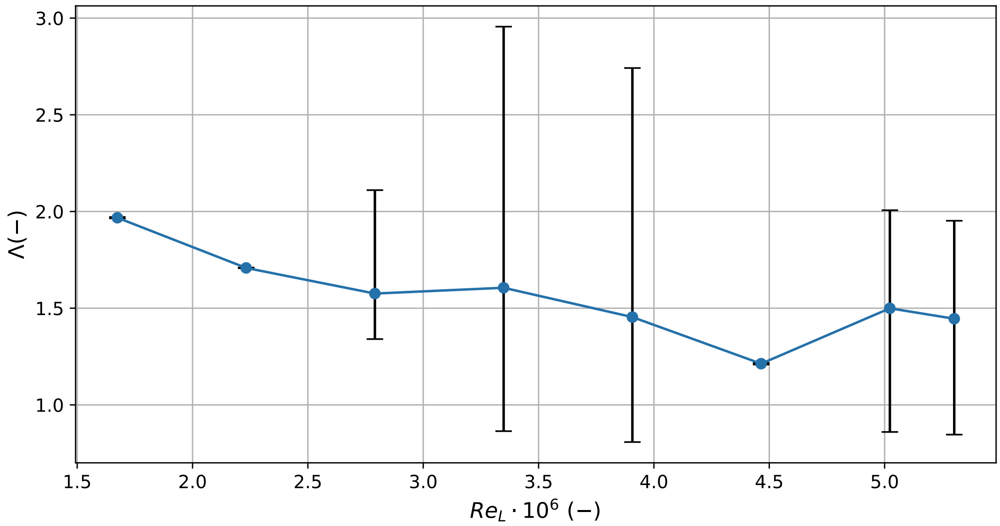

Figure C.6: Non-dimensional wavelength (Λ) for the large wavelength waves for the 20° ramp as function of Reynolds number.

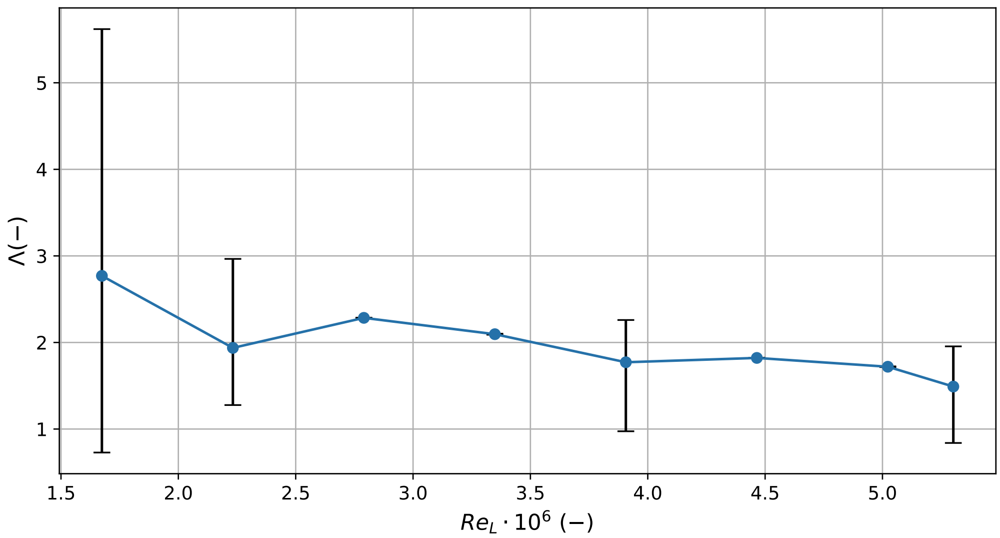

Figure C.7: Non-dimensional wavelength (Λ) for the large wavelength waves for the 25° ramp as function of Reynolds number.

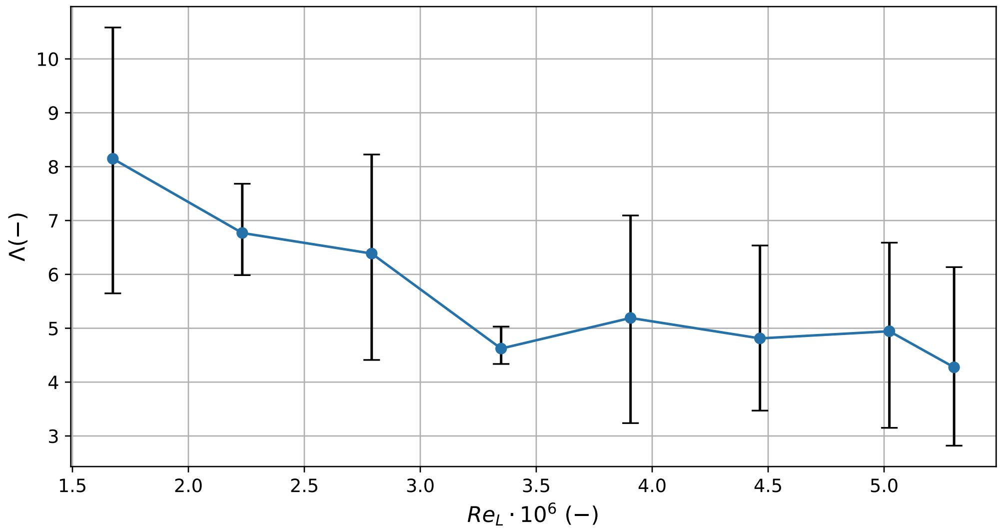

Figure C.8: Non-dimensional wavelength (Λ) for the small wavelength waves for the 20° ramp as function of Reynolds number.

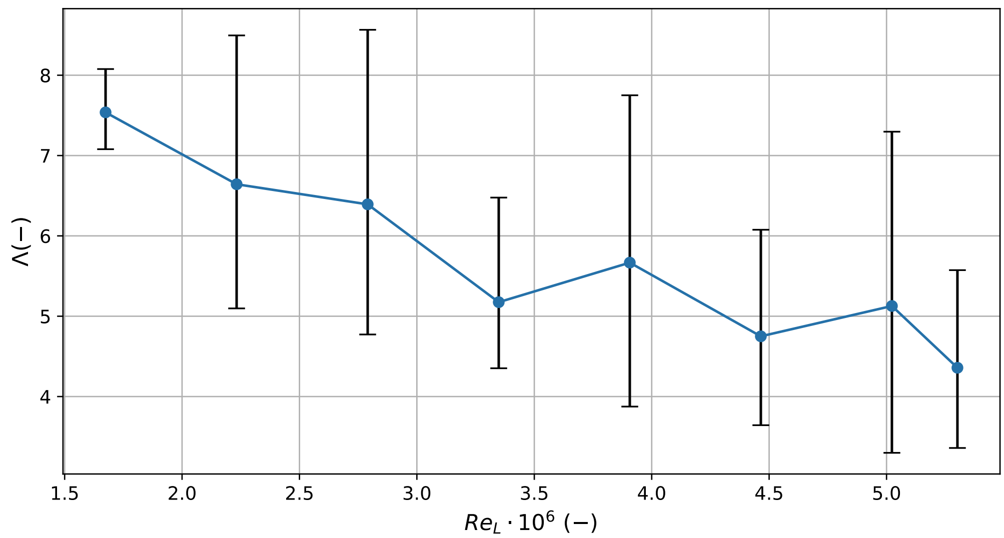

Figure C.9: Non-dimensional wavelength (Λ) for the small wavelength waves for the 25° ramp as function of Reynolds number.

D

Test Matrices

D.1. Schlieren

Table D.1: Schlieren test matrix day 1

$Test\ Nr.$	$ET\ (\mu s)$	$Ramp$	$T_{hot} \approx 500\ (K)$	$T_{cold} \approx 100\ (K)$	$p_t \approx 95\ (bar)$	$Pivot\ hole$	$p_{vac} < 4\ (mbar)$
1	2	-	✓	✓	95	BC	✓
2	100	-	✓	✓	95	EF	✓
3	2	10°	✓	✓	95	BC	✓
4	2	10°	✓	✓	95	BC	✓
5	2	10°	✓	✓	95	BC	✓
6	100	10°	✓	✓	94.75	EF	✓
9	2	20°	✓	✓	95	BC	✓
10	2	20°	✓	✓	95	BC	✓
11	2	20°	✓	✓	95	BC	✓
12	100	20°	✓	✓	95	EF	✓
13	100	20°	✓	✓	95	EF	✓
14	100	20°	✓	✓	95	EF	2.7
15	2	15°	✓	✓	95	BC	✓
16	2	15°	✓	✓	95	BC	✓
17	2	15°	✓	✓	95	BC	✓
18	100	15°	✓	✓	95	EF	✓
21	2	25°	✓	✓	95	BC	✓
22	2	25°	✓	✓	95	BC	✓
23	2	25°	✓	✓	95	BC	✓
24	100	25°	✓	✓	95	EF	✓
25	100	25°	✓	✓	95	EF	✓
26	100	25°	✓	✓	95	EF	✓
27	2	30°	✓	✓	95	BC	✓
28	2	30°	✓	✓	95	BC	✓
29	2	30°	✓	✓	95	BC	✓
30	100	30°	✓	✓	95	EF	✓
31	100	30°	✓	✓	95	EF	✓
32	100	30°	✓	✓	95	EF	✓

Table D.2: Schlieren test matrix day 2

$Test\ Nr.$	$ET\ (\mu s)$	$Ramp$	$T_{hot} \approx 500\ (K)$	$T_{cold} \approx 100\ (K)$	$p_t\ (bar)$	$Pivot\ hole$	$p_{vac}\ (mbar)$
1	2	30°	✓	✓	50	BC	3.08
2	2	30°	✓	✓	40	BC	2.607
3	2	30°	✓	✓	35	BC	2.637
4	2	30°	✓	✓	30	BC	2.72
5	2	30°	✓	✓	95	BC	2.7
6	2	30°	✓	✓	40	AB	2.75
7	2	30°	✓	✓	50	AB	2.75
8	2	30°	✓	✓	95	AB	2.4
9	2	30°	✓	✓	30	AB	2.32
10	100	30°	✓	✓	30	EC	2.54
11	2	10°	✓	✓	50	BC	2.35
12	2	10°	✓	✓	40	BC	2.5
13	2	10°	✓	✓	30	BC	2.45
14	2	15°	✓	✓	50	BC	2.6
15	2	15°	✓	✓	30	BC	2.6
16	2	25°	✓	✓	30	BC	2.6
17	2	25°	✓	✓	40	BC	2.65
18	2	25°	✓	✓	50	BC	2.65
19	2	20°	✓	✓	30	BC	2.56
20	2	20°	✓	✓	40	BC	2.8
21	2	20°	✓	✓	50	BC	2.7
22	2	20°	✓	✓	95	BC	2.9

Table D.3: Schlieren test matrix day 3

$Test\ Nr.$	$ET\ (\mu s)$	$Ramp$	$T_{hot} \approx 500\ (K)$	$T_{cold} \approx 100\ (K)$	$p_t\ (bar)$	$Pivot\ hole$	$p_{vac}\ (mbar)$	fps
1	2	15°	✓	✓	95=94.61	BC	2.5	1280
2	2	15°	✓	✓	95=94.58	BC	2.5	1280
3	2	15°	✓	✓	95=94.65	BC	2.2	1280
4	2	15°	✓	✓	50=50.34	BC	2.4	1280
5	2	15°	✓	✓	40=40.34	BC	2.4	1280
6	2	15°	✓	✓	30=30.46	BC	2.3	1280
7	2	15°	✓	✓	80=80.4	BC	2	1280
8	2	15°	✓	✓	70=70	BC	2	1280
9	2	15°	✓	✓	60=60.08	BC	2.5	1280
10	2	30°	✓	✓	60=60.17	BC	2.3	1280
11	2	30°	✓	✓	70=70.02	BC	2.2	1280
12	2	30°	✓	✓	80=79.87	BC	1.8	1280
13	2	30°	✓	✓	95=94.86	BC	1.16	3863
14	2	30°	✓	✓	95=94.64	BC	1.84	8149
15	2	30°	✓	✓	30=30.1	BC	1.6	8149
16	2	30°	✓	✓	30=30.05	BC	2.6	5319
17	2	30°	✓	✓	30=30	BC	2	9661,4
18	2	30°	✓	✓	95=94.87	BC	2	9661
19	1000	30°	✓	✓	95=94.86	FG	2.2	195
20	952	30°	✓	✓	95=94.78	FG	2.2	975
21	952	30°	✓	✓	95=94.6	EF	2.2	975
22	400	30°	✓	✓	95=94.5	EF	2	975
23	400	30°	✓	✓	?	EF	2	975
24	400	30°	✓	✓	95=94.64	HJ	2.5	975
25	400	30°	✓	✓	95=94.5	EF	1	975
26	400	30°	✓	✓	95=94.66	EF	1.4	975
27	400	30°	✓	✓	95	EF	2.5	975
28	400	30°	✓	✓	95=94.55	EF	2.2	975
29	400	30°	✓	✓	95=94.51	EF	2	975
30	400	30°	✓	✓	95=94.51	EF	2	975
31	1.28	30°	✓	✓	95=94.75	BC	2.5	Max
32	1.28	30°	✓	✓	95	BC	1.5	6236,9
33	1.28	30°	✓	✓	95	BC	1.28	9649,5
34	1.28	30°	✓	✓	95=94.55	BC	1.95	9649
35	1.28	30°	✓	✓	95=94.57	BC	1.9	21559
36	1.28	30°	✓	✓	95=94.52	BC	1.5	21559
37	1.28	30°	✓	✓	95=94.51		1.47	21559
38	1.28	30°	✓	✓	95=94.51	AB	2.8	48412
39	1.28	30°	✓	✓	95=94.56	HG	2.8	60620
40	1.28	30°	✓	✓	95=94.51	EF	1.38	60620

D.2. QIRT

Table D.4: QIRT test matrix

$Test\ Nr.$	$ET\ (\mu s)$	$Ramp$	$T_{hot} \approx 500\ (K)$	$T_{cold} \approx 100\ (K)$	$p_t\ (bar)$	$p_{vac}\ (mbar)$	fps
1	144	30°	✓	✓	30	✓	200
2	144	30°	✓	✓	40	✓	200
3	144	30°	✓	✓	50	✓	200
4	144	30°	✓	✓	60	✓	200
5	144	30°	✓	✓	70	✓	200
6	144	30°	✓	✓	80	✓	200
7	144	30°	✓	✓	90	✓	200
8	144	30°	✓	✓	95	✓	200
9	144	15°	✓	✓	30	✓	200
10	144	15°	✓	✓	40	✓	200
11	144	15°	✓	✓	50	✓	200
12	144	15°	✓	✓	60	✓	200
13	144	15°	✓	✓	70	✓	200
14	144	15°	✓	✓	80	✓	200
15	144	15°	✓	✓	90	✓	200
16	144	15°	✓	✓	95	✓	200
17	144	25°	✓	✓	30	✓	200
18	144	25°	✓	✓	40	✓	200
19	144	25°	✓	✓	50	✓	200
20	144	25°	✓	✓	60	✓	200
21	144	25°	✓	✓	70	✓	200
22	144	25°	✓	✓	80	✓	200
23	144	25°	✓	✓	90	✓	200
24	144	25°	✓	✓	95	✓	200
25	144	20°	✓	✓	30	✓	200
26	144	20°	✓	✓	40	✓	200
27	144	20°	✓	✓	50	✓	200
28	144	20°	✓	✓	60	✓	200
29	144	20°	✓	✓	70	✓	200
30	144	20°	✓	✓	80	✓	200
31	144	20°	✓	✓	90	✓	200
32	144	20°	✓	✓	95	✓	200